Universitá degli studi di Milano
Department of Biomedical Sciences for Health
PhD Course in Integrated Biomedical Research
XXIX Cycle

PhD Thesis

Computer aided feature extraction in 3D oro-maxillo-facial images

PhD Thesis by:
Marina CODARI
R10409

Advisor: Prof.ssa Chiarella Sforza
Co-Advisor: Prof. Giuseppe Baselli

January 2017, 29^{th} **Cycle**

"Il divertimento della ricerca scientifica è anche
trovare sempre altre frontiere da superare,
costruire mezzi più potenti d'indagine, teorie più complesse,
cercare sempre di progredire pur sapendo che probabilmente
ci si avvicinerà sempre di più a comprendere la realtà,
senza arrivare mai a capirla completamente."

MARGHERITA HACK

Acknowledgements

"There is one way to learn, it's through action.
Everything you need to know you have
learned through your journey"
PAULO COELHO

First and foremost I would like to thank Prof. Chiarella Sforza and Prof. Giuseppe Baselli, who have been more that my promoters, supporting me both during research and daily life. We know each other from a long time and I feel privileged be your student, the teachings that I have received from you go beyond the academic world.

Secondly, I really would like to thank Prof. Reinhilde Jacobs that offered me the amazing opportunity of being part of her research group at the KU Leuven University. I will always have a wonderful memory of all the moments spent in Leuven.

Furthermore, I would like to thanks the Cefla Research and Development team. In particular, big thanks goes to Marco Serafini, Davide Bianconi, Luca Guardini, Carlo Sandri and Marco Soldini who showed me how the academic and company world can collaborate to obtain great results.

I would like to thanks also to Dr. Tartaglia and the SST Dentofacial Clinic staff who worked with me on more than one study.

Usually, a person at work is surrounded by colleagues. In these years I have been lucky to be surrounded by friends. For this reason I would thank all my Italian colleagues and friends of the lab: Daniela, Valentina, Claudia, Ilaria, Isabella, Laura, Matteo, Luca, and Domenico. I would had never enjoyed my work as I really did without you.

A big thanks goes also to Matteo Caffini, who worked with me even when I was no longer his student, becoming a colleague and friend.

At last, but not least, I would like to thank all the incredible people that I met in Leuven and worked with me in the OMFS-IMPATH research group: Laura, Karla, Mariana, Natalia, Manuelita, Emmy, Deepti, Ruth, Bieke, Marta, Jeroen, Mostafa, Yan, Yi, Ademir, Titiaan, Andreas, Omar, Juan and David.

Finally, I would like to dedicate this thesis to my family: to Andrea, that always supports me and believes in me in every moment of my life. To my sister and my parents, that believe in me more then myself and finally to my whole family. This thesis would not be possible without you.

Many thanks,

Marina

Contents

List of Figures

List of Tables

List of Abbreviations

CBCT	**C**one **B**eam **C**omputed **T**omography
MSCT	**M**ulti-**S**lice **C**omputed **T**omography
MRI	**M**agnetic **R**esonance **I**maging
US	**U**ltrasound **I**maging
CAD	**C**omputer **A**ided **D**esign
CAM	**C**omputer **A**ided **M**anufacture
DICOM	**D**igital **I**maging and **CO**mmunications in **M**edicine
CT	**C**omputed **T**omography
FOV	**F**ield **O**f **V**iew
HU	**H**ounsfield **U**nits
GUI	**G**uided **U**ser **I**nterface
MPR	**M**ulti**P**lanar **R**econstruction
MSD	**M**ean **S**quare **D**ifference
MIRT	**M**edical **I**mage **R**egistration **T**oolbox
FFD	**F**ree **F**orm **D**eformation
ICC	**I**nterclass **C**orrelation **C**oefficient
IQR	**I**nter**Q**uartile **R**ange
ROI	**R**egion **O**f **I**nterest
VD	**V**olume **D**ifference
SD	**S**tandard **D**eviation
ANOVA	**AN**alysis **O**f **VA**riance
nSD	**n**ormalized **S**tandard **D**eviation
AD	**A**rea **D**ifference
VOI	**V**olume **O**f **I**nterest
MAR	**M**etal **A**rtifact **R**eduction
FA	**F**acial **A**rea
UT	**U**pper **T**hird

MT	**M**iddle **T**hird
LT	**L**ower **T**hird
RMSD	**R**oot **M**ean **S**quare **D**eviation
RC	**R**epeatability **C**oefficient
ICP	**I**terative **C**losest **P**oint
NSD	**N**asal **S**eptal **D**eviation
MR	**M**agnetic **R**esonance
VDP	**V**olume **D**ifference **P**ercentage
SDI	**S**eptal **D**eviation **I**ndex
SDA	**S**eptal **D**eviation **A**ngle
PCA	**P**rincipal **C**omponent **A**nalysis
PC	**P**rincipal **C**omponent

Abstract

Aim: Recently, maxillofacial imaging has drastically evolved thanks to the development of dedicated imaging techniques. The complex anatomy of the maxillofacial region requires the use of different image modalities, demanding the development of dedicated image analysis procedures. This doctoral thesis aims at explore the possible use of image processing techniques for maxillofacial applications.

Hard tissue imaging: In this chapter, we propose different studies that focused on image segmentation, registration and artifact reduction applied to the automatic extraction of hard tissue structures in CBCT data. The procedure involves an adaptive, cluster-based segmentation of bone tissues followed by an intensity-based registration of an annotated reference volume onto a patient CBCT head volume. Automatic segmentation shows a high accuracy level with no significant difference between automatically and manually determined threshold values. The overall median localization error was equal to 1.99 mm with an interquartile range (IQR) of 1.22-2.89 mm.

The second study aims to objectively compare the influence of different image parameters on metal artifact generation. After a fully automatic segmentation and image registration, the effect on metal object segmentation and background image noise was evaluated. Results showed that metal object segmentation is highly influenced by the device and material factor, while background noise was more affected by the devices and the FOV parameters compared to the used material.

Then, in the third study, in order to improve the automatic extraction of craniofacial features and cephalometric landmarks, we designed a metal artifacts reduction (MAR) algorithm. The new MAR step is fully integrated with our landmark detection algorithm and works on both projection and image domain and allows the automatic detection of the corrupted portion of the image, thus preserving image details. The algorithm was tested on 17 CBCT volumes with a total number of 245 analysed VOIs and reduction of SD values in not metallic voxels was used as image metric. In our dataset, the proposed MAR

algorithm always decreased the voxel intensity SD in the examined VOIs, thus showing a significant metal artifact reduction in a fully automatic way.
Finally, in order to improve the segmentation quality in the mandibular condyle region, which is usually affected by large amount of noise, a dedicated segmentation approach was developed. Also this algorithm is integrated with the hard tissue segmentation approach and it is based on patient adaptive thresholding and contrast enhancement techniques. The algorithm was tested in vitro on a series of CT and CBCT scans of a dried human mandible. To reproduce soft-tissue attenuation, a copper filter was used. The proposed automatic segmentation algorithm allows to improve the quality of the trabecular bone segmentation, significantly reducing the overestimation of the segmented bone.

Soft tissue imaging: In this section, the application of stereophotogrammetric systems and laser scanners for the development of computer aided approaches for facial morphology evaluation was evaluated.
In the first study, we present a new quantitative method to assess symmetry in different facial thirds, objectively defined on trigeminal distribution branches territories. Seventy subjects (40 healthy controls and 30 patients affected by monolateral facial palsy) were acquired with a stereophotogrammetric system and the level of asymmetry was evaluated, RMSD was used as asymmetry metric. Results show a high average reproducibility of area selection and significant differences in RMSD values between controls and patients for all the thirds. No significant differences were found on different thirds among controls, while significant differences were found for upper, middle and lower thirds of patients. The proposed method provides an accurate, reproducible and local facial symmetry analysis.
The second study aims to develop an imaging technique that allows to integrate the information about patient dentition together with the stereophotogrammetric reconstruction of the face, providing an un-invasive way to assess the morphology of facial soft tissues in relation to teeth. The proposed algorithm is based on several surface registration steps, initialized by a landmark registration step. To validate the proposed method, CBCT images were analysed and a series of dentofacial distances were calculated. The high values of percentage of corresponding point and a median distance of 0.59 mm prove the accuracy of the registration progress. Statistical analysis shows no significant differences between distanced calculated on CBCT image or on face and dental surfaces, except for one distance.

Upper airway imaging: In this last section, a new image analysis method was developed to assess whether three-dimensional morphometric parameters could be useful in nasal septal deviation (NSD) diagnosis and, secondarily, whether CBCT could be considered an adequate imaging technique for the proposed task. Forty-six CBCT scan were segmented using ITK-Snap in order to obtain the 3D model of patient upper airway and compute four morphological parameters septal deviation angle (SDA), percentage of volume difference between right and left side of the nasal airways, nasal airway total volume and a new synthetic septal deviation index (SDI). Principal component analysis (PCA) was used to unveil relationships between each variable and the global nasal airway variability. Among the analysed parameters, SDI seemed to be the most suitable for the quantitative assessment of NSD, and CBCT allowed accurate assessment of airway morphology.

Conclusion: In conclusion, we proved that the application of image processing techniques may help in the development of new diagnostic tools. This PhD thesis has helped creating a good basis for future studies on the application of imaging techniques in oral and maxillofacial applications.

Sommario

Scopo del lavoro: Negli ultimi anni, l'imaging maxillo-facciale si é notevolmente evoluto grazie all'introduzione di nuove tecnologie per l'analisi tridimensionale del distretto cranio-facciale. La complessa anatomia di questo distretto e i differenti tessuti che lo compongono richiedono l'utilizzo di diverse modalitá diagnostiche e, di conseguenza, dello sviluppo di metodi di analisi dedicati. Questa tesi di dottorato ha lo scopo di esplorare le possibili applicazioni delle metodiche di analisi di immagini a tematiche riguardanti la diagnostica per immagini in ambito maxillo-facciale.

Imaging dei tessuti duri: In questo capitolo vengono trattati diversi studi focalizzati sulla segmentazione, registrazione e riduzione di artefatti, volte all'estrazione di caratteristiche dei tessuti duri in immagini CBCT. In primo luogo, viene sviluppato e validato un algoritmo di segmentazione automatica dei tessuti duri basato sul calcolo di 4 diversi cluster in un subset di slice, al fine di ricavare una soglia di segmentazione adattiva, specifica per ogni immagine analizzata. La fase di segmentazione é seguita da una di registrazione, nella quale un cranio annotato di riferimento viene automaticamente registrato su quello del paziente in modo da ottenere l'annotazione automatica di 21 punti cefalometrici. La validazione ha mostrato alti livelli di accuratezza nella fase di segmentazione e un errore mediano nell'annotazione automatica pari a 1.99 mm con un intervallo inter-quartile pari a 1.22-2.89 mm.

Il secondo studio ha come scopo quello di valutare quantitativamente l'effetto di diversi parametri di immagine sulla genesi di artefatti da metallo. Gli oggetti metallici contenuti nei fantocci acquisiti durante lo studio sono stati automaticamente segmentati e registrati in modo da permettere la valutazione oggettiva dell'impatto degli artefatti sia nel processo di segmentazione degli oggetti metallici che nella valutazione del rumore presente sullo sfondo dell'immagine. I risultati dimostrano che la segmentazione degli oggetti metallici é principalmente influenzata dal tipo di materiale presente nel fantoccio e dal tipo di CBCT utilizzata. Per quanto riguarda l'effetto sui tessuti circostanti, questo risulta essere

maggiormente influenzato dal tipo di FOV e tomografo utilizzato.
Nel terzo studio, al fine di migliorare la segmentazione dei tessuti duri e della detezione automatica dei landmark cefalometrici, é stato sviluppato un algoritmo per la riduzione degli artefatti da metallo in immagini CBCT. L'algoritmo é completamente integrato nell'algoritmo di annotazione e lavora sia nello spazio immagine che nello spazio delle proiezioni. Inoltre la soluzione proposta individua automaticamente la porzione di volume corrotta da artefatti in modo da ridurre il costo computazionale e preservare il maggior numero di dettagli possibile all'interno dell'immagine. L'algoritmo é stato testato su 17 volumi CBCT e in particolare in 245 VOI. I risultati mostrano una riduzione significativa della deviazione standard nei valori di intensitá, dimostrando l'efficacia della soluzione proposta. Infine, allo scopo di migliorare l'accuratezza della segmentazione dei condili mandibolari, é stato sviluppato un algoritmo automatico atto alla segmentazione di questa specifica struttura anatomica.
Anche questo algoritmo é perfettamente integrato con il primo algoritmo di segmentazione e si basa sull'utilizzo di sogliatura adattiva e tecniche di analisi di immagini atte all'ottimizzazione del contrasto. L'algoritmo é stato testato in-vitro su una serie di CT e CBCT. La segmentazione é stata comparata con quella ottenuta attraverso l'utilizzo di una micro-CT, che rappresenta lo standard per l'imaging dei tessuti duri. La soluzione proposta permette di migliorare l'accuratezza della segmentazione ed in particolare di migliorare la segmentazione delle strutture trabecolari, riducendo significativamente la sovrastima del volume osseo.

Imaging dei tessuti molli: In questa sezione vengono presentati due studi che indagano la possibilitá di utilizzo di sistemi stereofotogrammetrici e di laser scanner per l'analisi dei tessuti molli facciali.
Nel primo studio, il metodo proposto é stato testato su 70 soggetti (40 sani e 30 affetti da paralisi del nervo facciale) acquisiti con sistema stereofotogrammetrico. La RMSD tra i due lati del volto, analizzata nei diversi terzi, é stata usata come metrica per la definizione del grado di asimmetria. I risultati mostrano un alto livello di riporducibilitá del metodo proposto. Inoltre i valori du RMSD mostrano una significativa differenza tra soggetti sani e patologici.
Il secondo studio propone lo sviluppo di una metodica di integrazione delle arcate dentarie, digitalizzate attraverso l'utilizzo di un scanner laser, con la superficie della faccia del soggetto acquisita con un sistema stereofotogrammetrico. Questo metodo prevede una serie di step di regsitrazione di superfici. La validazione dei risultati ottenuti é stata effet-

tuata confrontando l'esito del processo di registrazione con le CBCT degli stessi soggetti. Il basso errore di registrazione (0.59 mm) prova l'accuratezza del metodo proposto. Inoltre l'analisi statistica non mostra differenze statisticamente significative per quasi tutte le distanze dento-facciali usate nel processo di validazione.

Imaging delle vie aeree superiori: In questa ultima sezione viene mostrato uno studio relativo alla modellizazzione e analisi della morfologia delle vie aeree superiori in immagini CBCT. In particolare, questo studio si focalizza sullo sviluppo di un indice atto alla valutazione quantitativa della deviazione del setto nasale. Il metodo proposto é stato testato su 46 immagini CBCT. In queste immagini sono stati valutati 4 parametri morfologici: l'angolo di deviazione del setto, la differenza di volume delle vie aeree nasali tra lato destro e sinistro, il volume totale delle vie aeree nasali e il nuovo indice di deviazione del setto. L'analisi delle componenti principali é stata usata per valutare la capacitÃ dei diversi indici di modellizzare la variabilitá della morfologia delle vie aeree all'interno del campione studiato. Tra i parametri analizzati il nuovo indice sembra essere quello meglio utilizzabile per un'accurata valutazione della condizione del soggetto preso in esame.

Conclusioni: In conclusione, in questa tesi di dottorato vengono proposti diversi approcci dove l'utilizzo di tecniche proprie dell'analisi d'immagine vengono usate al fine di risolvere problematiche tipiche dell'ambito maxillo-facciale. Questa tesi di dottorato getta le basi per studi futuri sull'applicazione e validazione di tali algoritmi in ambito clinico.

Chapter 1

Oro-maxillofacial imaging

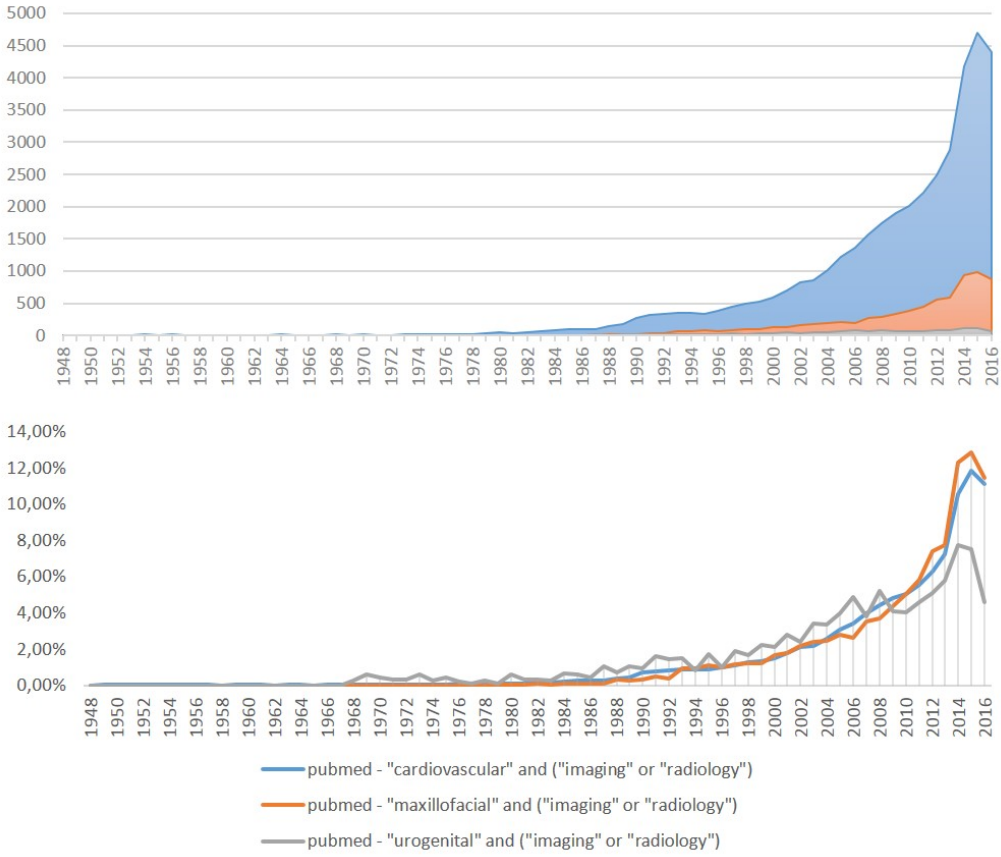

Figure 1.1: Result of the PubMed research, number of article published each year and the same value normalized on the total number of published article for three different imaging fields: cardiovascular, maxillofacial and urogenital

During the last decades, maxillofacial imaging has drastically evolved thanks to the development of dedicated imaging techniques. Figure 1.1 shows the number of articles published each year and the same value normalized on the total number of published article for three

different imaging fields: cardiovascular, maxillofacial and urogenital. As can be seen, the amount of published articles is greater in cardiovascular imaging, which is a, well-known, growing research field compared to maxillofacial imaging. Nevertheless, the normalized amount of papers published each year shows a similar incremental trend in cardiovascular and maxillofacial imaging. Moreover, in the last years, this trend has accelerated in the maxillofacial field, proving the significant increment of interest of the research community on this topic.

Maxillofacial imaging involves the interpretation of diagnostic images of the craniofacial structures, which are well known for their complex anatomy [1]. Craniofacial region complexity is due to the fact that it is composed of many different structures, such as elements of the musculoskeletal, digestive, respiratory, nervous, vascular and endocrine systems. All these structures create a unique morphology made from cartilaginous, osseous, dental and soft-tissue elements, which requires different modalities to be imaged [2].

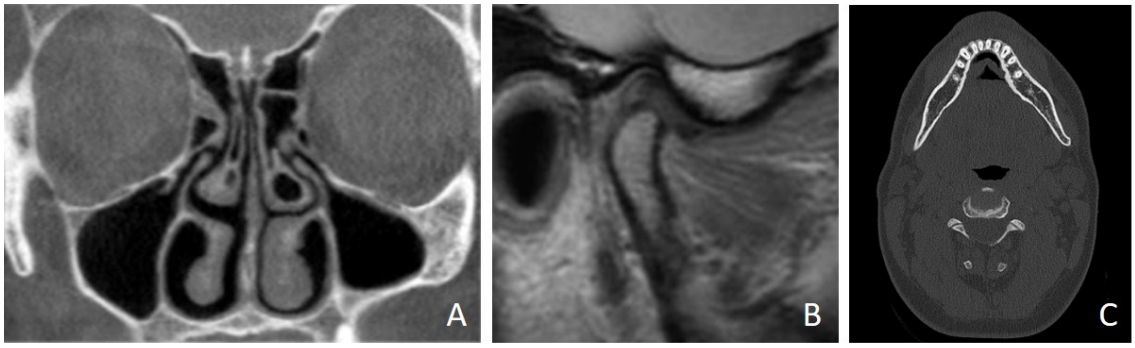

Figure 1.2: Examples of different imaging modalities applied to the maxillofacial region: CBCT (A), MRI (B) and MSCT (C)

Traditional maxillofacial imaging was based on two-dimensional X-ray radiographs. Nowadays, the advent of new imaging technologies has moved this radiology branch to a three-dimensional virtual based process [3].

Different imaging modalities are used for the diagnosis of maxillofacial diseases, among these CBCT, MSCT, MRI and US imaging are the most used in daily clinical practice to obtain a 3D representation of the hard and soft tissue of the craniofacial region. Figure 1.2 shows three examples of images that can be used in daily diagnosis. As can be seen, each modality allows to enhance different tissues. For example, CBCT and MSCT images (Figures 1.2.A and 1.2.C) are more suitable for hard tissue evaluation, due to their high contrast of dense structures such as teeth, bone and enamel [4]. On the other hand, MRI

images (Figures 1.2.B) can be a powerful tool for soft tissue evaluation.

Together with these systems, the use of optical devices, such as laser scanner, intra-oral scanner and stereophotogrammetric systems has increased in the last years. The advantage of these systems is that they allow to render the facial soft tissue and obtain the digital models of dental arches in a fast and un-invasive way [2].

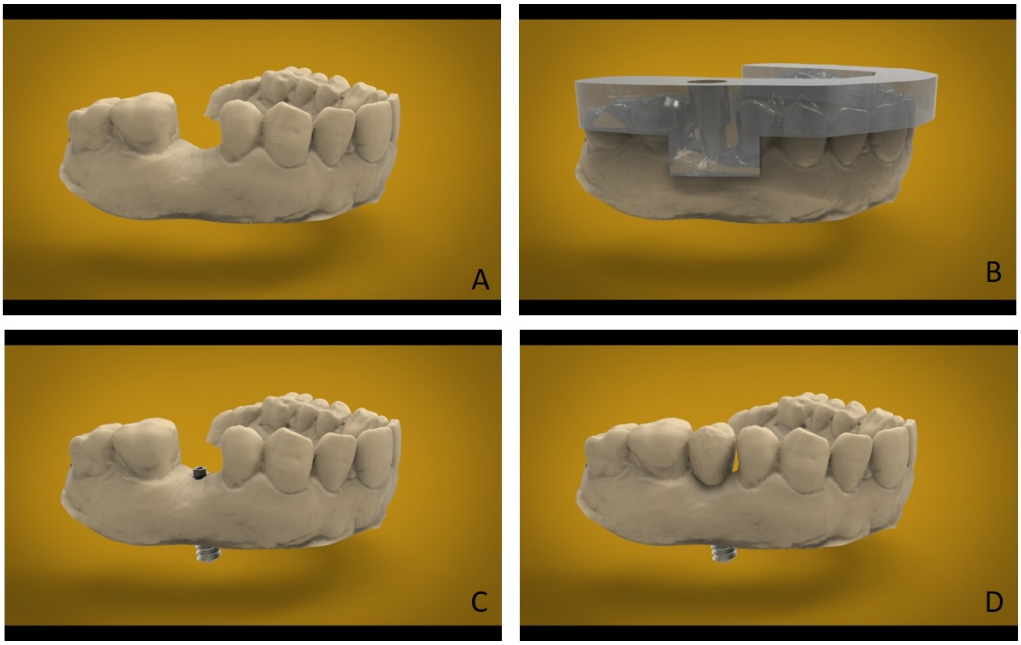

Figure 1.3: Computer aided design and manufacture of a surgical guide for implant placement (B), which allows to simulate implant placement (C) and design tooth prosthesis (D), based on patient dentition (A), before the surgery

Data obtained with these imaging modalities can be processed to integrate and interpret patient data, making clinicians able to plan treatment and assess its outcomes in a precise and objective way [5]. In particular, the integration of those data allow the use of computer aided surgical systems to customize surgery and prosthesis manufacturing [6]. Figure 1.3 shows an example CAD and CAM of a surgical guide for implant placement and of dental prosthesis based on patient dentition.

Moreover, the correct use of these modalities will lead to a reduction of patient discomfort, decreasing the invasiveness of diagnostic tools.

The incremental use of this images in clinical practice, has led to the development of new imaging techniques for craniofacial feature extraction.

In the last years, several segmentation approaches were developed in order to improve 3D model accuracy. In particular, dedicated segmentation approaches were designed for each

structures of the craniofacial complex, such as teeth [7–9], bony structures [10–12] and upper airways [13, 14].

Moreover, in order to integrate information from different data sources, several image registration techniques were developed [15, 16]. Data fusion approaches allow to register different DICOM images to visualize different kinds of tissues at the same time, or to integrate morphological and functional data [17, 18]. Furthermore, image registration allows to fuse DICOM images with three-dimensional surface models obtained using optical systems. For example, the fusion of 3D model of dental arches with the CBCT data of the patient is now routinely used in computer aided implantology and orthognathic surgery [19, 20].

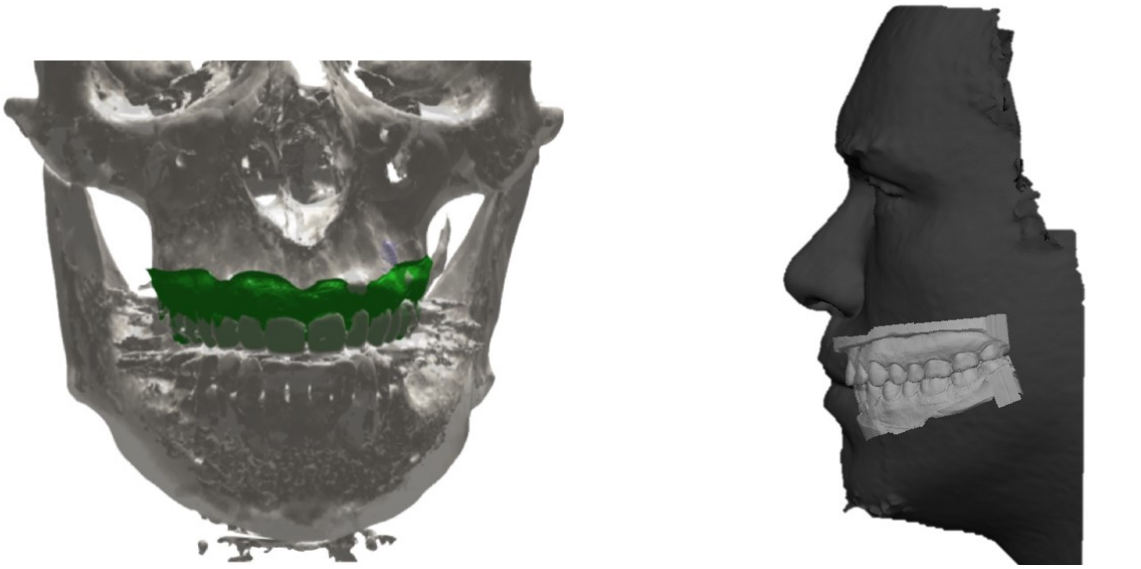

Figure 1.4: Example of virtual patient models, on the right is depicted a model that integrates CBCT bone rendering, the 3D digital model of patient dental arch and the CAD model of the dental implant. On the left is depicted an virtual model composed by the stereophotogrammetric facial surface and the digital dental casts of the patient

The integration of different image data allows not only the complete and accurate evaluation of patient condition, but also to overcome the limitations of a specific image modality, fusing it with another one that compensates its lack of information.

The creation of virtual patients model will allow to simulate the entire treatment noninvasively and adapt it to patient expectations. Moreover, virtual planning allows to take the relationship between dental arches and surrounding bony structure into account at the same time using a single 3D model [21].

Figure 1.4 shows some examples of virtual patient models created fusing different three-dimensional images of the craniofacial complex. The continuous advancement in image analysis techniques may allow researchers to develop patient-specific and pathology-specific protocols, in order to customize treatment planning and follow-up evaluations as much as possible.

In this PhD thesis, we applied imaging processing techniques to maxillo-facial tasks in order to obtain digital tools that may help clinicians during diagnosis and treatment evaluation. The thesis is divided in three main sections, each one related to the kind of biological tissue analysed in the proposed studies.

Chapter 2

Overview on image processing techniques

In order to fully understand the imaging processes used in all the studies presented in this doctoral thesis, an overview of the main existing techniques is presented in this chapter.

2.1 Image segmentation

Image segmentation plays a key role in many medical imaging applications. Its main aim consists in automating or facilitating the delineation of anatomical structures or other object of interest. Diagnostic imaging techniques allow to enrich the knowledge of normal and pathological anatomy and represent a critical step in diagnosis and treatment planning.

In the literature, image segmentation is defined as "the partitioning of an image into non-overlapping, constituent regions that are homogeneous with respect to some characteristic such as intensity or texture" [22].

Segmentation can be performed in a two-dimensional or three-dimensional image domains. In general, methods that rely only on image intensity values are independent from the image domain, on the other hand other segmentation method, such as region growing, can operate differently depending on image dimensionality. Moreover segmentation can be performed at different interaction levels. The identification of a trade-off between manual interaction and segmentation performance represents one of the main issues in medical applications.

Over the years several methods for biomedical image segmentation have been developed. These approaches can be classified into main categories [23].

- **Thresholding**: this approach allows the creation of a binary image segmenting scalar images by partitioning of its image intensity values. This method is simple and effective where different structures have different intensity values. The main limitations of this approach rely on the fact that it does not consider the spatial characteristics of the image, making the segmentation to be sensitive to noises and intensities inhomogeneity.

- **Region growing**: it is a technique that allows to extract a region of the image which is connected basing on some a priori criteria. Unfortunately it usually requires manual interaction to find the seed point. Thus, for each region of interest, a seed has to be planted. Furthermore, it can also be sensitive to noise, creating holes or disconnecting anatomical regions.

- **Classifiers**: these pattern recognition techniques explore a feature space, e.g. image intensities, derived from the image using data with known labels. They are defined as supervised methods, since they require training data that are manually segmented and used as models to automatically segment new data.

- **Clustering**: clustering can be defined as a classifier algorithm that does not require the use of training data. For this reason, they are defined as unsupervised methods. Clustering techniques use iterative methods to compensate the lack of training data. During the iterations, these algorithms alternate between segmenting the image and characterizing the properties of each of the clusters, training itself using the available data.

- **Markov random field**: that represents a statistical model which can be used within other segmentation methods, modelling spatial interactions between adjacent pixels.

- **Artificial neural networks**: it represents a paradigm for machine learning and is used in several ways for image segmentation. In medical imaging it is often used as a classifier that using a training data allows to segment new data.

- **Deformable models**: this model-based techniques are usually used for delineating region boundaries using closed parametric curves or surfaces that are deformed under the influence of both internal and external forces. The main advantages of these models are their ability to directly generate closed parametric curves or surfaces from images and their robustness to noise and spurious edges. Their main disadvantage is

that they require manual interaction to place an initial model and choose appropriate parameters.

- **Atlas-guided**: image segmentation that requires a standard atlas or template. The atlas is generated by compiling anatomical information of the structure that requires segmenting, then it is used as a reference frame for segmenting new images.

In this doctoral thesis, different segmentation approaches were used. In each study the characteristic of the used image modalities were evaluated in order to find the segmentation approach that best fits image proprieties and allow to segment the anatomical structure of interest.

2.2 Image registration

To better understand the reasons that led to the choice of the registration approaches used in presented studies, it is useful to define the registration task and the criteria by which different methods can be classified.
The task of image registration is to find an *optimal geometric transformation* between corresponding image data [24]. Each registration methods can be seen as different combination of the following categories:

- **Dimensionality**: like segmentation, registration can be performed in any dimension, in all the studies presented in this thesis work three-dimensional images were used.

- **Domain of the transformations**: a transformation is called *global* if it applies to the entire image and *local* if subsections of the image which have their own transformation are defined [25]

- **Elasticity of the transformations**: transformations can be divided into *rigid*, *affine*, *projective*, and *elastic*. An image coordinate transformation is called rigid, when only translations and rotations are allowed. If the transformation maps parallel lines onto parallel lines it is called affine and if it maps lines onto lines, it is called projective. Finally, if it maps lines onto curves, it is called elastic [26]

- **Nature of registration basis**: image based registration can be divided into *intrinsic*, based on the image information as generated by the patient and *extrinsic*, based on foreign objects introduced into the image space (e.g. skin markers) [27].

In this thesis, intrinsic registration methods were used, which rely on image content and can be classified as:

  - **Corresponding landmark based**: these methods are based on a limited set of corresponding landmarks that can be manually or automatically detected in the image.
  - **Surface based**: when it is not possible to find corresponding landmarks, surface registration approach can be used to find the geometrical transformation that best align the analysed surfaces.
  - **Segmentation based**: it can be rigid or deformable model based, where the same anatomical structures are segmented from both image to be registered.
  - **Voxel property based**: these methods stand apart from the other intrinsic methods, due to the fact that they operate directly on the image grey values, without prior data reduction caused by the user or segmentation [27].

- **Interaction**: image registration methods can be divided into 3 level of interaction. *Automatic* where no user interaction is needed, *semi-automatic* where the user can specify some registration parameter and *interactive*, where the user does the registration himself assisted by software [27]

- **Image modality**: when a image is registered with another image create with the same image modality, the registration can be defined a *mono-modal* process. If the two images that have to be registered are created by different imaging modalities the registration is defined as *multi-modal*

- **Involved subject**: when all the images involved are acquired from a single patient the registration process can be defined as *intra-subject registration*. If the registration is performed using two image from different patient it is called *inter-subject registration* and then if one image is acquired from a single patient and the other image is constructed using a image informations database containing different patients acquisitions, it is called *atlas-based registration* [27]

As well as for the segmentation approach, when image registration is needed, the properties of analysed images were evaluated in order to find the registration approach that best fulfil study requirements.

Chapter 3

Hard Tissue Imaging

This chapter is based on:

- M. Codari et al. "Computed aided Cephalometry from CBCT data", *International Journal of Computer Assisted Radiology and Surgery*, 1-9, 2016.
- M. Codari et al. "Quantitative evaluation of metal artifact using different CBCT devices, high-density materials and field of views", submitted to *Clinical Oral Implant Research*, 2016. This project was made under the supervision of Prof. Jacobs as part of the OMFS-IMPATH research group of the KU Leuven University in collaboration with University of Campinas.
- M. Codari et al. "Automatic segmentation for condylar morphometric analysis in CT and CBCT data: an in-vitro validation", *International Journal of Computer Assisted Radiology and Surgery*, 11(S1):S146-S147, 2016. Proceedings of the CARS 2016 Conference. This project was made in under the supervision of Prof. Jacobs as part of the OMFS-IMPATH research group of the KU Leuven University in collaboration with University of Milan and Politecico di Milano.
- M. Codari et al. "Automatic Hard Tissue Segmentation And Metal Artifacts Reduction In Dental CBCT Data", *International Journal of Computer Aided Radiology and Surgery*, 10(S1):300-301, 2015. Proceedings of the CARS 2015 Conference.
- The project titled "Elaborazione ed integrazione nella piattaforma software di Cefla di metodiche algoritmiche per le rimozione/riduzione di artefatti da metallo in CBCT", financed by Cefla S.C and made in collaboration with the Politecnico di Milano.

3.1 Hard tissue maxillofacial imaging

Three-dimensional images are gaining importance in assisting surgical planning and diagnosis in maxillofacial field. In particular, when cross-sectional images of the hard tissues of craniofacial structures are needed, MSCT and CBCT are the current method of choice [4]. Both CT and CBCT are tomographic, X-ray based, techniques which provide high resolution and well contrasted images of hard tissues. The differences between these two modalities are primarily related to beam geometry, which can be cone or fan shaped, scanning and detector geometry [28].

In particular, CBCT allows to obtain high resolution and isotropic images, which dimensions range from 0.08 to 0.4 mm depending on device and acquisition parameters [29]. Moreover, CBCT data are obtained with only one rotation of the source and detector around patient's head. During this rotation, projection data taken from different angles are used for 3D volume reconstruction, which is performed through modification of the original cone-beam algorithm developed by Feldkamp [30,31]. The single rotation reduces the acquisition time, which ranges between 6 and 20 seconds, reducing the possibility of major movement artifacts [32]. Figure 3.1 shows an example of an axial slice of a CBCT image of the craniofacial complex and its corresponding 3D surface rendering.

Although CBCT provides diagnostically acceptable images, projection data are affected by a considerable amount of scatter radiation, that leads to an inferior soft tissue contrast compared to MSCT images [4].

Both MSCT and CBCT are used to asses bony structures of the head and neck. Nevertheless the use of CBCT has increased, due to the relatively low dose delivered to the patient during acquisition [33]. Nowadays, CBCT finds its application in implantology,

Figure 3.1: Axial slice of a CBCT image and the corresponding three-dimensional renderings of hard tissue structures

orthodontics, endodontics, detection of maxillofacial traumas, maxillofacial surgical planning, temporomandibular joint evaluation and otorhinolaryngology [34].

All these clinical applications require the development of dedicated image processing techniques. For this reason, with the advancement of its use in clinical practice, several effort were performed to improve its image quality.

One of the main limitations of CBCT images is the presence of different kind of image artifacts, which are defined as structures visible in the reconstructed image that are not present in the imaged object. Among them extinction artefacts, beam hardening artefacts, partial volume effect, aliasing and motion artifacts are the most relevant [32].

Moreover, the presence of high density objects, such as metals, generated strong artifacts that can compromise the diagnostic process [35,36]. Figure 3.2 shows an example of CBCT image corrupted by metal artifacts, showing the effect of both image grey values and rendered surface model.

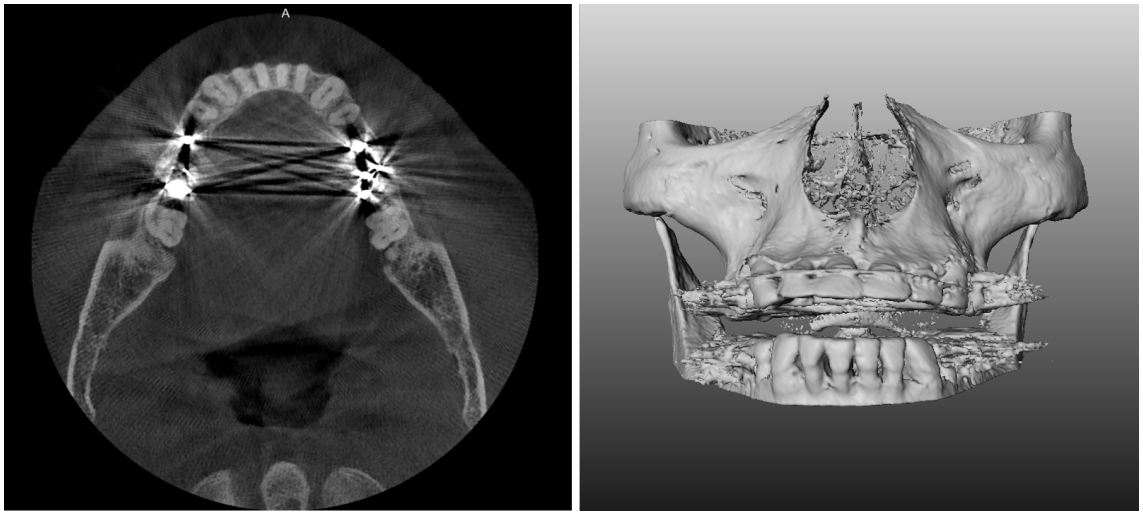

Figure 3.2: Axial slice of a CBCT image corrupted by metal artifacts (left) and the corresponding three-dimensional rendering of hard tissue structures (right)

Metal artifacts can strongly compromise all the image processing steps that are usually involved in CBCT image analysis, like image segmentation and registration. For these reasons, the quantification and reduction of such artifacts is becoming a "hot" topic in dental research.

Recently, some studies were conducted in order to assess the expression of metal artifacts and their impact on image quality, finding that material density, exposure parameters, FOV and imaged structures affect their expression [35–37]. For this reason, several metal

artifact reduction algorithms has been developed [38–42].

Other efforts were done in the development of automatic or semi-automatic segmentation methods for CBCT data. The need of automatic methods relies in another limitation of CBCT images, namely the grey values variability of its voxels.

CBCT devices use 12-bit or 16-bit images scaled like Hounsfield units (HU), but nonetheless it is demonstrated that CBCT grey values cannot be as accurately calibrated as HU. This miscalibration is due to the amount of noise, artifacts, beam geometry and the limited FOV size [43]. This variability in grey values make it difficult to standardize threshold segmentation approaches, which are those most commonly used to segment hard tissue in clinical practice. For this reason, several automatic or semi-automatic segmentation algorithms for CBCT data were developed [44–46]. Furthermore the development of automatic or nearly automatic segmentation algorithms help in the reduction of operator variability, which is a well-known source of inaccuracy in segmentation tasks.

In maxillofacial and oral radiology, as for the other branches of radiology, operator dependency of performed measurements is one of the most important source of bias. This problem is usually related to the huge number of image processing steps that characterize computer aided surgical planning and image segmentation. All these steps represent a series of approximations subjected to intra and inter-operator variability and are usually time consuming. For all these reasons, nearly automatic or fully automatic softwares have been developed in the last years [47–49].

CBCT imaging is becoming the imaging method of choice when three-dimensional analysis of the hard tissues of oral and maxillofacial region is needed. Nevertheless some limitations need to be overcome to fully exploit its advantages. Efforts should be made in both image improvement and diagnostic tool development.

In this section, we present a series of projects focused on automatic feature extraction, automatic segmentation and artifact reduction in CBCT data.

3.2 Computed aided Cephalometry from CBCT data

The measurement of the head, known as cephalometry, considers both soft and hard tissues and has many applications in today's world. The application of cephalometry to the clinical needs, commonly known as cephalometric analysis, is widely used in dental applications, such as orthodontics and implantology, and in surgical planning and treatment evaluation for maxillofacial surgery [50–52]. Traditionally, cephalometric analyses have been manually performed on a 2D cephalogram, which is a standardized tracing of craniofacial structures as depicted by a latero-lateral radiography of the head. Currently, with the diffusion of Cone Beam Computerized Tomography scanners, 3D cephalometric analysis is emerging [53]. CBCT is used for small segments of the body, such as the head or part of it, and generally delivers lower dose to the patient, compared to CT [54]. In particular, CBCT is a useful tool for identification and evaluation of treatment outcomes, becoming one of the most common image modality used to visualize the facial skeleton [55–57]. Both maxillofacial surgeons and dentists can foresee remarkable developments by the aid of computerized methods permitting to easily extract individual features and perform measurements.

Nowadays, manual point-picking represents the method of choice to perform 3D cephalometric analysis, however this approach is limited in accuracy and repeatability due to the differences in intra- and inter-operator landmark identification [58–60]. The need to overcome these limitations recently led to the development of aided, automated or nearly-automated methods [45, 48, 61–65]. Here, we propose a semi-automatic computerized method that can help the clinician to annotate three-dimensional CBCT volumes of the human head, using intensity-based image registration.

Material and Methods

The proposed algorithm, entirely developed in MATLAB (MathWorks, Natick, MA, USA), automatically segments the skull from CBCT volumes of the human head and subsequently estimates a number of cephalometric landmarks. The flowchart of the proposed algorithm is presented in Figure 3.3.

Anatomical Landmarks: In this study, a set of fiducial points, which location will be estimated, must be decided and defined. To validate the proposed method, a set of 21 landmarks, commonly used in clinical practice and distributed all over the skull surface, was chosen [66]. All chosen landmarks are listed in Table 3.1. [54].

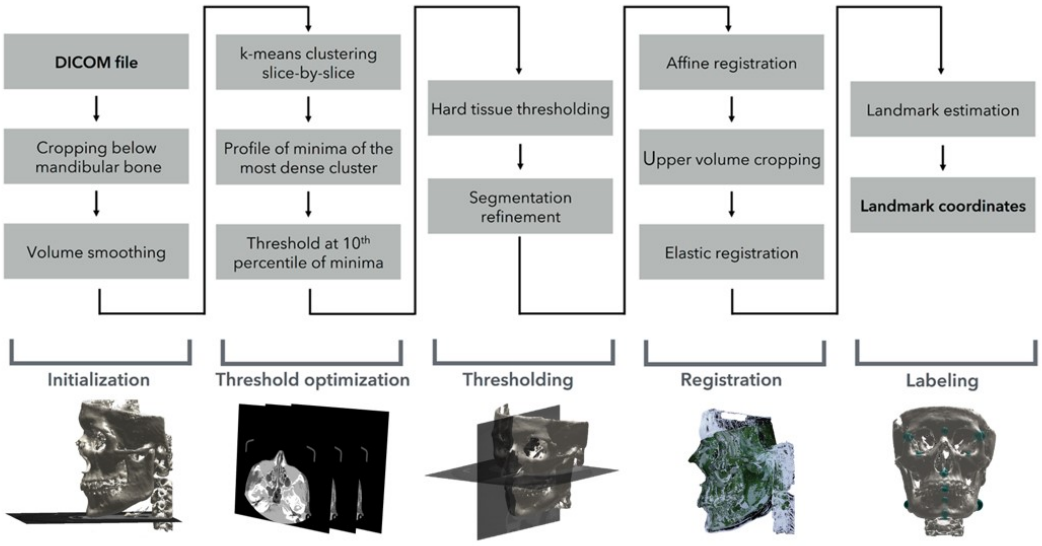

Figure 3.3: Flowchart of the presented algorithm, which receives a DICOM file as input, articulates in 3 phases: image pre-processing, segmentation and registration and returns the landmark coordinates as output

Dataset: Datasets of 18 subjects who underwent CBCT imaging examination at the SST Dentofacial Clinic, Italy, were retrospectively selected. These image were acquired for reasons independent of this study and in all acquisitions the device was operated at 6-10 mA (pulse mode) and 105 kV using a X-ray generator with fixed anode and 0.5 mm nominal focal spot size. All images were acquired with cephalometric field of view (200 mm x 170 mm). All subjects were adult Caucasian women, aged from 37 to 74 years, without diagnosed craniofacial pathologies, who had teeth in both dental arches. No limitations was set to the presence of dental implants, dental fillings or even on particular dental treatments carried out before the radiological examination.

Image Processing: In order to standardize the structures in the CBCT data, the proposed method requires a single initialization step consisting in pointing the most inferior point of the mandibular bone. Currently, this is the only manual operation required; however, this is easy to automatize, provided a standard patient positioning on the scanner chin set. Next, the volume is cut off below the selected slice and the algorithm proceeds automatically in landmark identification. This simple step defines a common criterion for volume limitation capable of providing a coarse standardization of the structures.
Subsequently, to improve the accuracy of the segmentation procedures and to make it

Table 3.1: Landmark used in this study

Landmark	Abbreviation
Sella Turcica	S
Nasion	N
Left and Right Gonion	lGo and rGo
Anterior Nasal Spine	ANS
Pogonion	Pg
Menton	Me
Left and Right Orbitale	lOr rOr
Posterior Nasal Spine	PNS
Left and Right posterior maxillary points	lPM and rPM
Left and Right Upper Incisor	lUI and rUI
Left and Right Lower Incisor	lLI eLI
Left and Right Frontozygomatic Point	lFz and rFz
A Point	A
B Point	B
Basion	Ba

robust to the presence of noise, the image was filtered using a three-dimensional low pass Gaussian filter. The size of this cubic filter was set to 3 voxels in order to limit the blurring effect, increase signal to noise ratio and preserve the morphology of craniofacial bones [67].

Image Segmentation: The segmentation algorithm aims at a standard hard-tissue thresholding, though after a subject-specific adaptation with no manual interaction and no training dataset or previously developed models. A major consideration driving the algorithm design was that CBCT scanners provide less calibrated contrasts than CTs, thus reducing the confidence in pre-set thresholds [68].

This aim was approached by k-means clustering separately performed on a representative subset of the volume slices.

Given a set of observation the *K-means* clustering aims to partition N observations $\mathbf{x}_n$, where n runs from 1 to N, into K sets by minimizing the sum of euclidean distances between all observations belonging to the same cluster and their mean (or centroid) $\mathbf{m}_k$. Each observation $\mathbf{x}$ can have J components x_j, in this case each observation is a mono-dimensional vector representing the intensity values of the image voxels.

K-means is an iterative algorithm which divides the given observations into a set of clusters following these steps:

1. **Initialization**: the centroids $\mathbf{m}_k$ are initialized to random values.

2. **Assignment step**: each data point is assigned to the nearest mean. In the following equation the guess for the cluster k_n that the observation $\mathbf{x}_n$ belongs to is denoted by $\hat{k}_n$.

$$\hat{k}_n = \underset{k}{\operatorname{argmin}}\{\|\mathbf{x}_n - \mathbf{m}_k\|\} \tag{3.1}$$

   Then in this step, the variables $r_{n,k}$, called responsibilities, are set following this relationship:

$$r_{k,n} = \begin{cases} 1, & \text{if } \hat{k}_n = k \\ 0, & \text{if } \hat{k}_n \neq k \end{cases} \tag{3.2}$$

3. **Update step**: the means are adjusted to match the sample means of the data points that they are responsible for

$$\mathbf{m}_k = \frac{\sum_n r_{k,n}\mathbf{x}_n}{R_k} \tag{3.3}$$

   where R_k is the total responsibility of mean of the cluster k,

$$R_k = \sum_n r_{k,n} \tag{3.4}$$

   In this way, when $R_k = 0$ the corresponding mean remain at its original value.

4. **Optimization step**: the assignment step and update step are repeated until the assignments do not change [69].

In particular, the k-means clustering was chosen due to its low sensitivity to initialization parameters, relatively low computational complexity and its suitability for biomedical image segmentation since the number of clusters can be easily defined based on prior anatomical knowledge [70, 71].

The present validation considered a 1:2 reduction, by analysing each second slice; however, further preliminary trials revealed that higher reduction factors improved efficiency with no accuracy loss. As detailed below, the statistics of clusters was used to set the optimal soft/hard tissue separation threshold; also, a good robustness against dental metal artifacts was achieved by proper elimination of low-density outliers. Within each subset, slice tissues were classified into 4 main categories, one representing air, two representing soft tissues and one representing hard tissues. The classification was performed using a k-means clustering approach [72]. The following statistics through the subset of slices considered

the minimum of the highest intensity cluster; i.e., the one intended to classify bone and tooth tissue.

These values allowed to determine the global threshold which was defined at the 10th percentile of the population of minima. This threshold value was shown to make the algorithm robust to misclassification of tissues in a limited (i.e., less than 10%) number of slices that are easily classified as outliers. The 10% rule was shown selected to avoid a specific search of outliers.

After the optimized threshold value was obtained, it was possible to proceed with the thresholding of the entire volume that needs to be segmented, since preliminary analyses confirmed that possible intensity calibration trends through slices were negligible. The outcome of single voxel thresholding was next improved by removing all the residual volumes of the segmentation process, caused by the presence of noise or artifacts. A 3D labelling process identified all structures and those presenting a volume lower than 0.1% of the total segmented volume were eliminated. An example of the outcome of the segmentation process is shown in Figure 3.4.

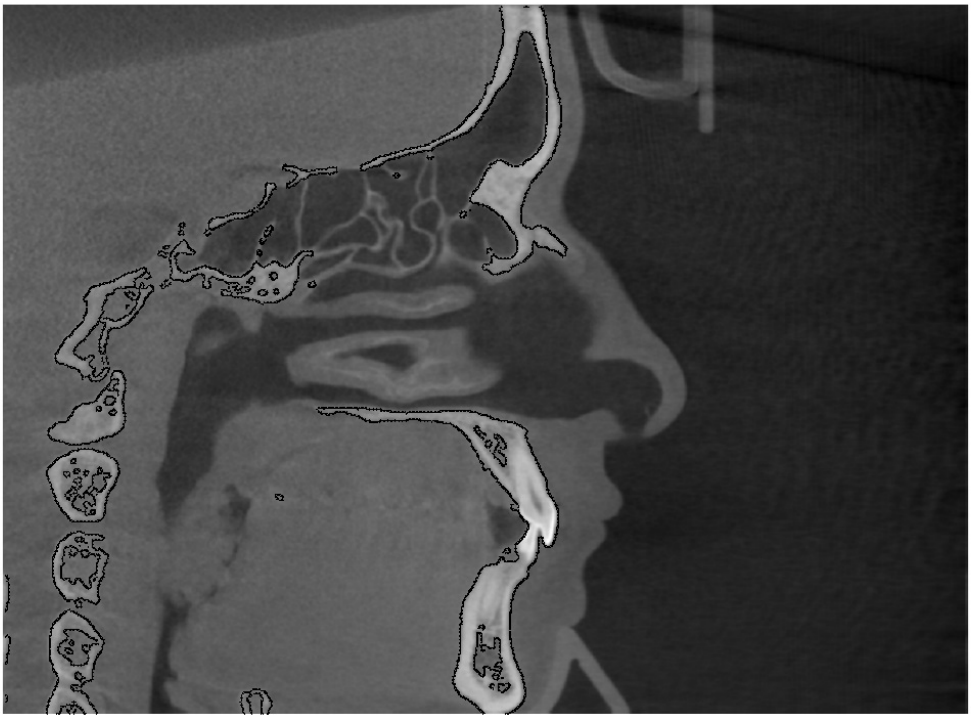

Figure 3.4: The figure shows, in a median sagittal slice, which structures are maintained during the segmentation process

Image Registration: Landmark placement was based on the propagation of landmarks through the registration on an annotated reference skull. The reference skull was automatically segmented with the above presented method and annotated in a double blinded process by three expert operators for three times, in order to take into account intra and inter-operator variability. Each operator had at least 4 years of experience in morphological evaluation of the skull. To allow the user to annotate the reference skull a GUI was created using MATLAB. This GUI allowed the user to annotate the skull visualizing MPR views. Once all the operators performed the annotation the center of mass of all annotations was used as final landmark positions.

In previous investigations, deformable registration approaches have been used to align corresponding structures in different images in order to estimate anatomical landmarks, as such methods take into account the global appearance information of the anatomical structures [73–75]. During this step, segmentation for both subject and reference was used for masking only, thus keeping the information of gray levels inside the segmented bone. Registration was started by affine transformation that, being global and linear, permits re-scaling according to the individual proportions and also allows a robust compensation of the different volumetric FOVs occurring in CBCT. Its transform is expressed by:

$$F : \mathbf{x}_F \in \Omega_F \mapsto F(\mathbf{x}_F)$$
$$M : \mathbf{x}_M \in \Omega_M \mapsto M(\mathbf{x}_M)$$

where $F(\mathbf{x}_F)$ is an intensity value of the image F at the location $\mathbf{x}_F$ and $M(\mathbf{x}_M)$ is an intensity value of the image M at the location $\mathbf{x}_M$ [76].

The MSD was applied as registration objective function to be minimized. This cost figure is defined as follows:

$$\text{MSD} = \frac{1}{N} \sum_{\mathbf{x}_F \in \Omega^{\mathbf{T}}_{F,M}} |F(\mathbf{x}_F) - M^{\mathcal{T}_\text{a}}(\mathbf{x}_F)|^2 \tag{3.5}$$

where $\mathbf{x}_F$ represents the voxel locations in image F and $\mathbf{T}_{F,M}$ represents the overlap domain consisting of N voxel subset.

Trilinear interpolation was applied in computing the transformed image gray levels and an iterative gradient descent algorithm was applied to find the optimal transform:

$$R_\text{a} = M^{\mathcal{T}_\text{a}} = \mathcal{T}_\text{a}(M) \tag{3.6}$$

The affine registration (linear) step was used as initialization of a subsequent elastic registration (nonlinear). Importantly, the algorithm was designed to avoid deformations due to the presence of different anatomical structures in the image volumes; which were caused by

the limited field of view of CBCT images and inter-subject morphological variability. This problem was solved by shrinking the subjects mask to the overlap subset TF,M found after the first affine registration step, thus cutting out the individual volume in excess to the reference volume. Then, the skulls were processed with a subsequent step of intensity-based global elastic registration, by MATLAB Medical Image Registration Toolbox, MIRT, Free FFD with three hierarchical levels of B-spline control points [77,78]. A wide mesh window size between the B-spline control points of 15 voxels was set, in order to register the main skull features while avoiding deformation relevant to the largely varying bone structure details and to artifacts. As a result, the number of control points varied for each image, depending on its size.

Moreover, in order to prevent the mesh to get too much deformed, a regularization term was used. In particular, the Euclidean distance between all the neighbouring displacements of B-spline control points was penalized [77]. In our algorithm, the regularization weight was set to 0.1. Both mesh window size and regularization weight were empirically determined to give the best performance in term of accuracy.

Like the affine one, the elastic registration was an iterative process, which optimizes the MSD voxel similarity measure using a gradient descent optimization method with 3 hierarchical levels of optimization. This additional transformation Te is defined as:

$$R_{\mathrm{e}} = \mathcal{T}_{\mathrm{e}}(R_{\mathrm{a}}) \tag{3.7}$$

An example of the outcome of these registration steps is depicted in Figure 3.5, which shows how the elastic registration allowed to better adapt the morphology of the reference skull to the patient's one, compared to the affine step.

Landmark Estimation: Through the registration phase the algorithm superimposes and deforms the reference skull to comply with the morphology of the patient using only the information provided by the intensity values of the segmented CBCT images.

Such process is geometrically defined by the transformations $\mathcal{T}_{\mathrm{a}}$ and $\mathcal{T}_{\mathrm{e}}$, that can be applied to the coordinates of cephalometric landmarks annotated on the initial reference skull to estimate the same cephalometric landmark positions on the patient's one.

Regarding the affine transformation, it is possible to derive the geometric transformation $\mathbf{T}_{\mathrm{a}}$ corresponding to the image transformation $\mathcal{T}_{\mathrm{a}}$ and apply it to the matrix of the reference landmark coordinates.

Defining the position of the *i-th* landmark in the reference system as $\mathbf{p}_i$, where i runs from

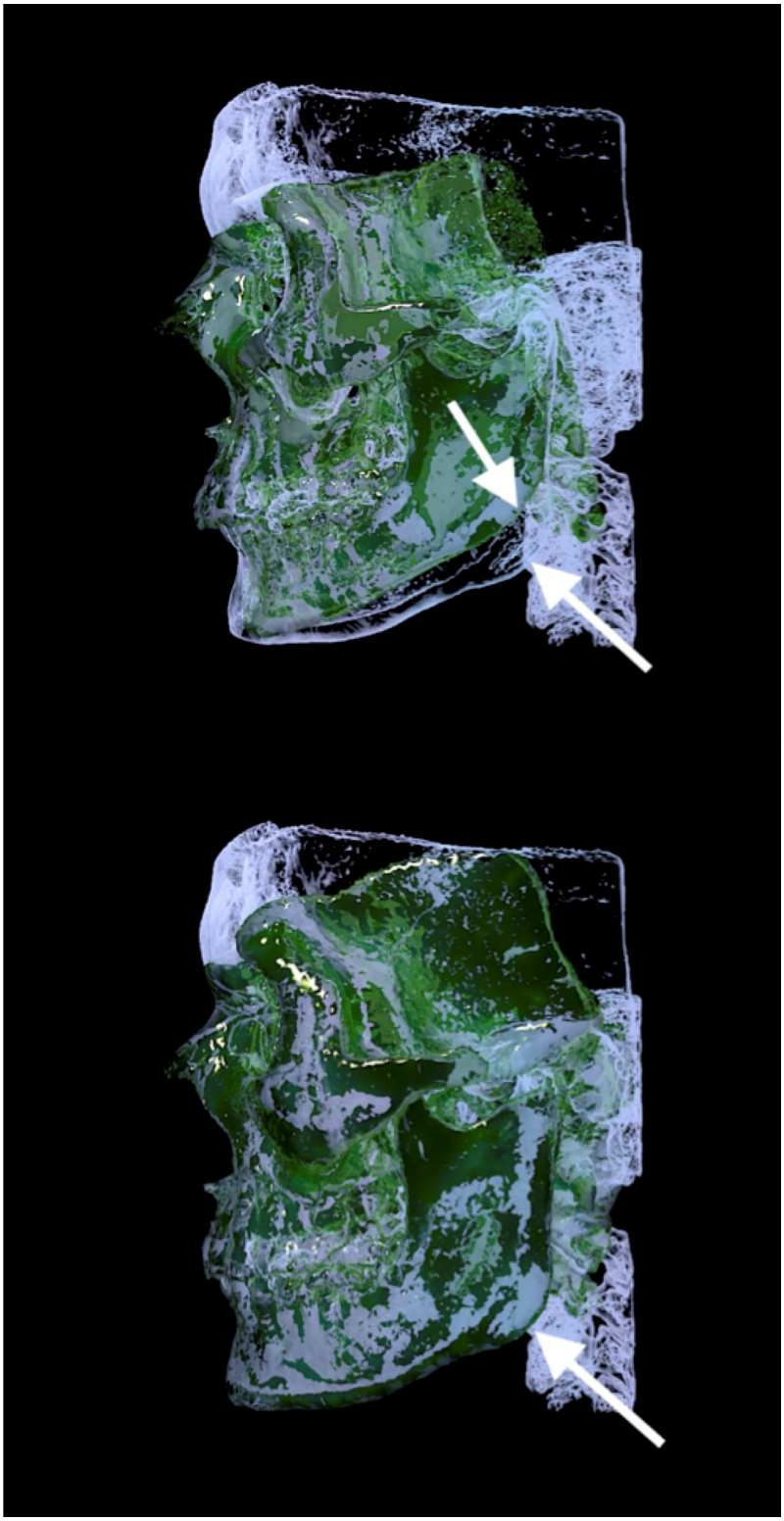

Figure 3.5: Example of affine registration (above) and affine + elastic registration (below). Median sagittal view of the segmented subject skull (light) with the register. Arrows indicate the mandibular region, which is fully registered after the elastic segmentation step

1 to 9, the new estimated position of the same landmark on the transformed reference skull, and expressed in the patient's reference system, $\hat{\mathbf{p}}_i^{\mathrm{a}}$ can be calculated as follows:

$$\hat{\mathbf{p}}_i^{\mathrm{a}} = \mathbf{T}_{\mathrm{a}}\mathbf{p}_i \tag{3.8}$$

The elastic transformation Te was implemented numerically on a zeros volume, the size of the original volume, marked with a single 1 at the landmark position. The transformed image was no more binary and the center of mass coordinates were taken as transformed landmark coordinates. The 21 landmark coordinates were collected in a vector p_e representing the final estimation of the chosen cephalometric landmark coordinates. At the end of the annotation process each annotated landmark is displayed on the 3D surface of the patient skull. Moreover each landmark is centered into a spherical confidence region that helps the clinician during a subsequent eventual manual refinement of the annotation, as can be seen in Figure 3.6. The radius of the confidence spheres was set to the 95th percentile of the annotation error population calculated during the validation step.

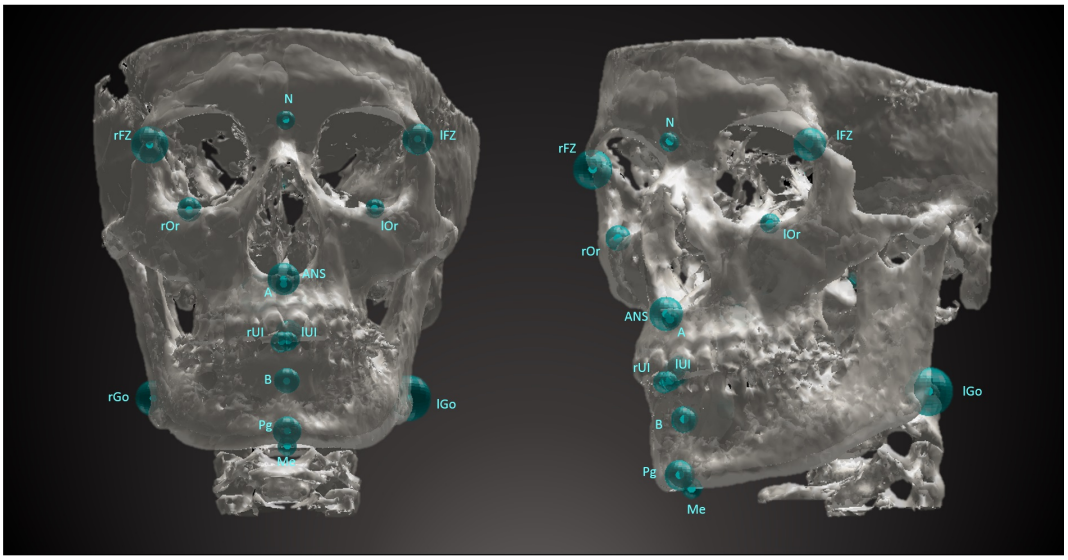

Figure 3.6: Example of the proposed, computer aided, annotation process outcome; each landmark is centered into a spherical confidence region (95th percentile of the annotation error population) that can help the clinician in a subsequent manual refinement of the annotation

Validation: Optimized thresholding, though preliminary to registration and automated annotation, was considered a crucial step deserving a specific validation. Therefore, the algorithm outcomes were compared to the manual thresholding performed by an experienced user on the whole data set. Both threshold values and segmented volumes were compared

testing correlation and significance of differences of automatic vs. manual identification. Depending on the normality of data, either Student's t-test or Wilcoxon signed rank test was used; p-value significance level was set to 0.05. The normality of data distribution was checked with Jarque-Bera test; also in this case significance level was set to 0.05.
To evaluate the quality of the annotations performed in this study all CBCT volumes were manually annotated. In particular, in order to take into account the inter-operator variability of the annotation process a team of expert users manually annotated the image dataset. This way, for each subject, the expected location of the 21 cephalometric landmarks can be defined as the barycenter of operator annotation. Figure 3.6 shows an example of manually and automatically annotated landmarks.
Subsequently, the Euclidean distance, expressed in mm, between the position of each manually annotated landmark and the position of its corresponding landmark estimated by the proposed algorithm, was calculated. These distances will be subsequently used to display confidence regions around the estimate landmarks in order to allow the user to easily place the landmark in the most suitable place.

Results

Segmentation: To evaluate the accuracy of the segmentation process, both threshold values and segmented volumes where compared. Both manual and automatic threshold values resulted normally distributed ($p > 0.05$). They were highly correlated ($R = 0.96$, $p < 0.001$) and no significant difference was found between them ($p > 0.05$), thus indicating that the automatic optimization well reproduced the threshold setting of experts.
Segmented volume values resulted not normally distributed ($p < 0.05$), and non-parametric tests were used for their statistical comparisons. Even for these values, a high level of accuracy was found between automatically and manually segmented volume values ($\rho = 0.98$, $p < 0.001$) and no significant differences were found between the two groups ($p > 0.05$).

Landmark Estimation: The mean (SD) inter-operator ICC for all the analysed landmarks was 0.98 (0.04). The overall median value of the computer-aided localization error was equal to 1.99 mm with an IQR of 1.22 - 2.89 mm.This median error expressed in the horizontal, vertical and transverse direction was equal to 0.60, 0.86 and 0.89 mm, respectively. These distances widely varied among different landmarks. In particular, among the calculated estimation errors the lowest value was reported for the PNS landmark with a median value of 1.47 mm and an IQR of 0.79 - 1.76 mm. On the other hand, the highest

values were observed for Gonia, respectively, right Gonion with a median value of 2.81 mm and an IQR of 1.46 - 4.83 mm and left Gonion with a median value of 4.00 mm and an IQR of 2.00 - 4.86 mm.

Considering all landmarks, annotation error was less than 5.00 mm for 90 % of landmarks and less than 2.50 mm for 63 % of them.

The descriptive statistics for the obtained distances for each landmark are shown in Figure 3.7.

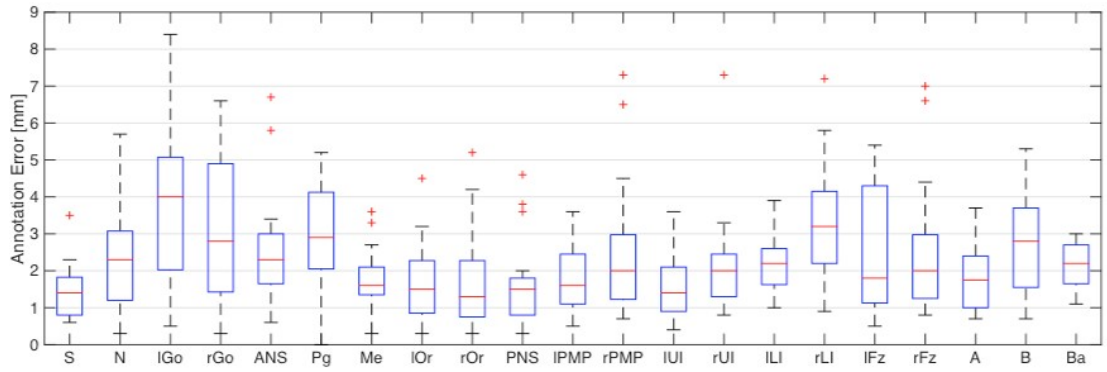

Figure 3.7: Annotation error, calculated as the Euclidean distances between manually annotated and estimated landmarks, for all the analyzed landmarks.

Conclusion

The proposed method allows to find a good estimate of landmark positions, which may subsequently be refined by the clinician, saving operator time and reducing annotation variability.

Nowadays the annotation of cephalometric points is mainly performed manually. Recent studies reported that the error caused by identification of landmark varies between 0.02 mm to 2.47 mm [58–60, 79]. Therefore, one important aim for the evaluation of skeletal morphology in maxillofacial patients is to reduce the landmark identification error under 2.00 mm [79].

In the present study, landmarks lying in different locations present largely different average localization errors. Using our method, Gonia arise as the most difficult markers to localize. As a matter of fact, this reflects the variability of human anatomy and manual annotation. The mandibular bone, statistically, is among the most variable bones of the skull [80] and this is reflected in the estimation of right and left Gonion [81].

In this study, since annotation errors were not normally distributed among different pa-

tients ($p<0.001$), the median annotation error was used to measure the accuracy of the annotation process. In particular, the median annotation error was found as 1.99 mm with an IQR of 1.22 - 2.89 mm. In a recent study, Shahidi et al. validated an algorithm for landmark annotation based on 3D image registration for 14 landmarks on a dataset of 20 CBCT images. They obtained an overall mean error of 3.40 mm, which is significantly higher compared to the one obtained with the current method [64]. In another study, Gupta et al. proposed a knowledge-based algorithm for automatic detection of cephalometric landmarks on CBCT images that was validated on 30 CBCT images. Gupta et al. obtained a mean error of 2.01 mm with a standard deviation of 1.23 mm, which is comparable with the one obtained with the proposed methodology [48]. With our method a comparable accuracy level was obtained with reduced a priori information about landmark positions.

The method described in the present study attempts a general and robust approach for the propagation of landmarks from an annotated reference skull to subject-specific ones. Segmentation of hard tissues is a fully automatic process that reduces the amount of error dependent on operator experience. In the validation step, no significant difference was found between manually and automatically determined threshold values. Moreover, the correlation coefficient close to 1 proved the high accuracy of the segmentation step compared to manual thresholding, which is now considered the standard method of segmentation in maxillofacial applications.

Since the segmentation step was proved to be very robust, the registration step represents the main source of variability in automatic annotation. In order to improve the annotation accuracy, local adaptation in a region of interest around each estimated landmark should be added to overcome the limits of the global registration step. Moreover, we believe that a computer aided cephalometric annotation of CBCT volumes, relying on intensity-based image registration, can be a good initialization that can help the clinician in performing cephalometric analysis. Indeed, for most landmarks the current results are well comparable with those provided by other methods present in the literature [62,63]. One advantage of our method is that cephalometric landmark coordinates were obtained without any local a priori information about geometry and location of each landmark, allowing physicians to use this approach for personalized cephalometric analysis. Indeed, the method can be customized only changing the number of landmark annotated on the reference skull, without any modification of the annotation algorithm. Results are promising, nevertheless the study should be expanded in order to validate it on a larger dataset and reduce the

estimation error to provide a fully automatic annotation algorithm. Moreover, in order to improve the segmentation and, consequently, the annotation in the dental region, a dedicated high intensity object artifact reducing algorithm should be implemented.

3.3 Metal artifacts in CBCT images

3.3.1 Quantitative evaluation of metal artifact using different CBCT devices, high-density materials and field of views

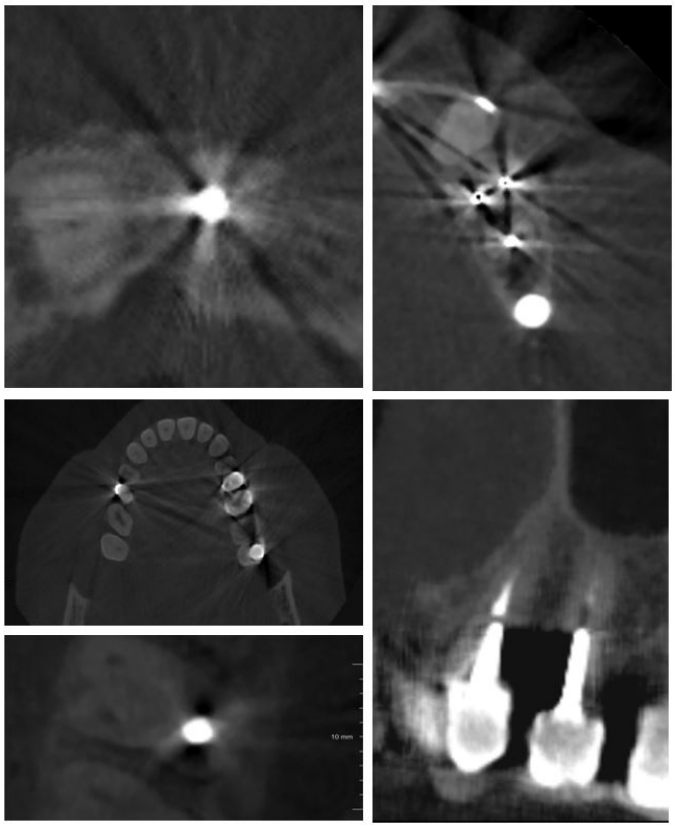

Figure 3.8: Examples of the effetc of metal artifacts on CBCT images

Since the advent of CBCT, attempts to quantify image artifacts have gained importance. For this reason, in the last years, research focused on the evaluation of the factors that influence artifact expression in CBCT images in order to better understand how to analyse and improve corrupted images [37, 82, 83].

Artifacts can be seen in the reconstructed images and several etiologies has been reported in the literature [32,35]. Among the possible causes of artifacts, beam hardening is described as the most common; followed by the dispersion of photon noise and motion artifacts [84]. One of the main causes of artifacts is the presence of high-density materials within the FOV, such as metal implants, intracanal posts, metallic crowns and amalgam restoration. The literature has demonstrated that metal artifacts have negative influence in the daily diagnosis. In particular, their presence influences root fractures diagnosis in CBCT images in presence of intracanal materials and metal posts [85–89]. Some examples of the effect

of metal artifact on CBCT images are depicted in Figure 3.8. This negative influence is due to the appearance of artifacts mimicking the fracture lines disturbing the diagnostic process, leading to an incorrect diagnosis and treatment plan and in some cases to unnecessary extraction.

Similar limitation may occur when looking for the dental implants surface. Despite the CBCT provides accurate information related to bone morphology and guidance on the positioning of the implant in the alveolar ridge [90], the peri-implant region can be compromised by the presence screw artifacts hindering or even making impossible the diagnosis in this region [82, 91].

High density materials can create artifacts that affect image quality in different ways depending on the CBCT device [36] and imaging protocol. For this reason, acquisition parameters, detector type and reconstruction algorithms are important parameters that must be taken into account while evaluating image quality in terms of image noise, contrast resolution and artifacts [92].

Given the influence of such factors on artifact generation and in order to better understand their expression in CBCT images, the aim of the present research was to develop a quantitative method to assess the effect of different CBCT devices, materials and FOV sizes on metal artifact generation.

Materials and Methods

Phantoms

For this study, three acrylic resin phantoms (VIP, São Paulo, Brazil) were manufactured. Each phantom contains three cylindrical pins, made with different high-density materials: titanium, copper-aluminum alloy (CuAl) and amalgam. These metal pins were positioned at the vertices of an isosceles triangle to mimic the position of the central incisors (A) and seconds molars (B and C) in a human mandible. Phantom geometry and composition is described in Figure 3.9.

The dimensions of the metallic cylinders were checked with an electronic digital caliper (0-150 mm Stainless, Hardened) before their inclusion in the resin phantom. Moreover, their correct position inside the phantom was certified using a comparative microscope (Olympus Optical CO, LTD, Japan), in order to standardize the geometry of all phantoms.

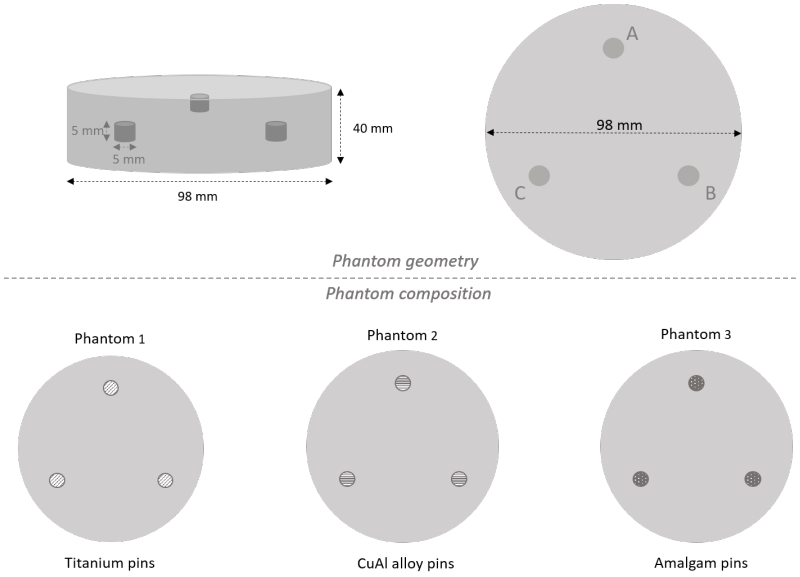

Figure 3.9: Geometry and composition of the phantom used in this study

CBCT parameters

All phantoms were scanned using hi-resolution parameters, fixing the spatial resolution to 0.2 mm and choosing one representative large and small FOV for each CBCT devices: 3D Accuitomo 170 (J. Morita, Kyoto, Japan); ProMax 3D (Planmeca Oy, Helsinki, Finland) and Newtom VGI evo (Newtom, Verona, Itlay). All exposure protocols are shown in Table 3.2.

Table 3.2: Exposure protocols for the CBCT devices included in this study

	ID	FOVs (cm)	kVp	mA	exposure time (s)	voxel size (mm)
3D Accuitomo 170	CBCT1	4x4/10x5	90	5.0	30.8/17.5	0.2
NewTom VGI evo	CBCT2	5x5/10x5	110	3.0	1./1.8	0.2
ProMax 3D	CBCT3	5x5/10x5	96	5.6	12/12	0.2

Image analysis

During image analysis, for each combination of CBCT device and material, the images acquired with the 2 different FOV were analyzed.

At first, to quantify the effect of metal artifact on image quality, the metal cylinders were segmented in both images. To automatically segment them, all the voxel were classified in 3 categories (air, acrylic resin and metal) using a three-dimensional k-mean clustering

approach [93]. Then, the voxels belonging to the most intense cluster were classified as metal.

After the segmentation, in order to select the same ROI, in both images, the small FOV image was registered to the one acquired with the large FOV. This registration was performed automatically and was divided in two steps. The first step consists in the estimation of the initial translation transformation that allow to roughly register the two volumes. During this step, the metal cylinders in B position, which were present in both images, were automatically detected in order to calculate their barycenter and estimate the initial transformation. After this initialization step, a fine intensity-based registration step was used to register the volumes. For this registration step the normalized mutual information was used as registration metric [94].

Once the volumes were registered, the same ROI was selected. The ROI was automatically defined as the portion of the acrylic resin phantom that was imaged in both the registered volumes. All the acquired images were analyzed using Matlab (MathWorks, Natick, USA). The flowchart of the presented image analysis process is depicted in Figure 3.10.

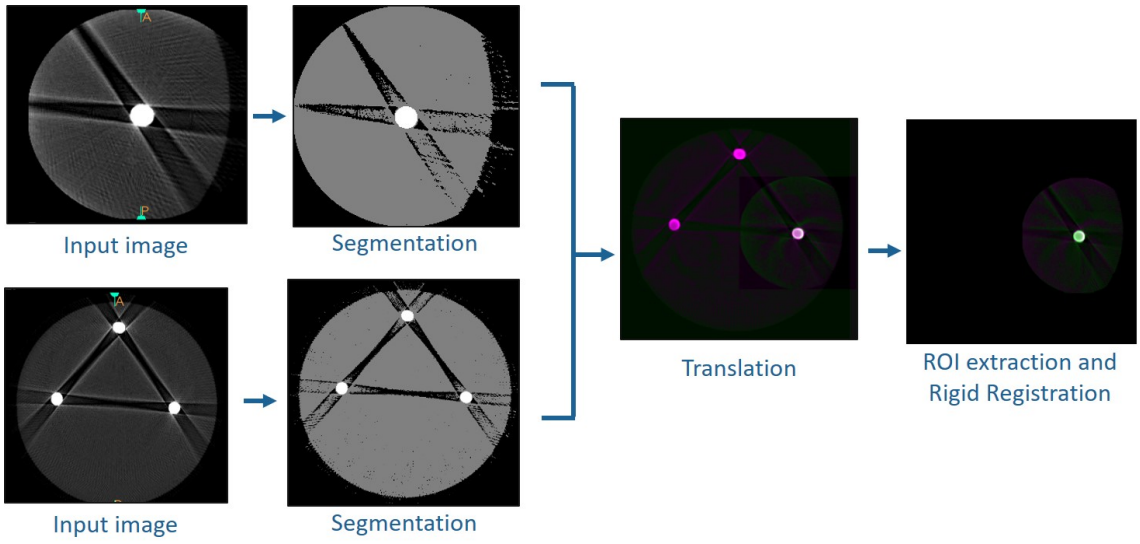

Figure 3.10: Flowchart of the image processing process used to estract the same ROI from the images obtained for each combination of CBCT device, material and FOV

Within the selected ROIs, to evaluate how the metal cylinder geometry was corrupted by metal artifacts, the difference between the segmented volume and the real volume of the metal cylinder (VD), expressed as percentage of the real volume, was calculated.

On the other hand, to evaluate the impact of the metal artifact in the surrounding voxels, the voxels segmented as metal were removed from the ROI. Once removed, the original

ROI was divided into three sub-ROIs. In these way, the amount of artifacts was evaluate taking the distance between the surrounding voxels and the metal object into account. Figure 3.11 shows an example of ROI division.

To quantify the amount of the artifacts in these regions, the nSD was used (Pauwels et al. 2013). In particular, the SD of the voxels contained therein the ROI was normalized to the maximum possible SD, which is defined as half or the full grey value range, allowing us to compare different CBCT devices with different gray value ranges.

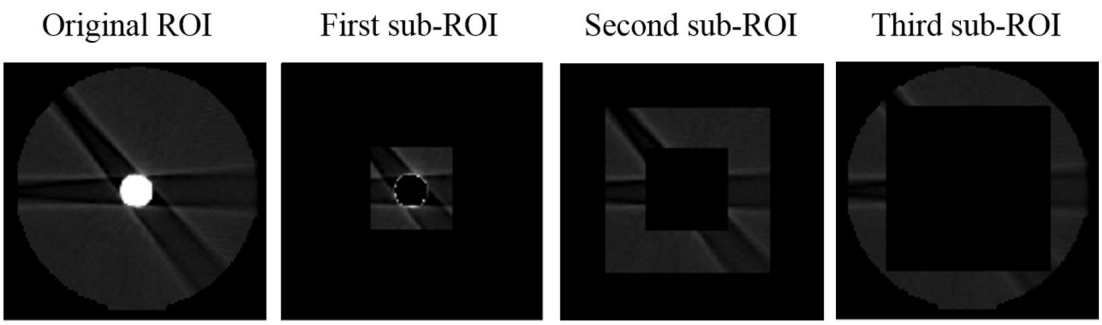

Figure 3.11: Example of ROI subdivision showed in an axial slice

Statistical analysis

Data were analyzed with a three-way ANOVA model, with CBCT device, material and FOV as three crossed factors. Since there is only one measurement for each combination for the volumetric measurements and nSD of the different ROIs, a solution was found by confounding the three-way interaction factor with the error term. Any difference between measured values that may point to a three-way interaction was explained by experimental error. Level of statistical significance was set for p-value < 0.05.

Results

Differences between segmented and real volume were observed for all CBCT devices and materials, see Table 3.3. Within the materials, amalgam generated the strongest artifacts while titanium generated the lightest. Statistical differences were found among different materials for different combination of CBCT devices and FOVs. Moreover, statistical differences were found in volume overestimation when varying CBCT devices, but not when varying FOV size.

The most accurate segmentation (0.2% of volume overestimation) was found for a Tita-

nium pin, acquired with CBCT1 using a small FOV. On the contrary, the least accurate segmentation was obtained for an amalgam pin, acquired with CBCT3 using a large FOV (67.0% of volume overestimation). In Figure 3.12 the differences between segmentation for each combination of CBCT device, material and FOV are shown.

For A_D values, significant difference was observed for all combinations of FOV, CBCT

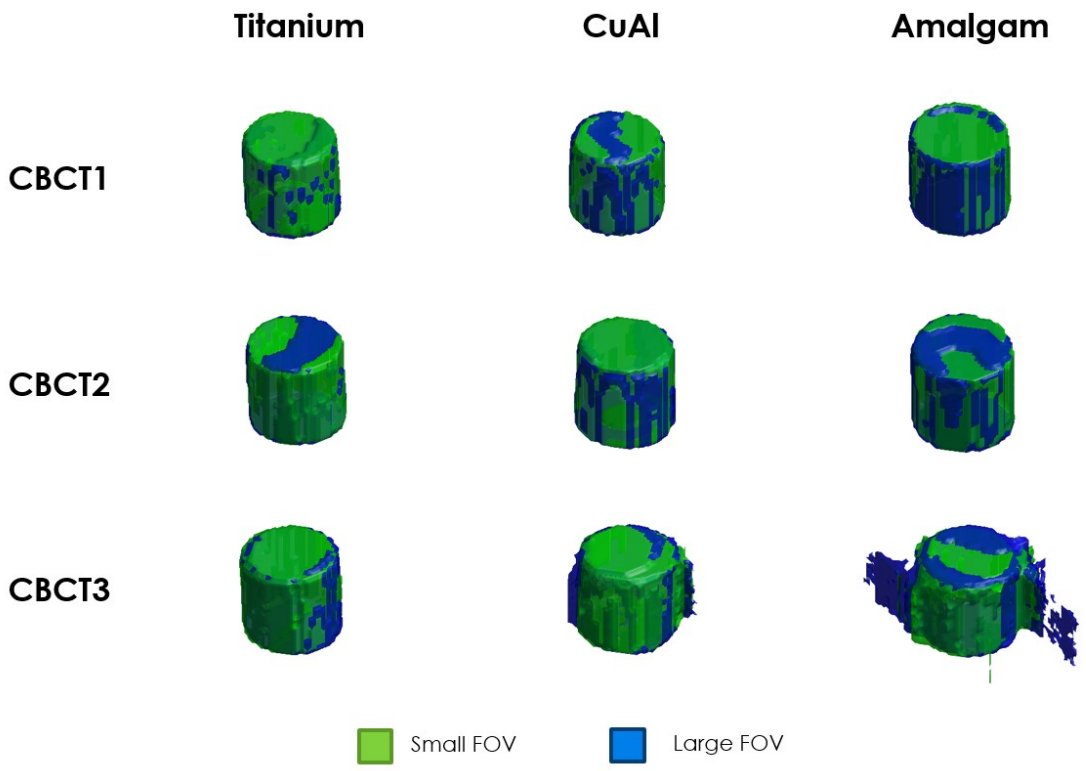

Figure 3.12: Segmented volumes for all the combinations of CBCT devices, materials and FOV

Table 3.3: VD values (%) for all the combinations of CBCT device, material and FOV

		CBCT 1	CBCT 2	CBCT 3
Titanium	LFOV	3.7	2.1	23.1
	sFOV	1.7	0.2	22.3
CuAl	LFOV	-6.0	-2.6	27.9
	sFOV	-7.1	-5.4	25.3
Amalgam	LFOV	15.6	12.3	67.0
	sFOV	13.8	8.6	60.2

device and material. The results of this analysis are summarized in Table 3.4. Normalized

Table 3.4: Median and interquartile range of A_D values (%), for all the combination of CBCT device, material and FOV

		CBCT 1	CBCT 2	CBCT 3
Titanium	LFOV	4.4 (0.6)	2.8 (1.9)	17.5 (0.6)
	sFOV	3.3 (0.8)	1.8 (1.2)	17.1 (1.1)
CuAl	LFOV	-0.8 (3.5)	0.6 (3.5)	23.0 (7.5)
	sFOV	-2.2 (4.7)	-1.4 (4.8)	23.6 (7.7)
Amalgam	LFOV	13.6 (3.0)	16.0 (1.4)	61.5 (17.0)
	sFOV	11.2 (1.1)	14.0 (2.1)	53.6 (10.4)

standard deviation varied differently between the three ROIs in each device (Table 3.5). There was no significant difference between materials for all combinations of CBCT and FOV ($p>0.05$). Only CBCT3 showed significant difference in nSD values for all combinations of FOV and materials ($p<0.05$). Finally, the small FOV in all the CBCT devices showed statistical significant differences ($p<0.05$).

Discussion

The present study showed the influence of different high density materials, CBCT devices and FOVs on the image quality, using a novel and fully objective method.

In CBCT images, grey values intensity is specific for each equipment due to the influence of technique factors inherent for each device. Usually, in modern CBCT devices, the acquired images are stored as 12-bit or 16-bit DICOM images. The difference in the number of stored bits lead to a different number of possible grey values, which is defined as $2^{(stored_{bit}-1)}$. To compensate these differences and be able to compare SD values from different CBCT devices, nSD was calculated [35].

Independently of this specific characteristic related to each CBCT device, the presence of high density materials produces severe artifacts in the reconstructed data. These artifacts are even worse when these materials are present in more than one place. In this case, the region between two objects is deteriorated, impairing the diagnosis.

Beam hardening is the most common cause of artifacts in CBCT related to the polychromatic source and especially, two types of artifacts can result from this phenomenon: dark bands or "photon starvation" between dense objects and cupping artifacts [95]. In the present study, both artifacts were observed in all the samples for all the materials reduc-

Table 3.5: nSD values (%) for all the combinations of CBCT device, material, FOV and sub-ROI

	CBCT 1						CBCT 2						CBCT 3					
	Amalgam		CuAl		Titanium		Amalgam		CuAl		Titanium		Amalgam		CuAl		Titanium	
	LFOV	sFOV	LFOV	sFOV	LFOV	sFOV	LFOV	sFOV	LFOV	sFOV	LFOV	sFOV	LFOV	sFOV	LFOV	sFOV	LFOV	sFOV
ROI 1	2.0	2.7	1.8	2.2	1.1	1.4	1.6	1.7	1.3	1.4	0.9	0.9	15.1	13.9	12.4	11.2	6.3	6.3
ROI 2	0.5	0.7	0.4	0.6	0.2	0.5	0.4	0.5	0.3	0.3	0.1	0.1	6.0	5.0	4.6	3.9	2.7	2.2
ROI 3	0.5	2.2	0.5	1.7	0.5	1.3	0.6	0.7	0.5	0.5	0.4	0.5	7.9	7.3	7.7	7.2	7.6	6.9
Total	0.6	1.9	0.6	1.5	0.5	1.3	0.6	0.8	0.5	0.6	0.4	0.4	8.1	7.4	7.5	6.9	6.6	6.1

ing the image quality. Several studies demonstrated that CBCT image quality can be improved by changing some parameters during scanning procedure, such as kVp [96–99], mA [100], FOV [101] and voxel size [102].

Therefore, in the present study, the protocols for each CBCT were carefully established. A fixed spatial resolution was selected to eliminate partial volume artifacts standardizing image quality analysis. However, even choosing similar protocols, the results showed statistical differences in volume measurements among CBCT devices. In particular, CBCT1 and CBCT2 seemed to have the same behaviour for all combination of material and FOV ($p>0,05$). On the other hand, CBCT3 showed significant differences compared to the other devices ($p<0.05$). This can be explained by the differences in operating characteristics of each X-ray tube. The latter varies with different voltage peaks and therefore, different effective beam energies. Despite choosing similar high resolution protocols, the presence of high-density material in the scanned volume originated severe artifacts.

In dentistry, a number of dense materials are currently in use which can differ in density and uniformity. In this study we used three different materials to evaluate the effect of their proprieties on metal artifact generation.

In particular amalgam, which is a heterogeneous material composed by mercury (Z=80), silver (Z=47), tin (Z=50) and zinc (Z=30), showed a different behaviour compared to CuAl (Copper Z=39 and Aluminum Z=13) and Titanium (Z = 22). The high density of this material compared to the others causes strong artifacts that lead to high volume overestimation during segmentation.

In this study, segmented volume analysis allow to globally evaluate the effect of metal artifact on metal cylinder segmentation. On the other hand the area analysis allowed to evaluate slice by slice if the over or underestimation was constant troughs the metal object. Our findings showed that amalgam had the highest values of median overestimation in interquartile range (IQR). In particular, the high value of median overestimation can be due to the high density of the material, that causes strong artifacts. In the same way, the high IQR values can be related to its heterogeneity that causes a large variability in AD values on different slices. This hypothesis is than confirmed by the values measured in the titanium cylinders, which is a homogeneous material with a lower atomic number, that showed the lowest values for both median and IQR of AD values. These results allow us to correlate the effect of metal artifact not only to material density, but also to their homogeneity.

Moreover, the area analysis allows to observe that the segmentation of the metal object

was mainly affected in the initial and final slices that compose the metal cylinders. This behaviour is common for all samples, highlighting a strong effect of artifacts at the vertical edges of the metal object. Probably, this can be explained by the divergence of the vertical beam in the extremes. The beam diverges from the ideal perpendicularity to the rotation axis and the detector. According to Molteni et al. a slight, but consistent increase in grey values intensity can be noticed moving toward the top (where X-ray beam increases divergence from an ideal orthogonal) [95].

The quantification of inaccuracy in metal object volume and area quantification can be of help for clinician during the evaluation of corrupted images, making them more aware of the amount of volume difference between the real object and the one imaged in the CBCT data. Regarding the amount of background, quantified using nSD, there was no significant difference in nSD values between materials for all combinations of CBCT and FOV ($p>0.05$), proving that the difference among materials affects more metal segmentation than background noise. Moreover, our results confirmed that amalgam, compared to the other two materials increased the SD of intensity of surrounding voxels. Similar finding were reported in a recent study that compared the SD values of intensity values in metal artifacts generated by amalgam and other composites [99].

The results of the present study showed also a significant difference between the three analyzed CBCTs, only in the small FOV. The presence of few artifacts in large FOV images may be explained by the scattered radiation and differences related to the scanning process (i.e., scanning geometry and image reconstruction and preprocessing).

For the small FOVs the presence of metal objects outside the reconstructed FOV should be one of the reasons for the differences between the devices. In general, smaller irradiated and reconstructed volumes are less prone to inaccurate voxel values, caused by scattered radiation and by non-ideal geometry [95]. The presence of metal objects outside the reconstructed FOV may be particularly problematic with limited-volume CBCT, for which only a small part of the head is within the reconstructed volume.

Conclusions

Different CBCT devices, materials and FOVs may affect the quality of resulting CBCT images. In particular, segmentation of a metal object was highly affected by the device and material factor, while FOV size seemed less important in this case. Regarding the background noise, CBCT devices and FOV size had more influence on the amount of artifacts than the materials.

3.3.2 Automatic hard tissue segmentation and metal artifact reduction in dental CBCT data

This project was financed by Cefla SC. The presented algorithm was then upgraded in collaboration with Cefla group and integrated in their imaging software. Details regarding the final version of this algorithm are not reported in this section, respecting the signed non-disclosure agreement.

In last decades, the use of CBCT devices has significantly increased. These devices allow to obtain high resolution cross-sectional images delivering a lower radiation dose to the patient, compared to a traditional multi-slice CT [66].
Cone Beam CT finds it main application in dental and maxillofacial applications, both in diagnosis and treatment planning, in particular when computer aided procedures are planned [34].
In this kind of applications, image quality plays a key role, since the accuracy of 3D models and manufactured surgical templates strictly relies on it [103]. Nowadays, CBCT images allow to create 3D models in a reliable and clinically applicable way, but there are some factors that can compromise model accuracy [104].
In craniofacial CBCT images severe corruption is caused by high-density objects, such as dental implants and dental fillings. The presence of metal artifacts worsens the image reconstructed by back-projection algorithms with bright streaks radiating from the metallic objects and with dark areas near them. The true contrast may be completely obscured in regions between adjacent metallic objects. Eventually, these artifacts may lead to misclassification of landmarks used for diagnosis, surgical planning and clinical follow-up [35].
Due to the clinical relevance of this matter, several efforts were made to reduce metal artifacts in CBCT images.
To reduce this kind of artifact, specific metal artifact reduction (MAR) algorithms, which allow improving image quality, were developed. These correction algorithms can be classified in three different groups: interpolation-based methods, iterative reconstruction approaches and adaptive filtering algorithms [38]. In the last years, specific MAR algorithms for CBCT images were developed [38–42] and now MAR solutions are available in some commercial devices. These solutions allow to improve image quality and consequently image segmentation and feature extraction.
In order to improve an automatic extraction of craniofacial features and cephalometric landmarks, currently in development by our research group, we designed a MAR solu-

tion. The new MAR step is fully integrated with our landmark detection software and exploits features of the preceding skull segmentation to limit the metal affected VOI to be corrected, with consistent computational saving.

Materials and Methods

Our automatic skull annotation algorithm starts with a hard tissue segmentation by a thresholding, driven by a k-means clustering performed on the first one out of every two slices. A vector of minima of the highest intensity cluster in each slice is computed. Then its 10th percentile is fixed as low threshold for the entire volume, thus assuming that at least 90% of the analyzed slices has no low-intensity artifact [44].
Once the original volume is segmented, the result may not be satisfactory due to the presence of strong metal artifacts. To reduce them, the algorithm automatically detects the corrupted volume subset.

This VOI was identified as a set of adjacent slices (slab) where the previous k-means clustering was affected by high intensity artifact caused by metal objects. To detect this VOI, the vector of intensity minima classified as hard tissue was used. When metal artifacts are present, this vector is characterized by abrupt changes in intensity values, since the 4th cluster is composed by metal voxels. A change of more than 500 grey levels was considered as threshold to identify the limits of the VOI. Figure 3.13 shows an example of change in minimum values that allows to automatically detect the VOI where the MAR

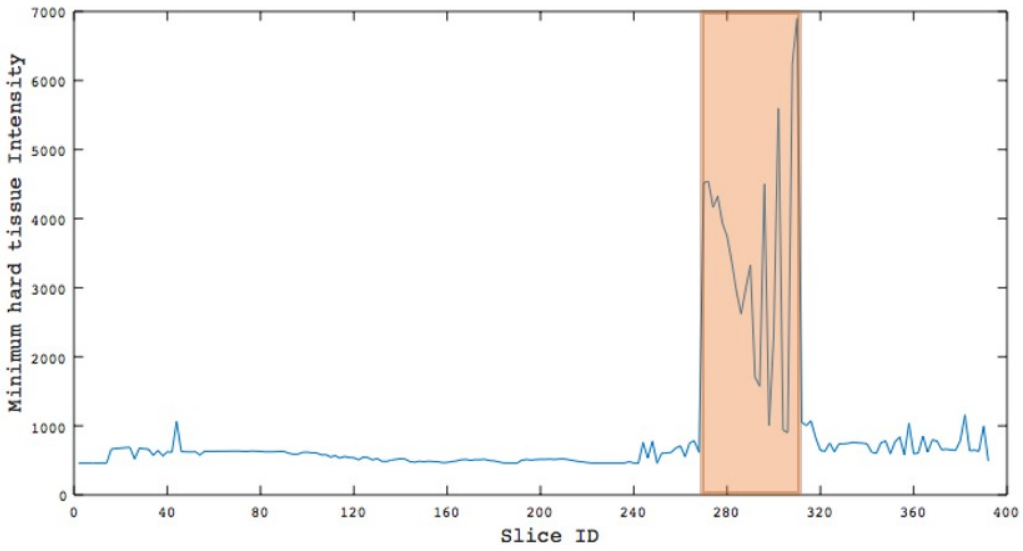

Figure 3.13: Example of automatically selected sub-volume from the original image volume

algorithm will be applied.

In this way, a new image volume is created using only a subset of the original image, which will be processed to reduce metal artifacts and improve its image quality. The proposed MAR algorithm works in 3D and starts with the segmentation of metal objects within the VOI by a three-dimensional k-means technique [105]. In this step, all the voxels segmented as bone were automatically classified in 6 clusters. Among them, the 2 most intense were classified as metal. This process was conducted only in the segmented part of the image, in order to save computational time and accurately detect all the metal objects.

After this process, the binary image containing only metal information was created. This metal image was then forward projected to obtain the metal trace in the image sinograms. For each slice contained in the VOI, the metal trace was identified using the metal image. Figure 3.14 shows an example of metal trace extracted from the VOI sinogram.

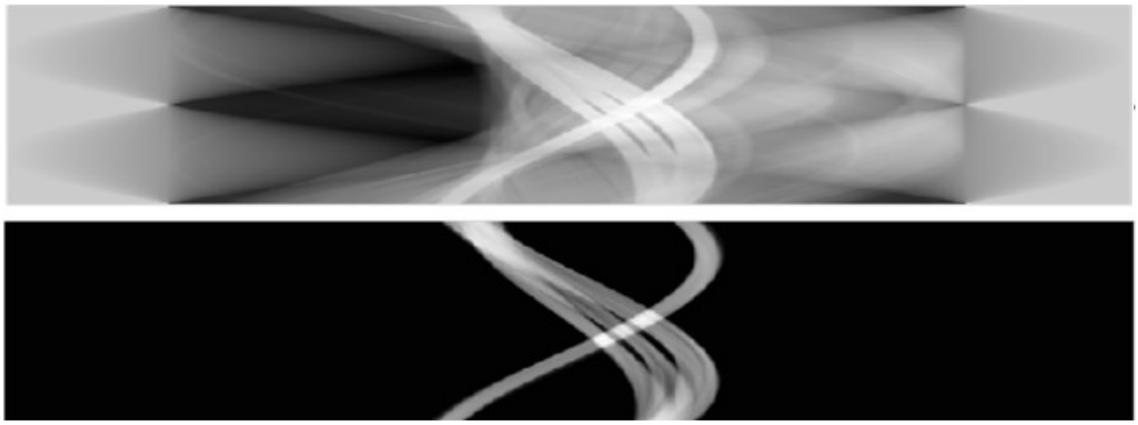

Figure 3.14: Example of metal trace (below) automatically estracted from the original stack of sinograms (above)

Once the metal trace was extracted, metal voxels were replaced in all sinograms to perform artifact suppression. During sinogram correction, in order to add the information provided from adjacent slices, the algorithm considers the series of 2D sinograms belonging to each VOI slice as a single volume.

MAR was performed in the 3D space of projections (approximately the stake of sinograms) to account for slice cross-talk. The proposed correction was non-linear, all the voxels corresponding to the metal trace are considered as missing data and filled by the 3D inpainting technique proposed by Garcia in 2010 [106]. Moreover, in order to reduce the streak artifacts, a 3 x 3 x 3 low pass 3D Gaussian filter is applied to the corrected sinogram [40]. Figure 3.15 shows an example of the results of sinogram correction.

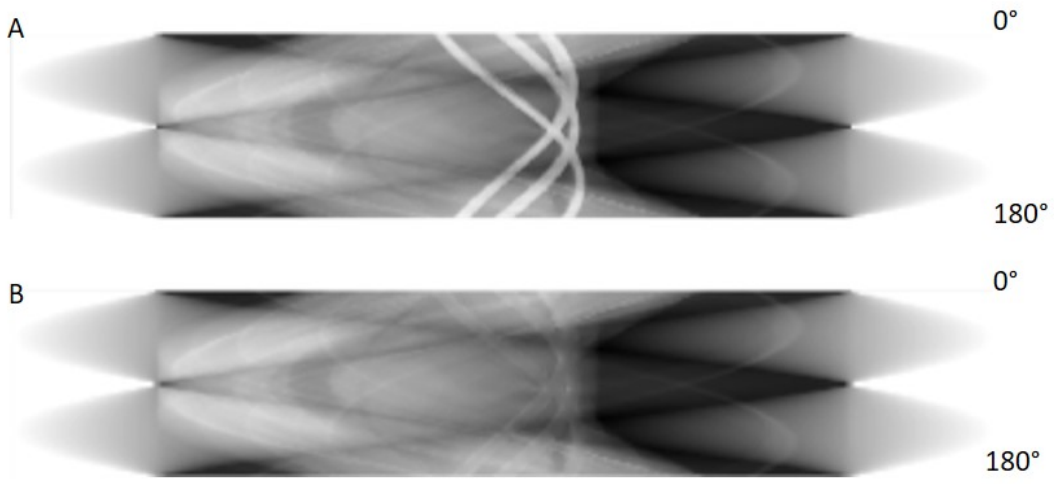

Figure 3.15: Example of sinogram correction after the application of the proposed MAR solution

After that, the corrected sinograms were backward projected and metal objects were replaced in their original position.

Finally, in order to reduce the low-pass filtering effect of forward projection and reconstruction steps, the difference image between the original and corrected reconstructed volumes was calculated. This difference image was then used to detect the voxels significantly modified by the MAR algorithm and those only smoothed by the low-pass filtering. The rationale behind this decision was that artifact correction should strongly change the intensity of those voxels corrupted from dark bands and streak artifacts. On the other hand, the smoothing effect should modify the intensity values to a lesser extent.

The smoothed voxels were then identified applying a threshold to the difference image, the threshold value was set to 5% of original intensities. Then, all voxels below this threshold value were set to their original intensity. In order to avoid abrupt changes of intensity values, a weight mask was created applying a low pass 3 x 3 x 3 median filter on the binary mask obtained after difference image thresholding.

To quantify the artifact reduction, a series of sub-VOIs around each metal object were extracted. The dimension of each sub-VOI was 40 x 40 x 20 voxels.

In each detected sub-VOI, the voxels classified as metal were deleted and the surrounding voxels were used to calculate the mean intensity of the non-metallic voxels and its SD. The percentage of SD reduction was used as image quality metric to quantify the metal artifact reduction [35].

Boxplots were used to represent the distribution of mean and SD intensity values of non metal voxels. Normality distribution of the data was tested using the Kolmogorov-

Smirnov-test, then Wilcoxon signed rank test was used to compare mean and SD values before and after the application of the MAR algorithm. Significance level was set to $p<0.05$.

Results

The algorithm was tested on 17 CBCT volumes with a total number of 245 analized VOIs. All images were provided by Cefla and used as validation set. For each volume, the algorithm qualitatively improved the image quality, reducing both streak artifacts and dark areas. Figure 3.16 shows some examples of images before and after the application of the proposed MAR solution.

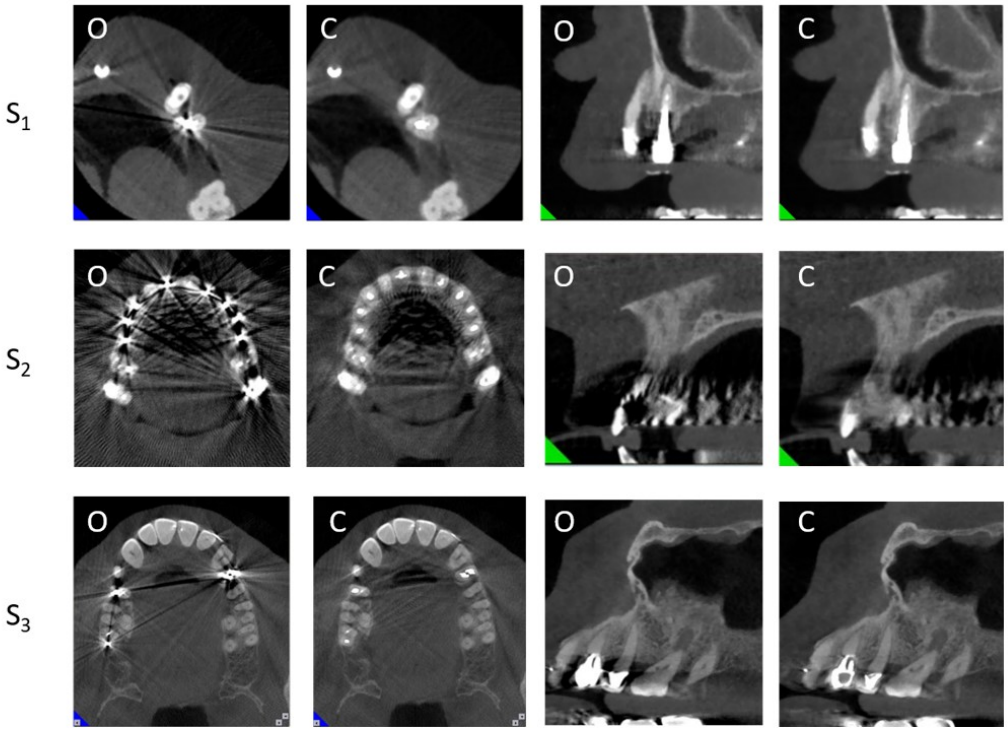

Figure 3.16: Examples of original (O) and corrected (C) images before and after the application of the proposed MAR solution

The mean intensity value (and its SD) across the sub-VOIs, both expressed in grey levels, were 2318 (1949) before and 2120 (1408) after image correction, with a median SD reduction percentage (and IQR) value of 22%(24%). Both mean and SD intensity values of the surround metal voxels were significantly reduced using the proposed MAR algorithm. ($p < 0.001$). The comparisons were performed using the signed rank sum test. Figure 3.17 shows the populations of standard deviation and mean intensity values measured in all the selected MS-VOIs.

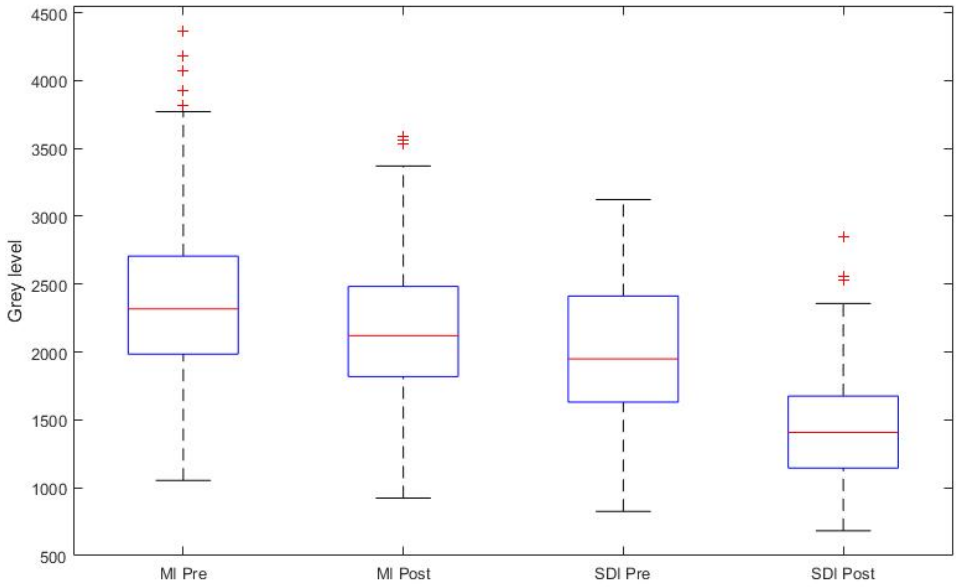

Figure 3.17: Boxplot of the values of Mean (MI) and standard deviation (SDI) intensity measured in the analysed MS-VOIs

Discussion

The proposed algorithm works on both projection and image domain and allows the automatic detection of the corrupted portion of the image, thus preserving image detail where the artifacts are not present.

The described method allows to automatically segment hard tissues and metal objects, finding them in the projection data and replace them taking into account slice cross-talk. In particular, this algorithm was applied on CBCT images of the maxillofacial region.

The proposed method starts with the segmentation of hard tissue, corrupted sub-volume identification and metal object segmentation. Using a clustering approach all these steps were performed automatically and without the need of a priori information, such as preset thresholds or prior knowledge about metal object geometry and composition [107–109]. Moreover, this adaptive segmentation approach allows to overcome a well-know limitation of CBCT images, such as the variability of grey values, allowing its use on different CBCT devices [43, 110].

As can be seen in Figure 3.16 the proposed MAR approach allows to both reduce dark bands and streaks artifacts. From these results, qualitative improvement of image quality can be noticed, even in presence of strong artifacts. In particular, the corrected images are free of radiating pattern and shadows artifact between metal objects. In some cases,

the algorithm is not able to fully delete metal artifact and in few cases new artifacts are introduces, which is a problem common to most of the published methods [111]. Results show a significant reduction of SD of intensity values of non metallic voxels in all the analyzed regions of interest.

As known, the interpolation method can reduce SD values due to the low-pass effect of sequential forward and backward projections [111]. In this work, this effect was reduced working directly in the image domain, restoring the image details lost due to the smoothing effect. In this way, a well-know side effect of the projection interpolation approach was reduced in a fast and computationally inexpensive way.

Conclusion

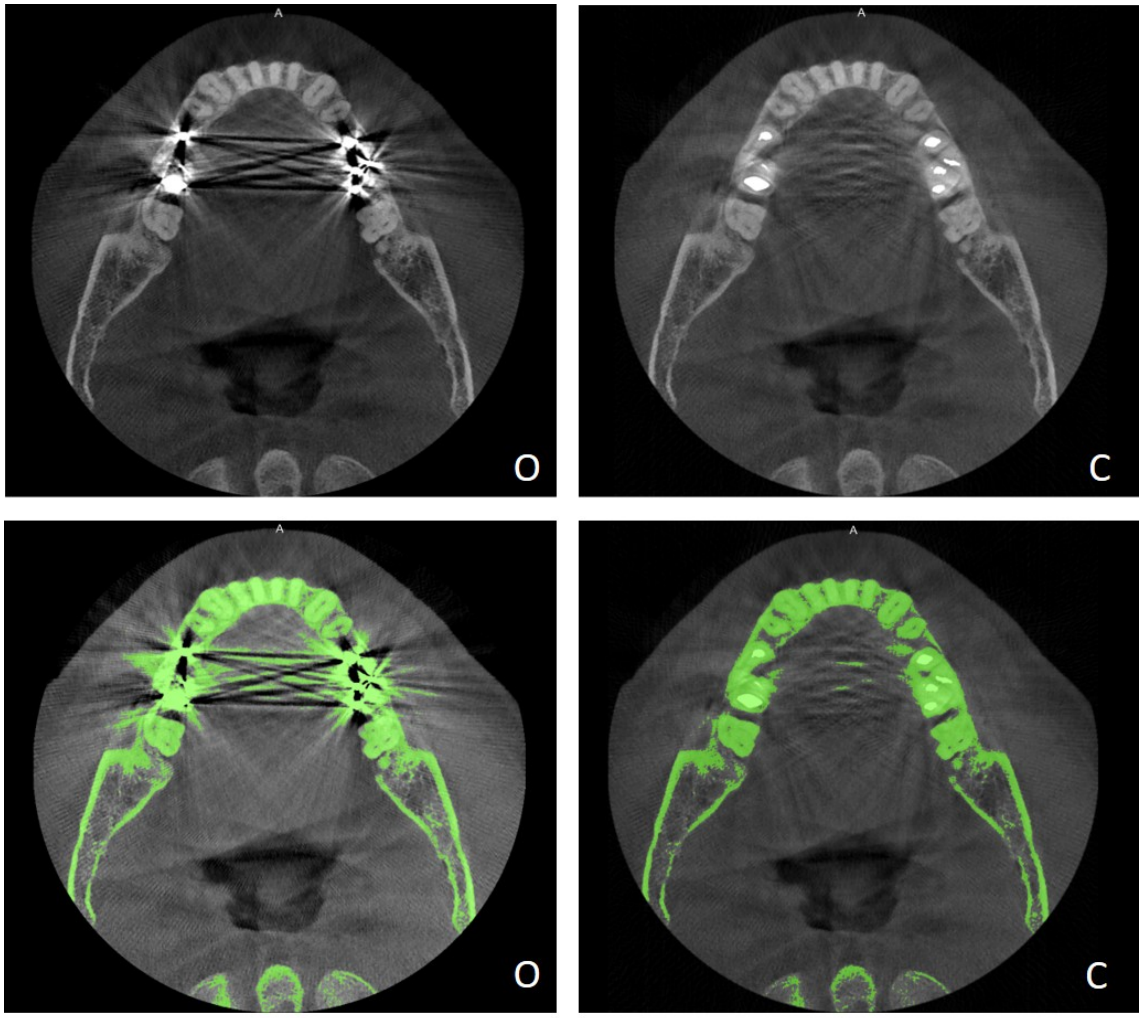

Figure 3.18: example of image before and after the application of the proposed MAR algorithm and the outcomes of image segmentation applying the same threshold value

In our dataset, the proposed MAR algorithm always decreased the voxel intensity

SD in the examined surrounds of metal objects, thus showing a significant metal artifact reduction in a fully automatic way. Moreover, the reduction of metal artifacts allowed to improve segmentation outcomes. Figure 3.18 shows an example of image before and after the application of the proposed MAR algorithm and the outcomes of image segmentation applying the same threshold value. As can be seen, some anatomical structures partially lost due to the presence of artifacts were recovered, improving the quality of the segmented hard tissue. Improvements in segmentation allow to obtain more accurate 3D models, making them more suitable for CAD/CAM applications.

Obtained results are promising, the algorithm seems able to reduce metal artifacts without a priori information about image setting parameter and metal object geometry. Nevertheless, further validation using equivalent tissue phantoms must be performed.

3.4 Automatic segmentation for condylar morphometric analysis in CT and CBCT data: an in-vitro validation.

The aim of orthognathic surgery is treatment of maxillofacial deformities to improve oral function as well as facial aesthetics with a long-term perspective. The surgery itself involves significant bone remodelling. The latter surely applies to the mandibular condyles. Condylar remodelling may remain within physiological condition or result in progressive condylar resorption [112]. Diagnosis of this condition is mainly based on 3D radiological examination (MSCT or CBCT). These 3D scans enable analysis of morphological and volumetric changes during healing [49]. Since such analyses strictly depend on the accuracy of bone segmentation, it is important to have an accurate and repeatable segmentation method. For this reason, in this study we propose an automatic method to segment condyle structure in both MSCT and CBCT data.

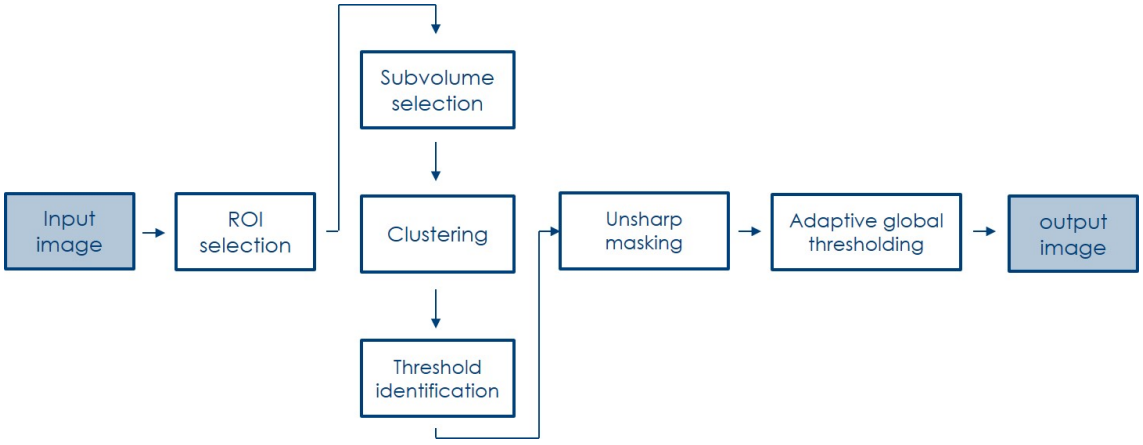

Figure 3.19: Flowchart of the mandibular condyle segmentation process

Materials and Methods:

The proposed algorithm, entirely developed in MATLAB (MathWorks, Natick, MA, USA), automatically segments the mandibular condyle in both MSCT and CBCT images. The flowchart of the proposed algorithm is presented in Figure 3.20. The presented segmentation method combines patient adaptive thresholding and contrast enhancement techniques in order to improve the segmentation of both trabecular and cortical bone. Thresholding was done by 4 clusters (air, soft tissue, trabecular and cortical bone) k-means clustering performed on one of each two slices of the original volume. For each slice the minimum intensity value classified as cortical bone was collected. Thereafter, the global threshold was defined as the 10th percentile of the population of minimum values. Then the same

method was applied to the trabecular bone cluster. Secondly, to create the first segmentation mask, the image contrast was enhanced using unsharp masking technique and segmented using the cortical threshold value. The unsharp masking id an image sharpening techniques that subtract a blurred (unsharp) version of the image from itself. In this study, this technique is used to locally increase image contrast, thus improving the subsequent adaptive thresholding step.

Then, the trabecular bone threshold was applied to the voxels of the first mask obtaining the second segmentation mask.

Once this mask was obtained, it was refined removing all the residual volumes of the segmentation process caused by noise or artifacts. Finally, it was applied to the original volume, maintaining the detail of the trabecular bone.

Figure 3.21 shows a detailed flowchart of these image processing steps, applied to an axial slice of a CBCT image.

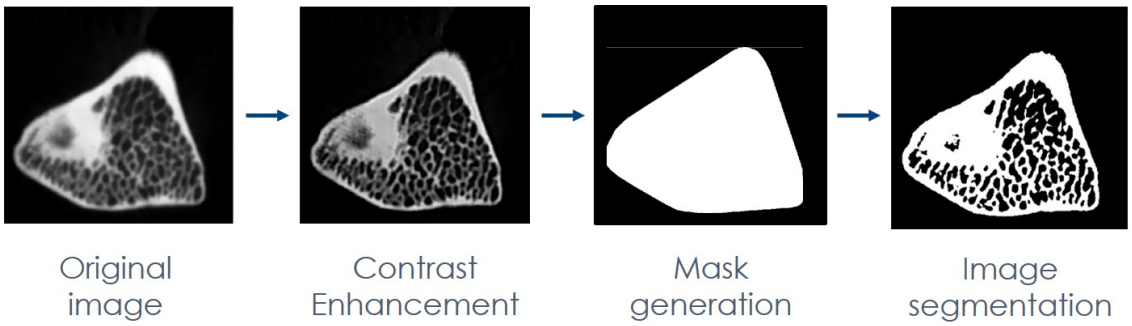

Figure 3.20: Example of image processing steps applied to an axial image of the dry condyle used in this study

For validation, a dry human hemimandible was scanned with 4 CBCT and 1 MSCT machine using clinical scanning protocols for condylar examination. To reproduce soft-tissue attenuation, a copper filter was used during all acquisitions. Moreover, the condyle was cut and scanned using a microCT, which represents the gold standard for bone x-ray imaging.

After image registration, all images were segmented with the proposed method and manual global thresholding. The segmented volumes, Dice similarity coefficient, which is a spatial overlap index. Dice coefficient can range from 0, indicating no spatial overlap between two sets of binary segmentation results, to 1, indicating complete overlap [113]. Moreover, the percentages of bone overestimation were calculated. Signed-rank sum test was used for data comparisons, with the significance level set to $p<0.05$.

Results:

The algorithm was tested on 6 image volumes. Qualitative comparison between the proposed algorithm and the global thresholding showed improvement of the segmentation accuracy, as it can be seen in Figure 3.22. The median (IQR) segmented volume was 1515.1 mm^3 (166.8 mm^3) for the automatic segmentation method and 1949.9 mm^3 (79.9 mm^3) for the manual thresholding.

Significant differences were found between segmented volume values ($p < 0.05$), Figure 3.21 shows the values of volume difference in all the used images.

The median (IQR) Dice Similarity Coefficient was 0.87 (0.1), with the maximum value of 0.98 for the MicroCT image volumes. Regarding the percentages of overestimation of the segmented volume compared with the MicroCT image, the median (IQR) value was 13% (10%) for the proposed method and 7% (4%) for the manual thresholding ($p < 0.05$).

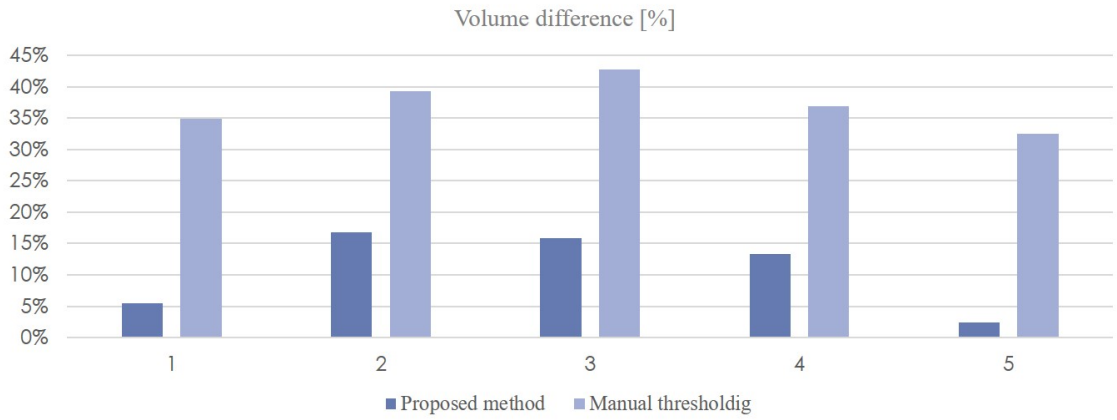

Figure 3.21: Volume difference between the microCT scan of the condyle (gold standard) and each CT and CBCT acquisition, segmented with the proposed method and manual thresholding

Conclusion:

The proposed method represents a fully automatic alternative for condyle segmentation in both CT and CBCT data. In particular, the automatic segmentation allows to improve the quality of the trabecular bone segmentation and significantly reduce the overestimation of the segmented bone (with a median reduction of 24% between methods), especially for high resolution images, as can be seen in Figure 3.22. Results are promising, nevertheless a further validation on an enlarged sample is advised.

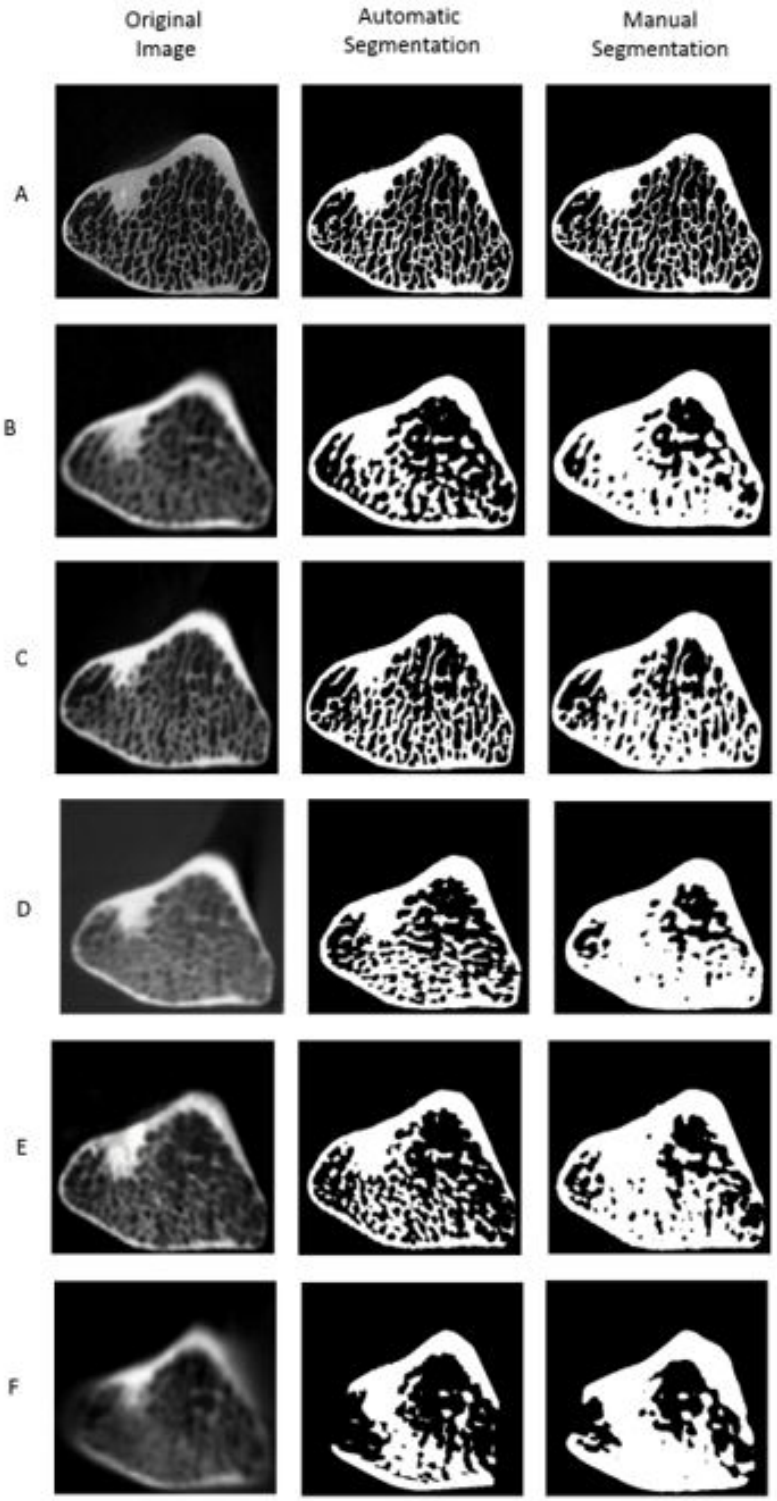

Figure 3.22: Outcomes of mandibular condyle segmentation, applied on an axial slice, obtained with manual and automatic segmentation

Chapter 4

Facial Soft Tissue Imaging

This chapter is based on:

- M. Codari et al. "Stereophotogrammetry and laser scans: non-invasive follow up technique for orthodontic patients", *The British Journal of Oral & Maxillofacial Surgery*, 53(8):769-770, 2015
- M. Codari et al. "Facial thirds-based method for facial asymmetry evaluation", *Journal of Craniomaxillofacial Surgery*, *In press*

4.1 Facial soft tissue imaging

Facial soft tissue can be imaged using different image modalities. MRI and US imaging can be used to evaluate the inner craniofacial soft tissue, while external facial surfaces can be imaged with optical systems. Among optical systems, stereophotogrammetry can be a useful tool to evaluate facial morphology, since it allows to reconstruct the digital surface of patient face in a safe, un-invasive and fast way [2].

These systems allow to create a 3D image from a series of multiple photographs taken simultaneously from different points of view. These images allow to reconstruct a 3D mesh composed by a point cloud connected in order to form triangular faces. Figure 4.1 shows an example of obtained 3D representation of facial soft tissues.

Figure 4.1: Three-dimensional surface rendering, and the corresponding triangular mesh, of facial soft tissues obtained using a stereophotogrammetric system

Stereophotogrammetric systems were found accurate and reliable for the detection of facial landmarks and for the evaluation of facial distances and angles [114, 115]. Moreover, they allow to acquire patient face in a contact-free way and without the use of ionizing radiations, making it suitable for frequent follow up evaluations. Another advantage of stereophotogrammetric systems is the short acquisition time, that makes it usable for the analysis of non-collaborative patients, such as children and special needs subjects.

Patients with craniofacial dismorphology are usually characterized by complex irregularities in the shape and configuration of facial soft tissue structures [116]. Moreover they often undergo extensive surgical procedures, so the development of fast and un-invasive follow up techniques is of particular importance for them.

Laser scanners are another class of instruments that allows to obtain three-dimensional

surfaces. They consist in a light source that projects well defined lines on the scanned object, which are then acquired from a series of cameras in order to reconstruct a 3D triangle based surface. The main limitation of this acquisition system is the time necessary for a complete facial scan, which is significantly higher than that necessary for stereophotogrammetry [2]. For this reason, their main application is for the reconstruction of 3D surfaces of dental cast for CAD/CAM applications.

Together with the advancement in scanning technology, the development of new follow-up protocols for the quantitative evaluation of patient morphology is important. Recently, several study were published on the application on stereophotogrammetric system for the evaluation of maxillofacial surgery outcomes [117–119].

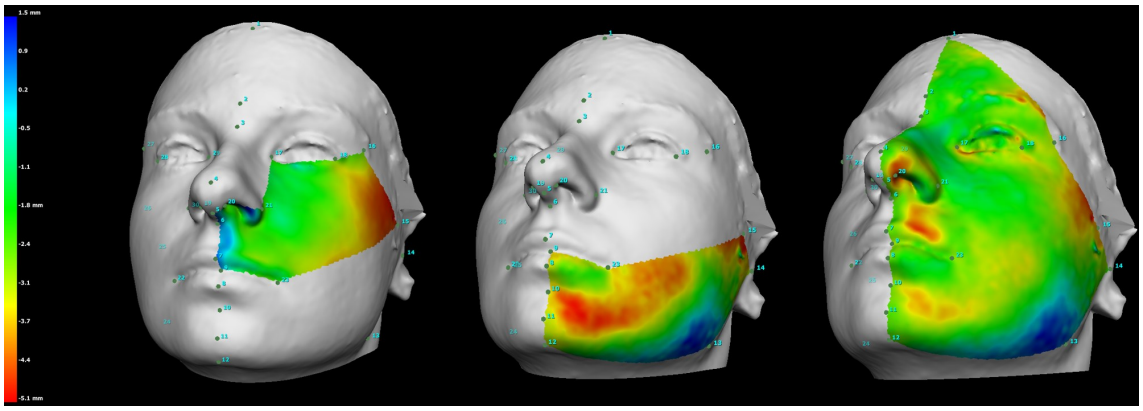

Figure 4.2: Example of surface analysis performed on stereophotogrammetric images

The instruments offer an innovative approach where surface and volumetric analysis during treatment planning allow the users to easily evaluate facial morphology without the need of direct measurement on patient face, thus reducing patient discomfort. Figure 4.2 shows an example of surface analysis performed on stereophotogrammetric images.

Moreover, using image fusion techniques, the stereophotogrammetric surface of patient face can be integrated with bony structure models obtained from MSCT and CBCT data, or with digital dental cast models obtained using laser scanners. In this way, it is easy to evaluate patient's condition, and then plan and simulate possible treatment and surgery options, monitor actual images of progress and make evaluations of outcomes [120].

Stereophotogrammetry, together with other imaging modalities, can be a powerful tool for the development of virtual patient models. In this section, two different follow up approaches for the evaluation of soft tissue morphology, based on stereophotogrammetric facial surfaces, are presented.

4.2 Facial thirds-based method for facial asymmetry evaluation

Many pathologies can result in facial asymmetry. Among those, hemifacial microsomia, cleft lip/palate, mandibular osteochondroma, trauma and infections, untreated mandibular fractures and damage to facial nerves are mentionable. In particular, facial nerve palsy, which can be due to different etiologies, from neoplasm to infective, traumatic, congenital and metabolic causes, can strongly alter facial harmony [121]. Furthermore, environmental factors, as chewing and sucking habits, or craniofacial syndromes, can compromise facial symmetry [122, 123]. The amount of asymmetry of the face can vary among subjects, ranging from unperceived or subclinical cases to evident and clear ones. In those cases, aesthetics, appearance and functionality of the orofacial complex can be severely affected, leading to discomfort and dissatisfaction of the patients for their own facial appearance [124, 125]. To both improve aesthetics and correct functional defects, an objective, quantitative assessment of facial asymmetry is advised. The quantification of asymmetry can be especially useful during surgical treatment planning, but it can also be performed during follow up examinations, allowing surgeons and dentists to evaluate the progressive reduction of asymmetry, therapy progression and achieved results [126–128].

The evaluation of facial morphology evolved during the last decades, passing from the direct measurement to an indirect assessment of the face, through two- and three-dimensional imaging systems [129]. These technologies can allow not only a facial analysis based on landmarks, but also the investigation of the whole surface [130]. Surface assessments have already been found to be more sensitive than landmark measurements [128]. Currently, facial asymmetry is mainly evaluated using the entire facial surface, thus providing measurements that give only general information about facial morphology [128, 131]. In contrast, several pathologies affecting facial appearance are localized in selected parts of the face [123, 132], and a local assessment can provide helpful information for clinical decisions.

In this study, we introduce a new method that combines surface and landmarks based approaches to assess facial asymmetry, taking different facial thirds into account, in order to provide local information. The intra-operator repeatability of the method was assessed, and a practical application in patients with unilateral facial palsy was made.

Materials and methods

Sample: Seventy adult Caucasian subjects were voluntarily recruited for this study. This sample was composed of 40 healthy subjects (21 females; 19 males; average age 39 ± 12 years) and 30 patients with diagnosed unilateral facial palsy (15 females; 15 males; average age 44 ± 15 years). All healthy subjects had no history of facial trauma, maxillofacial surgery and craniofacial syndromes or deformities. Among the patients, the etiology of the facial nerve palsy was: oncological surgery (71%), Bell's palsy (18%), trauma (7%) and brainstem embolus due to arterio-venous malformations (4%).

Image acquisition: All the involved subjects were acquired using the VECTRA M3 stereophotogrammetric system (Canfield Scientific Inc., Fairfield, NJ), which allows to scan their faces in a fast and non-invasive way [2]. Before the acquisition, 50 soft tissue facial landmarks were marked using black liquid eyeliner; following a protocol that was previously developed, tested and validated by our research group [114, 133]. During the acquisition, subjects were asked to have a neutral facial expression of the face, with teeth in loose contact and closed mouth. The institutional review board of the University of Milan (approval n. 92/2014) approved all the described procedures and all patients gave their written informed consent to them.
After the acquisition process, the facial landmarks were digitally marked on each surface, to delimit the portions of the face used for asymmetry evaluation, using the manufacturer's software (Mirror Vectra; Canfield Scientific Inc., Fairfield, NJ).

Asymmetry quantification: In order to define the portion of face used to evaluate the asymmetry of the subject, 10 facial landmarks were selected. A detailed list of these landmarks is provided in Table 1. Landmark selection allows to delimit the facial surface in a standard and repeatable way, thus reducing operator dependency. An example of the selected surface is depicted in Figure 4.3. Intra-operator repeatability of FA selection was evaluated on a training sample of 20 facial surfaces. One experienced operator selected the different facial thirds and the FA twice with a two week interval. The repeatability was assessed on facial surface selection since it is the main cause of variability in surface mirroring approaches, as further image processing steps are automated. After landmark identification, the Mirror Vectra software (Canfield Scientific Inc., Fairfield, NJ) automatically computed the surface area.
The selected surface was then used to calculate the plane of maximum symmetry, this process allowed to automatically find the midline plane of symmetry using only a previously

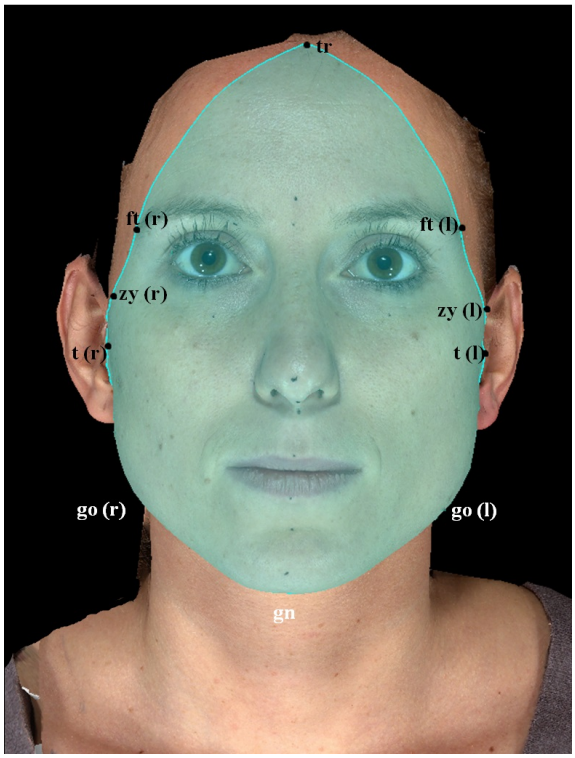

Figure 4.3: Facial area (FA) selected to evaluate asymmetry, based on the more external anthropometric landmarks of the face. Landmarks that are not visible from the frontal view are shown in white; r and l indicate right and left side of the face, respectively

selected area on the acquired facial surface. In this study, the selected area was defined in order to minimize the regions that can affect asymmetry quantification, such as hairs and neck region, and to take all the craniofacial structures of interest for maxillofacial morphometric analysis into account. This processing step was carried out using the Mirror imaging software (Canfield Scientific Inc., Fairfield, NJ).

Once the plane of maximum symmetry was obtained, it was used as mirroring plane to obtain the reflected face of each subject.

The original facial surface was then divided in two hemi-face surfaces, that were subsequently subdivided into three different facial thirds: upper, middle and lower third. In the proposed method, facial thirds division was based on the territories of distribution of trigeminal branches, which correspond to different embryological origins (Holmes, 2016). Each third was defined using anatomical landmarks, thus providing a standard and repeatable selection criterion. The list of landmarks used to define each facial third is provided in Table 4.1 while an example of facial third selection is depicted in Figure 4.4.

Finally, to quantify the asymmetry of each facial third in each subject, the RMSD between original and reflected surfaces was calculated. A color-coded surface map displayed

Table 4.1: Landmarks used to define facial area and the different facial thirds

Selected Area	Landmarks
Facial area (FA)	trichion (tr); frontotemporale (ft); zygion (zy); tragion (t); gonion (go); gnation (gn)
Upper third (UT)	trichion (tr); glabella (g); nasion (n); pronasale (prn); columella (c); alare (al); endocantion (en); exocantion (ex); frontotemporale (ft)
Middle third (MT)	endocantion (en); alare (al); upper terminal of the nostril (stn); columella (c); subnasale (sn); labiale superius (ls); stomion (sto); chelion (ch); zygion (zy); frontotemporale (ft); exocantion (ex)
Lower third (LT)	Stomion (sto), labiale inferius (li); sublabiale (sl); pogonion (pg); gnation (gn); gonion (go); tragion (t); zygion (zy); cheilion (ch)

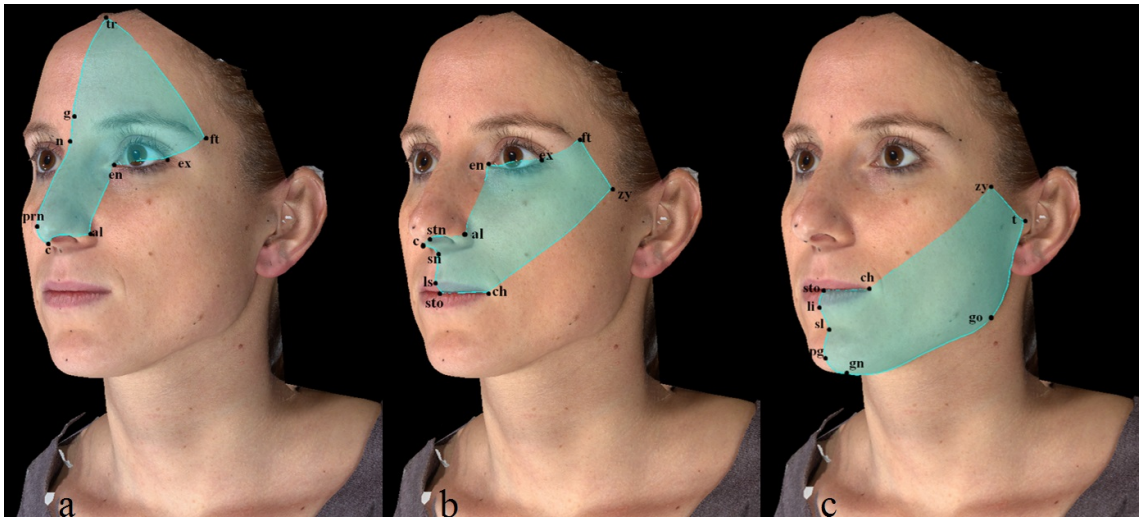

Figure 4.4: (a) Upper facial third (UT); (b) Middle facial third (MT); (c) Lower facial third (LT); each one defined by the respective anatomical landmarks, chosen to follow the territories of distribution of trigeminal branches

the local values of the distances between the two surfaces, as it can be seen in Figure 4.5. The RMSD has already proved to be a reproducible and accurate way to measure facial asymmetry, using three-dimensional photogrammetric systems [134].

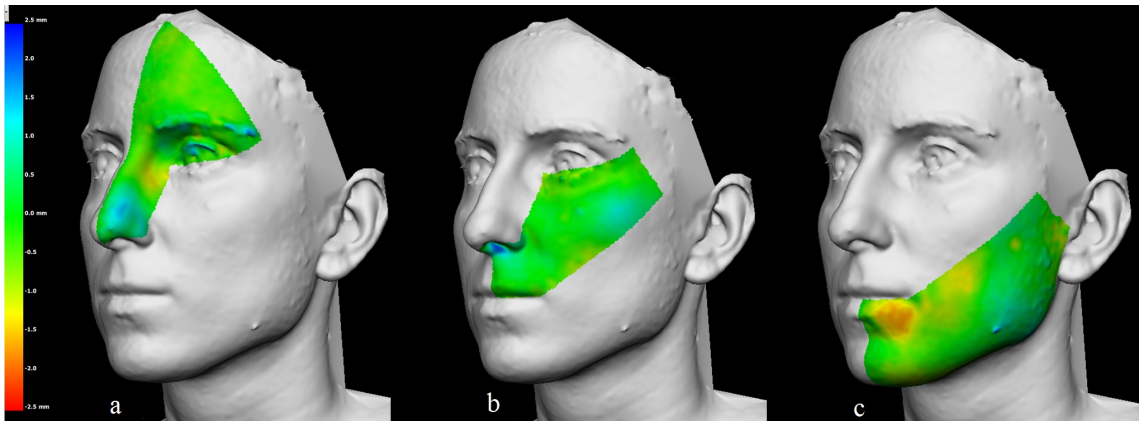

Figure 4.5: Color coded maps for the local distances between the original and mirrored facial areas. (a) Upper third; (b) Middle third; (c) Lower third

Statistical Analysis: Chi square test was used to check differences in sex distribution between control and patient groups, while unpaired Student's t-test was used to check age difference.

The repeatability in surface area selection was tested using Bland and Altman analysis for both the total facial area and each facial third. For repeated area measurements, the bias value, that corresponds to the systematic error, and the RC, that represents the least detectable difference among measurements and it is twice the standard deviation of measurement differences [135], were calculated.

Boxplots were used for representing RMSD values of different facial thirds in different subject groups. Normality distribution of the data was tested using the Kolmogorov-Smirnov-test. RMSD of different facial thirds in both control and pathological subject were positively skewed; so logarithmic transformation of the data was performed in order to obtain normal distributions. After this transformation, a two-way ANOVA analysis was performed in order to check if there were statistical significant differences among groups and facial thirds. Post hoc analyses were performed using Fisher's LSD test. The statistical level of significance was set to $p<0.05$ for all tests.

Results

In this study, 40 control subjects and 30 patients with diagnosed unilateral facial palsy were analyzed. No statistically significant differences were found in age ($p = 0.1$, Student's t) and sex distribution ($p = 0.84$, chi-square).

The statistical analysis of the repeated area measurements showed high level of reproducibility. Bland and Altman plots and the values of bias, SD, RC and reproducibility are respectively reported in Figure 4.6 and Table 4.2.

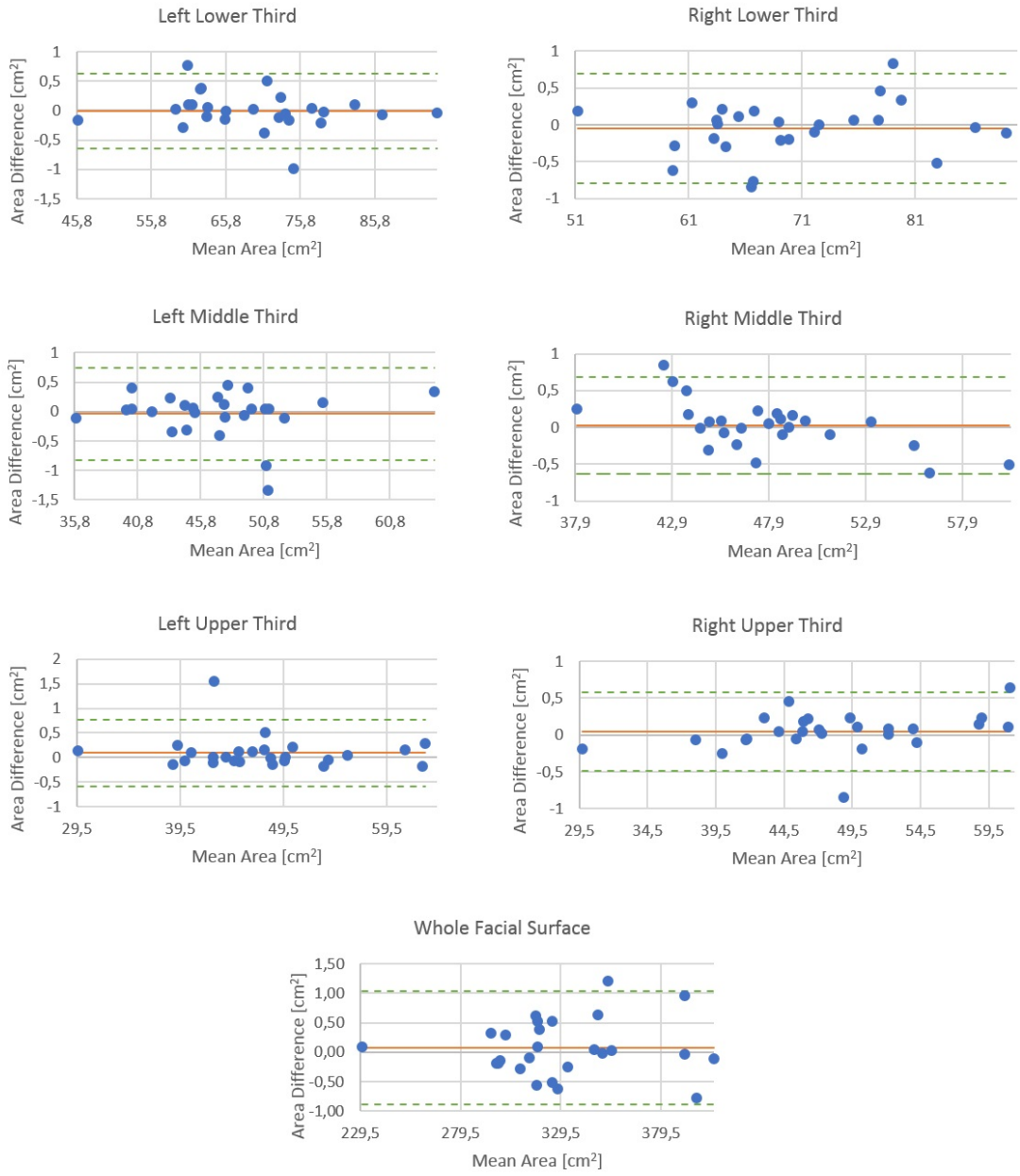

Figure 4.6: Bland and Altman plots for the area repeated measurements. Continuous line indicates the average; dashed lines indicate the interval of agreement

Table 4.2: Results of Bland and Altman analysis. Bias, SD and RC of area measurements are reported for upper (UT), middle (MT) and lower (LT) thirds and the whole facial area (FA).

	UT		MT		LT		FA
	Left	Right	Left	Right	Left	Right	
Bias $[cm^2]$	-0.003	-0.051	-0.039	-0.028	0.097	0.043	0.075
SD $[cm^2]$	0.319	0.372	0.393	0.329	0.340	0.267	0.479
RC [%]	0.9	1.1	1.7	1.4	1.4	1.1	0.6

Values of RMSD in control subjects and patients, divided for each facial third, are presented in Figure 4.7. Overall, patients had a larger asymmetry in all facial thirds than control subjects; the difference appears particularly evident for the middle and lower thirds. Two-way ANOVA showed a statistically significant difference in RMSD values be-

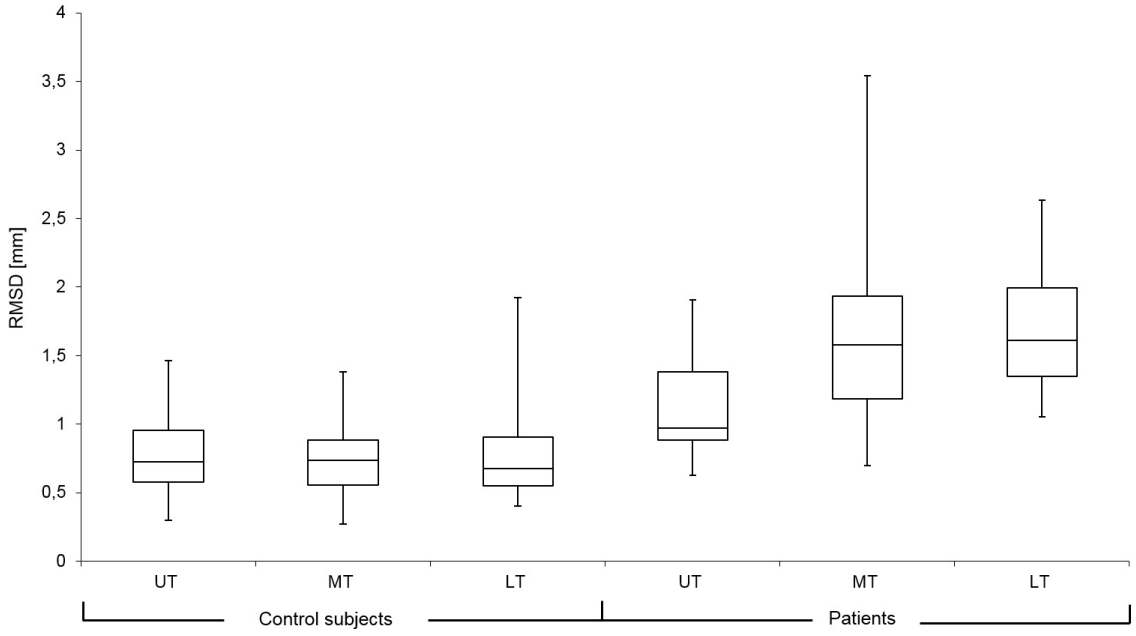

Figure 4.7: Box plots, representing Root Mean Square (RMS) values of controls subjects and patients for upper, middle and lower facial third

tween control subjects and patients ($p = 0.000$). A significant effect of facial third was also found ($p = 0.0014$), together with a significant group x third interaction ($p = 0.0012$). Among different thirds, the RMSD values of the UT resulted significantly different from the ones of the MT ($p = 0.005$) and LT ($p = 0.003$). Post hoc analysis showed that among control subject there was no significant difference between different thirds ($p > 0.05$). On

the other hand, in patients there was a significant difference between UT and MT ($p = 0.001$) and between UT and LT ($p = 0.000$). Comparing the same third between control and patient groups, statistically significant differences were found in all occasions ($p = 0.000$).

Discussion

The evaluation and quantification of facial asymmetry is a key task in maxillofacial surgery and orthodontics, since a lot of conditions can alter it, thus compromising the patient quality of life from functional, aesthetic and social points of view [136].

The introduction of noninvasive and inexpensive imaging procedures, e.g. laser scan and stereophotogrammetry, speeded up the research in this field and, in the last years, a lot of works were published on this topic, suggesting different approaches to assess facial asymmetry [128, 137–139]. Unfortunately, none of them is universally accepted from the scientific community, thus demonstrating that is still necessary to improve these procedures [132].

In the proposed method, we analyzed symmetry comparing original and mirrored facial surfaces and calculating the RMSD of the distances between their corresponding points. This approach is well known in the literature and it has proved to be a potentially powerful method to analyze facial symmetry [131, 132, 134].

Traditionally, the whole face is used to measure the asymmetry level of the subject, thus providing only a global evaluation of facial morphology [128,139]. In this study, we divided each hemi-face in thirds, based on trigeminal branches distribution territories for somatic sensitivity. Other studies tried to provide a local subdivision of the face using horizontal planes, thus obtaining irregular edges of selected thirds due to subjective selection of the facial area [132, 134, 140].

In the proposed method, facial area selection is the only manual image processing step needed to quantify the asymmetry of the face using surface mirroring approaches. To obtain a standardized imaging method it is essential to reduce the variability among different measurements as low as possible. For this reason, the selection of the FA plays a key role in asymmetry assessment on 3D facial surfaces. In the proposed method, the standardized definition of thirds allowed to reach a very high level of reproducibility during area selection, which is the main source of variability in asymmetry quantification. Repeatability analysis shows an average RC value ($\pm$ SD) equal to $1.2\% \pm 0.005\%$, proving a high level of agreement between repeated measurements. As shown by the Bland and Altman plot in

Figure 4, the bias is always near to 0% (average bias value 0.03% ± 0.001%), thus demonstrating the absence of systematic errors during repeated measurements. Moreover, the division of the face in thirds allows to focus treatment planning and follow up evaluations on the most asymmetric region.

To validate the proposed method, both patients with diagnosed unilateral facial palsy and control subjects, matched for gender and age, were enrolled. Unilateral facial palsy causes an evident asymmetry of the facial soft tissues, so it can be considered a perfect condition for testing this method within a clinical context. Other investigations used artificial, mathematically originated facial asymmetries that can be difficulty translated into daily practice [128].

In all subjects, the asymmetry was quantified calculating the RMSD of corresponding points belonging to mirrored hemi-facial thirds. The results show that patients had a significantly less asymmetric UT compared to the middle and lower thirds. Indeed, the UT is mainly composed by the frontal region, which is the area less affected by facial palsy. On the other hand, despite the fact that this third is less asymmetric than the other two, it is still more asymmetrical in patients than in control subjects. That can also be explained by the fact that the upper eyelid/ superior orbital region, which is strongly altered in facial nerve palsy, is part of our UT. Among control subjects, there was no significant difference in RMSD values of different thirds, thus confirming the recent observations of Djordjevic et al. [132].

These results proved the accuracy of the proposed method in asymmetry quantification, both in physiological and pathological conditions, allowing clinicians to use it in different kind of pathologies. Moreover, the strong reproducibility of this method makes it suitable for follow up evaluations in different craniofacial conditions.

Conclusions

With this study a facial third-based method for the analysis of facial asymmetry is provided. The method showed high reproducibility and accuracy in evaluating differences between control subjects and patients. Moreover, it is applicable for diagnosis, treatment planning and evaluation in patients with altered craniofacial morphology. In particular, the method appears suitable for pathologies that alter only part of the face, providing quantitative local information about facial symmetry.

4.3 Stereophotogrammetry and laser scans: non-invasive follow up technique for orthodontic patients

Nowadays digital technologies are widely used in dentistry, moving dental practices to virtual-based processes [3]. For this reason, the use of three-dimensional (3D) images is becoming normal in both clinical and research contexts [2] .

Three-dimensional images of the face, skull and dentition of the patient can be acquired using different imaging technologies. Among these, only CT and MRI allow to include all the mentioned structures in a single image, but they can not be used routinely due to their invasiveness, accessibility or cost. On the other hand, stereophotogrammetry and laser scanner allow to acquire separately the face and the dentition of the subject in a noninvasive way, making them suitable for use in children and for longitudinal evaluation of treatment outcomes [141]. Given the great potential of these technologies for application in the oro-maxillo-facial field, the integration of these imaging modalities seems to be a logical solution that will allow clinician to create a 3D virtual model of the patient and to deeply understand the correlation between soft and hard tissues that compose the face [142, 143].

In this context, the current work aims to define and validate a technique that allows to integrate the information about the dentition of the patient with the stereophotogrammetric reconstruction of the face and providing an uninvasive way to assess the morphology of facial soft tissues in relation to teeth.

Materials and methods

In this work the digitized dental plaster casts and the facial stereophotogrammetric images of seven subjects just undergone CBCT were registered and analyzed. Moreover, CBCT images of the same subjects were analyzed in order to validate the proposed registration method.

All subjects undergone CBCT for clinical reasons not correlated with this study. All procedures related to this study were noninvasive; involved subject were previously informed about them and gave their written consent, according to the principles outlined in the Declaration of Helsinki.

As a continuation of the work proposed by Rosati et al. [144], for each subject both maxillary and mandibular dental cast was obtained and digitized using a commercial laser scanner (Dental Wings series 3, Dental Wings Inc., Montreal, Canada). The upper and

lower dental arches were separately digitized preserving the original teeth alignment and occlusion using the DWOS software (Dental Wings Inc., Montreal, Canada).

Moreover, facial soft tissues were acquired twice using a stereophotogrammetric system (Vectra 3D, Canfield Scientific, Fairfield, NJ), the first time with open lips and with cheek retractors (in order to make visible frontal teeth) and the second time with teeth in occlusion and closed lips [144].

As proposed by Rosati et al., the two surfaces representing the subject faces were registered using point based and subsequently a surface based registration technique [144].

As regarding the registration of the digitized dental cast, the current study proposes a new approach. The proposed algorithm, entirely developed in MATLAB (MathWorks, Natick, MA, USA) aims to register the maxillary and mandibular dental arches using a point base registration, subsequently refined with a surface based registration.

At first, to properly register the dental arches into subject's face, a region of interest (ROI) was selected on the open-lips stereophotogrammetric surface and on the laser scanner surface of the upper dental arches. These ROIs will contain the same the upper frontal teeth, as can be seen in Figure 4.8.

Once the ROIs were selected a point based rigid registration was perform to initialize the

Figure 4.8: Example of selected region of interest (ROI) from the stereophotogrammetric (above) and laser scanner surface (below). These ROIs were used for point and surface based registration

subsequent surface based registration.

During the first step the operator must select at least 3 point in each ROI in order to find the optimal rigid transformation that align the ROI selected on upper dental cast to the ROI selected on the stereophotogrammetric images. These points may be anatomi-

cal landmarks or point of interest easily detachable on both the surfaces and may vary from subject to subject, since the point based registration is only an initialization for the surface based registration. To calculate this optimal geometric transformation between corresponding points the Procrusters method was used, which determines a linear transformation of the fiducial points of the first image to best conform them to the fiducial points of the second image. The chosen cost function was the sum of squared errors that was minimized during the iterative registration process [94].
After this step the registration was refined using a surface base registration. To this purpose the Iterative Closest Point (ICP) algorithm was chosen to find the optimal geometric transformation that rigidly registers the structures contained in the ROIs.
The ICP algorithm reduces the general non-linear minimization problem to an iterative point-based registration problem. In order to address the issue of point correspondence, the ICP algorithm iteratively performs the following steps:

1. **Matching step:** For each point of the moving surface the nearest neighbour of the reference surface is calculated.

2. **Minimization step:** The error metric, that in this case was the mean square distance between corresponding points, is minimized

3. **Update step:** points are transformed using the geometric transformation resulting from the minimization step.

The process iterates until the mean square distance stabilized within s pre-set tolerance value [145, 146]. Once this geometric transformation is calculated, it was applied to the original upper and lower dental cast, providing their correct position relative to patient face. To evaluate ROIs registration the median distance and its interquartile range (IQR) between the point clouds of the ROIs was calculated. Figure 4.9 shows the distanced between corresponding points displayed using a colour scale on the surface of patient dental arch. Moreover, the percentage of corresponding points between the two ROIs was evaluated. Corresponding point were defined as points that showed a distance lower than 1 mm [20].
An example of the outcome of this registration process is depicted in Figure 4.10.
To validate the proposed algorithm five facial and six dental landmarks were placed on the CBCT image of each subject and on the registered facial and dental surfaces. Since CBCT represent simultaneously the hard and the soft tissue of the patient it is suitable for the validation of the proposed method.

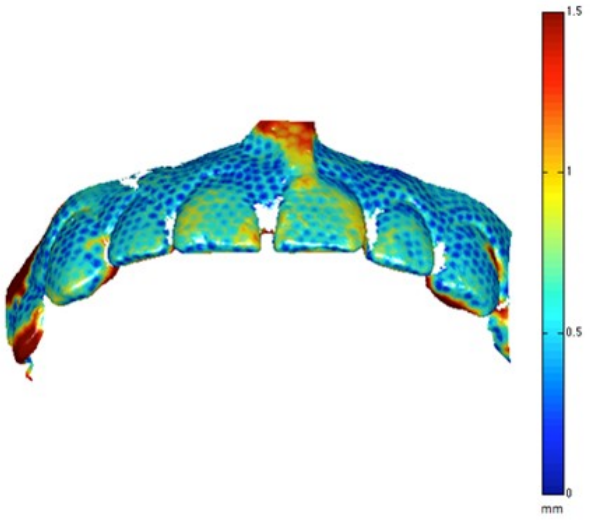

Figure 4.9: Example of assessment of distances between corresponding points between dental cast and stereophotogrammetric images

The chosen facial landmarks were: right and left Orbitale (lOr and rOr), Pronasale (Prn), Subnasale (Sn), Sublabiale (Sl), upper and lower inter-incisal (uIn and lIn) and the upper and lower distal vestibular cups of the first right and left molar (16, 46, 26 and 36). To evaluate the accuracy of the proposed method, the difference between distances were calculated. The Wilcoxon signed rank test was used to compare each distance taken on CBCT or stereophotogrammetric and laser scan surfaces. Significance level was set to $p<0.05$.

Results

For the evaluated subjects the median distances between ROI point clouds was 0.59 mm with an IQR of 0.43 - 0.73 mm. The median percentage of corresponding points was 86.1% with an IQR of 81.6% - 92.1%. In this work 28 dentofacial distances were evaluated. All distances, their descriptive statistics and p-value values are summarized in Table 4.3 and Table 4.4. No significant differences were found among all the evaluated distances except for the 36 - rOr distance ($p<0.05$).

Discussion

The proposed work aims to validate a method that allows clinicians to visualize the face and the dentition of patients using noninvasive imaging techniques. Compared with the method presented by Rosati et al., the proposed method allows to register separately both

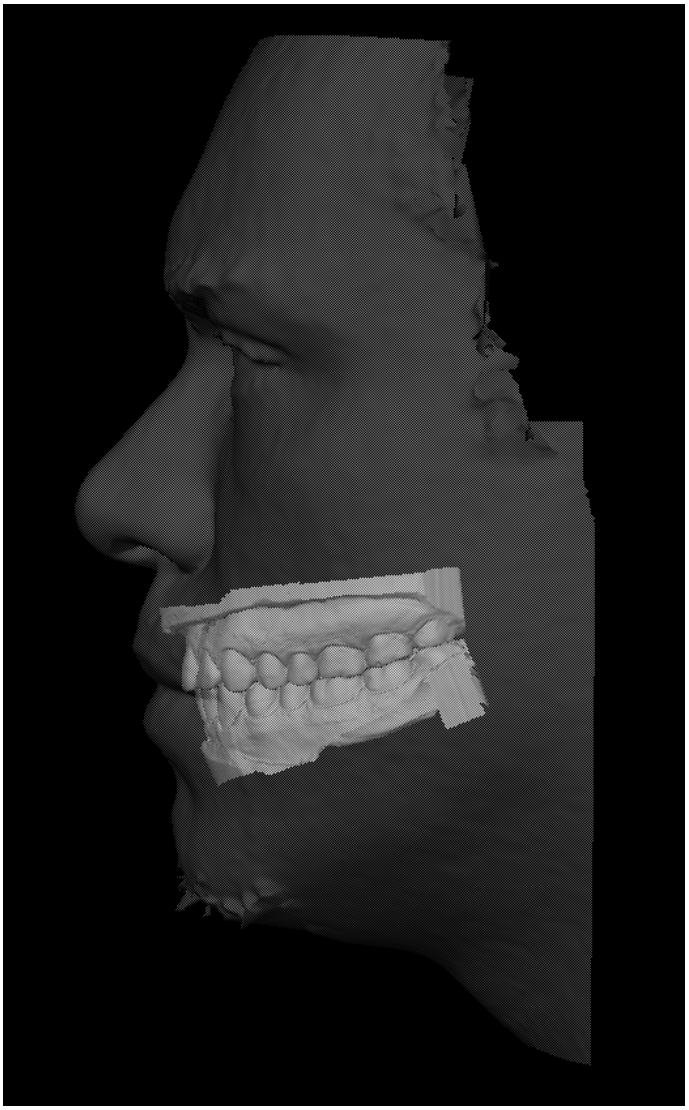

Figure 4.10: Example of registration outcome, between facial and dental surfaces. The darken surface represents the stereophotogrammetric acquisition of the face and the lighten surfaces represent the digitized dental casts

dental arches, providing a complete representation of patient dentition [144]. Moreover the dental arches were isolated from each other, allowing to analyze them together or separately.

To validate the proposed method CBCT images of the same subjects were retrospectively selected. CBCT images are used as reference image to evaluate the distances between face and teeth. In particular, the proposed work represents the first attempt at a complete validation of the registration algorithm on a subject sample [141, 147].

The high values of percentage of corresponding point and a median distance of 0.59 mm prove the accuracy of the registration progress. Statistical analysis shows no significant

Table 4.3: Median(IQR) distances between facial landmarks and landmarks belonging to the upper dental arch, expressed in mm

Distance	CBCT	Matched Surface	Wilcoxon p-value
uIn - lOr	66.3 (7.0)	64.8 (3.2)	0.43
uIn - rOr	67.4 (3.2)	64.3 (4.9)	0.06
uIn - Prn	46.3 (3.6)	45.9 (3.2)	0.84
uIn - Sn	27.3 (1.6)	27.1 (1.6)	1.00
16 - lOr	83.8 (7.2)	83.8 (3.0)	1.00
16 - rOr	53.2 (3.4)	54.2 (3.0)	0.56
16 - Prn	73.9 (5.6)	75.7 (2.5)	0.16
16 - Sn	55.7 (5.8)	57.4 (1,6)	0,31
16 - Sl	49.0 (3.0)	50.4 (2.5)	0.06
26 - lOr	52.4 (3.6)	54.2 (2.5)	0.16
26 - rOr	83.6 (6.2)	83.8 (1.8)	0.84
26 - Prn	73.7 (1,7)	74.9 (1.3)	0.09
26 - Sn	55.7 (2.6)	57.1 (4.6)	0.22
26 - Sl	48.8 (7.0)	49.3 (4.1)	0.69

differences between distanced calculated on CBCT image or on face and dental surfaces, except for one distance. This significance may be caused by the presence of the orbital landmark, which is difficult to annotate in CBCT images.

In conclusion, results show that this technique can be a useful tool to assess the position of facial soft tissues of the patient with respect to teeth. The results obtained are encouraging, nevertheless further validations on a larger sample are advisable.

Table 4.4: Median(IQR) distances between facial landmarks and landmarks belonging to the lower dental arch, expressed in mm

Distance	CBCT	Matched Surface	Wilcoxon p-value
lIn - lOr	64.3 (6.4)	63.1 (5.8)	0.56
lIn - rOr	65.5 (4.4)	62.3 (7.1)	0.07
lIn - Prn	46.8 (4.7)	46.9 (3.2)	0.84
lIn - Sn	27.2 (2.2)	27.4 (0.9)	1.00
46 - lOr	84.2 (5.4)	80.7 (1.7)	0.09
46 - rOr	55.7 (2.5)	53.4 (2.3)	0.09
46 - Prn	74.7 (4.6)	73,2 (3.3)	0.31
46 - Sn	56.1 (4.4)	54.7 (2.0)	0,31
46 - Sl	47.5 (1.2)	48.3 (3.8)	0.44
36 - lOr	54.9 (0.4)	50.6 (2.7)	0.16
36 - rOr	84.3(4.5)	79.4 (3.0)	0.03
36 - Prn	74.1 (2,0)	70.5 (1.2)	0.09
36 - Sn	55.8 (3.2)	52.8 (4.2)	0.16
36 - Sl	46.8 (3.2)	47.8 (4.9)	0.44

Chapter 5

Upper Airways Imaging

This chapter is based on:

- M. Codari et al. "The nasal septum deviation index (NSDI) based on CBCT data", *Dentomaxillofacial Radiology*, 45(2):20150327, 2015.

5.1 Upper airways imaging

The evaluation of craniofacial growth and in particular in airways morphology has increased in the last decades due to the interest in understanding the relationship between upper airway configuration and craniofacial morphology [148].

Traditionally, the upper airways and the near craniofacial structures were imaged using lateral cephalometric radiographies, which allow to perform linear and angular measurement to explore upper airway morphology [149]. However, cephalometry is affected by the limitation of two-dimensional radiographic procedure [150].

Usually, patient disease diagnosis requires the evaluation of the three-dimensional morphology of airways. For this reason, according to the medical literature airway evaluation can be performed using MRI, cine-MRI, MSCT, endoscopy and optical coherence tomography [148].

Recently, CBCT has emerged as cross-sectional, X-ray based, image modality for upper airways modelling thanks to its accessibility. Although CBCT has an inferior soft tissue contrast compared to MSCT, it is able to accurately define the boundaries between soft-tissue and air with high spatial resolution [149]. Furthermore, its accuracy and reliability for the assessment of upper airway was evaluated and confirmed in several studies [151, 152]. The main advantage of CBCT consists in the reduced radiation dose delivered to the patient without the reduction of its diagnostic usability, that make it suitable for otorhinolaryngological applications.

For all these reasons, recently different methods for upper airway segmentation and modelling were developed [14, 153, 154]. These algorithms allow clinicians to obtain three-dimensional models of the upper airways in an accurate and reliable way, which can be used for volumetric assessment, virtual rhinoscopy and computational fluid dynamics simulations.

Together with the advancement in software development, new imaging protocols for upper airway assessment were developed, which allow to fully understand their complex anatomy and help clinicians during treatment and surgical planning. In this way clinical evaluation can be helped by quantitative assessments of patient conditions, which may help in improve patient care.

In this section a new method for the quantification of nasal septal deviation and upper airway modelling in CBCT data is presented.

5.2 Airway modelling from CBCT data, application on nasal septum quantification

Nasal septal deviation consists in a misalignment of nasal septum from the midline, which leads to respiratory disease caused by volume reduction in nasal cavity. In approximately 90% of adults, nasal septum is not perfectly straight and median, but it often presents thickening and describes curves and angles [155]. NSD originates as a result of a disharmonious development of the facial skeleton that in some cases may occur after a trauma. A small anterior deviation can lead to a significant nasal obstruction, while a large deviation placed at the rear of nasal cavity may have no effect on the resistance of respiratory flow. Together with NSD, the compensatory hypertrophy of the turbinates, opposed to septal convexity, is often noticed [156, 157].

Diagnostic investigations currently used for this pathology are anterior rhinoscopy, endoscopy, multislice CT and MR, which allow a good evaluation of the entity and position of NSD [158–162]. In particular, pre-operative CT scan of the paranasal sinuses is often performed before septoplasty, in order to evaluate nasal anatomy, to find concomitant sinonasal pathologies and to reduce surgical failure [163, 164].

Despite the fact that pre-operative CT scan of the paranasal sinuses can be recommended in case of obstructive middle turbinate hypertrophy, impossibility to evaluate the middle meatus and the posterior nasal cavity or in patients with chronic sinusitis, the high radiation dose and costs do not allow its usage routinely in patients undergoing septoplasty.

In the last decades, CBCT is emerging and now it is widely used in dentistry thanks to its high resolution and low radiation dose. Currently its clinical use in other medical fields is limited and not widespread because of minor soft tissue contrast; however, many studies confirm that CBCT could be a valid support also in otorhinolaryngology [56, 165, 166].

Given that the evaluation of NSD is currently mainly based on subjective clinic and radiologic analysis, many studies are trying to find homogeneous and standard evaluation criteria based on morphometrical analysis of nasal airways [167, 168]. For example, recent studies evaluated the severity of NSD measuring the deviation angle, which is the angle included between a line drown from the apex of nasal septal deviation to crista galli and from crista galli to maxillary spine [157, 169].

Another method of evaluation is the segmentation of the upper airways, but the complex anatomy of the nasal cavity makes it hard to be segmented compared to other parts of the upper airways such as pharynx or larynx [168]. Three-dimensional segmentation has already been used in literature to study upper airways, mainly to assess Obstructive Sleep

Apnoea, but also in the evaluation of morphometrical changes occurred during growth or in case of congenital malformations [170–172]. In the current study we segmented several CBCT images to create three-dimensional models of the nasal airways, which were used to calculate three-dimensional parameters that describe their morphology. The aim of the proposed study was to understand if such parameters could be useful in NSD diagnosis and, secondary, if CBCT could be considered an adequate imaging technique for the proposed task.

Materials and Methods

For this study, 46 CBCT images were selected from the archives of SST Dentofacial Clinic (Segrate, MI, Italy), and analysed retrospectively. Subjects who had history of previous nasal surgery or other abnormality besides nasal septal deviation were excluded. All the images were evaluated by two experienced operators and divided in healthy and NSD subjects. An excellent level of agreement was found between operator, with an unweight Cohen κ equal to 0.86. Only in three cases the operators were in disagreement, so these data were excluded from the dataset. The final dataset was composed of 15 healthy subjects and 28 NSD subjects.

All CBCT scans were acquired by the same scanner (WhiteFox, ACTEON, MÃ©rignac, France). The device was operated at 6-10 mA (pulse mode) and 105 kV using a x-ray generator with fixed anode and 0.5 mm nominal focal spot size. The selected volume images are composed of isotropic 0.3 mm voxels.

To evaluate the severity of septal deviation, we assessed the difference between groups in SDA, calculated as proposed by Orhan et al. [173]. The measurements of the angle between the maxillary spine, the crista galli and the apex of the septal deviation were made using the freeware software OsiriX (Pixmeo, Geneva, Switzerland).

Subsequently, we evaluated the percentage difference between the volume of the upper airways in the right and left side of the nose in the same samples. Volume segmentation from the CBCT files was made using the freeware software ITK Snap, which allows the user to accurately segment and calculate volumes of upper airways [56,174]. For all images, a first automatic segmentation was subsequently refined manually.

At first, in order to obtain an accurate and reproducible segmentation of the nasal portion of the upper airway, a VOI was delimited for each side of the upper airways. Each VOI was defined as a box bounded antero-superiorly by the Rhinion, most inferior and anterior point between nasal bones, inferiorly from the lower limit of the hard palate, posteriorly from

the Posterior Nasal Spine landmark and laterally by the lateral margins of the nasal cavity, as shown in Figure 5.1. Once VOIs were selected, we proceeded with the segmentation of the nasal upper airway using the active contour segmentation option. Moreover, to avoid the inclusion of different portions of the maxillary sinuses in different subjects, they were segmented separately and their volume was subtracted from nasal airway volume. In Figure 5.2, an example of the outcome of the segmentation process is shown. The repeatability in the selection and segmentation of the volume of interest and in deviation angle measurements were verified on a subsample of 10 CBCT. Statistical analyses on measurement repeatability were performed calculating Student's t-test and Dahlberg's formula [175].

After the segmentation, the volume of each side of the nasal upper airway was measured, and then their relative VPD was calculated as:

$$VDP = \frac{|V_r - V_l|}{V_r + V_l} 100 \tag{5.1}$$

Where V_r and V_l, both expressed in cm^3, represent the volumes of the right and left VOIs defined previously.

Finally, a new index, named Septal Deviation Index (SDI), was introduced. The SDI was designed to summarize information about the angle of septal deviation, volume difference between right and left side of the nose and total volume of the nasal airway and was calculated as:

$$SDI = \frac{(SDA + 1)(VPD + 1)}{V_T} \tag{5.2}$$

Where SDA is the septal deviation angle, expressed in degrees, VPD is the adimensional volumetric percentage of difference and VT represents the total volume of nasal airways ($V_T = V_r + V_l$). Both SDA and VPD were increased by a unitary factor to prevent SDI from tending to zero if only one of these factors is null.

The statistical analysis was performed using the Matlab statistic toolbox (Mathworks, Natick, USA). Student's t-tests were performed to compare different morphometric parameters in healthy and NSD subjects. Statistical significance was set at $p<0.05$. Furthermore, since the evaluated morphometric variables are related to each other, we used PCA to transform all the morphological data into a set of uncorrelated variables called principal components [176]. According to Kaiser's rule, we retained the components whose eigenvalues were larger than one [177]. PCA was performed on the correlation matrix of the normalized dataset.

Pearson's correlation coefficients retained principal components and all calculated param-

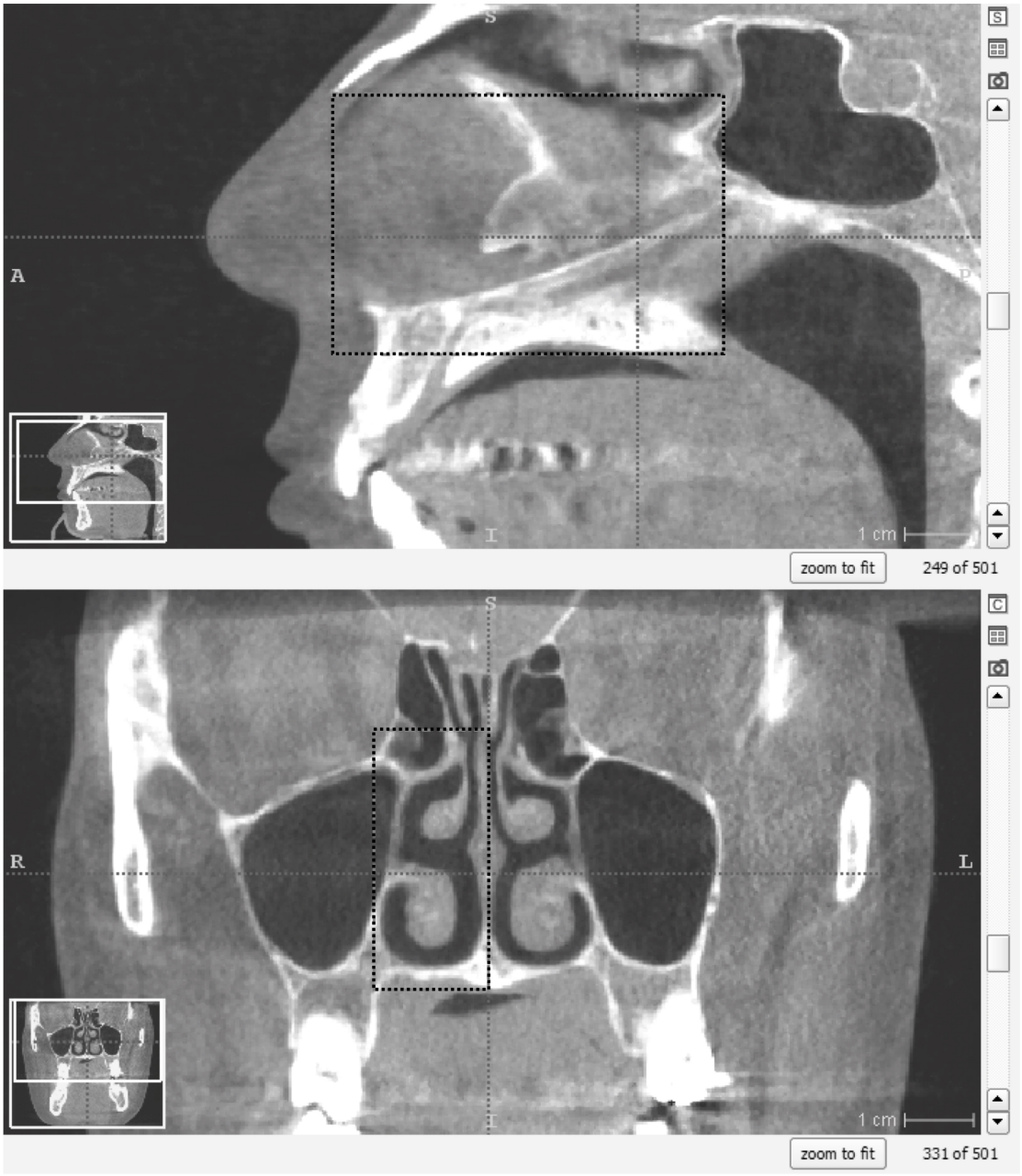

Figure 5.1: Example of segmentation of the right (B) and left (C) side of the nasal airway and of the left and right maxillary sinuses (A and D respectively). In the above image the segmentation outcomes are represented in a posterior coronal CBCT slice. In the image below, an example of the three-dimensional volumes segmented in the proposed study is depicted.

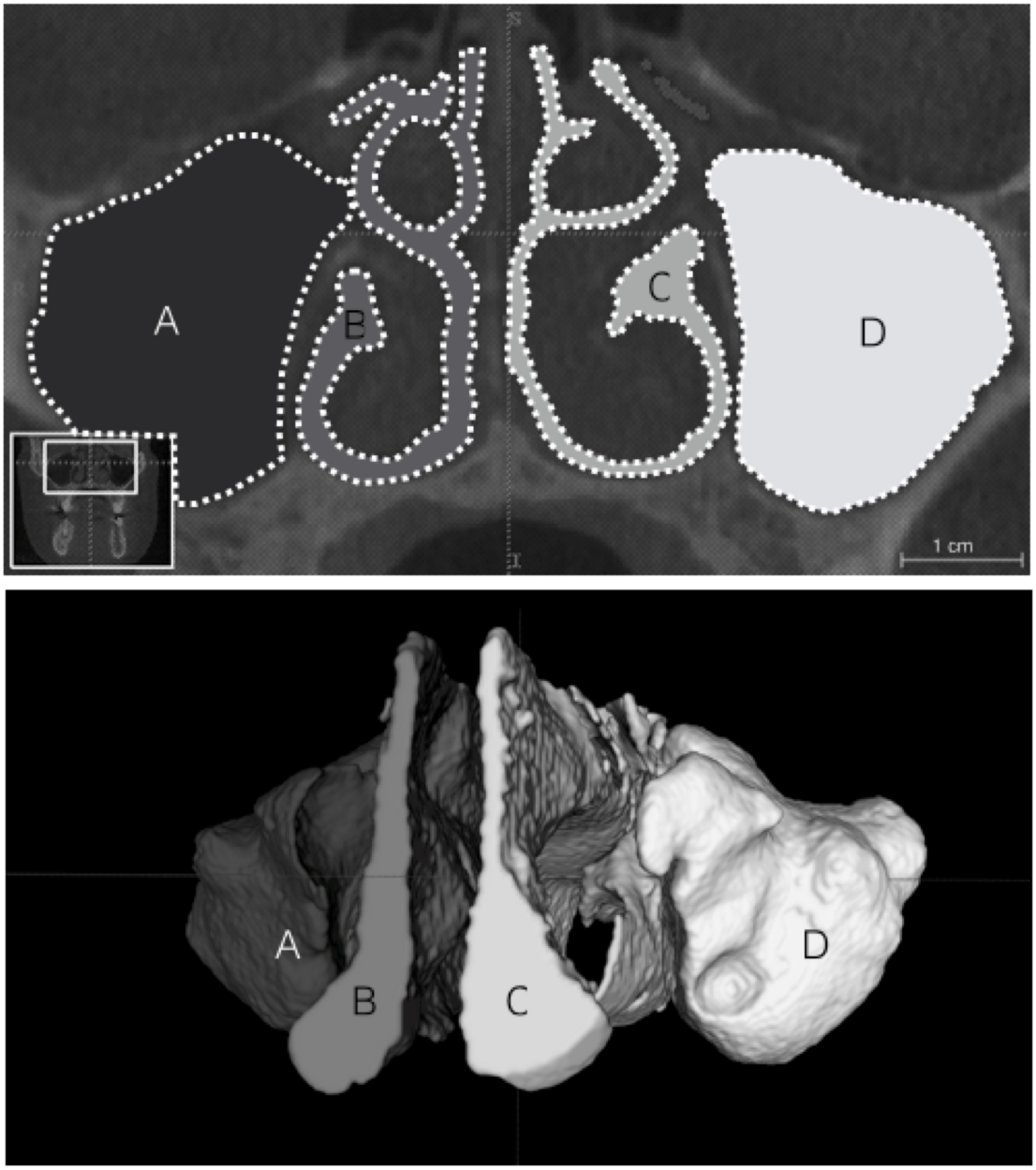

Figure 5.2: Example of a selected VOI for the right side of the nasal airways using ITK Snap. The bounding box is highlightened using dashed rectangles in sagittal (top) and frontal (bottom) views.

eters were also computed. In this way PCA is used to unveil the relationship between each variable and the global nasal airway variability [178].

Results

The analysed groups were composed of 15 healthy subjects (7 men, 9 women, average age 46 ±15 years) and 28 NSD subjects (15 men, 13 women, average age 48±15 years). No significant difference was found in age and sex between groups (p>0.05).
Repeatability analysis shown no significant differences both for SDA and volume measurements (p>0.05). In particular, random errors explained 0.77% of sample variance for angle measurements and 0.99% for volume measurements.
Values of SDA, VDP and SDI were significantly higher in NSD subjects compared to healthy subjects. Descriptive statistics of these parameters are summarized in Table 5.1. In

Table 5.1: Septal deviation angle (SDA), percentage of volume difference (PVD), total volume (V_T) and septal deviation index (SDI) between healthy and NSD group.

	Group	Mean	SD	Min	Max
SDA [°]	Healthy	9.5	2.5	5.9	14.3
	SND	17.3	5.5	10.0	36.0
VPD [%]	Healthy	5.5	4.9	0.1	16.4
	SND	13.6	11.6	0.39	54.7
V_T [cm^3]	Healthy	18.1	4.7	12.2	30.5
	SND	16.5	3.1	12.1	23.1
SDI [$°/cm^3$]	Healthy	3.8	3.2	0.6	12.0
	SND	16.5	14.3	1.3	62.9

particular, intergroup analysis shown statistical significant differences in SDA (p <0.001), in VPD (p < 0.05) and in SDI (p < 0.001) between healthy and SND subjects. No significant difference was found in VT between groups (p > 0.05).
Only the first (PC1) and the second (PC2) components resulting from the PCA were retained. These two components explained 86.6% of the sample variance. For PC1, higher values of correlation coefficient were found for SDI (0.97, p<0.001) and for SD (0.89, p<0.001), on the other hand PC2 seemed to be more correlated with VT (0.94, p<0.001) than the other morphological variables. In Table 5.2 all the calculated correlation coefficients are detailed.

Table 5.2: Eighenvalues and Explained variance of the retained principal components and their corresponding Pearson's correlation coefficient for the analysed morphological variables. The analysed parameters are: Septal deviation angle (SDA), percentage of volume difference (PVD), total volume (VT) and septal deviation index (SDI).

Principal component	Explained Variance (%)	R			
		SDA	PVD	V_T	SDI
PC1	57.0	0.75	0.89	0.12	0.96
PC2	29.6	-0.40	0.19	0.94	0.12

Discussion

In otorhinolaryngology, nasal septal deviation is one of the most frequent diagnoses and it is generally based on the evaluation of patient's symptoms and on anterior rhinoscopic outcomes [161]. This clinical analysis is accompanied by quantitative diagnostic methods used to demonstrate the septal deviation, such as endoscopy, anterior rhinoscopy, acoustic rhinometry, rhinomanometry and CT images [162, 179, 180]. In particular, cross-sectional images allow correlating patient's symptoms to the airway anatomy of both anterior and posterior nasal cavity [181]. In this context, CBCT imaging modality is emerging due to its reduction of the effective dose of radiation, its accuracy and accessibility [151, 182].
In this study, we analysed 46 CBCT images belonging to dental patients whose otolaryngological diagnosis is unknown to assess whether there was a significant difference in four morphological parameters (SDA, VDP, VT and SNI) between SND and healthy subjects. This analysis was performed in order to assess whether quantitative and evidence-based morphometric parameters may be useful in nasal septal deviation diagnosis and to test the validity of a proposed synthetic index summarizing these parameters.
Two experienced operators divided all the images into healthy and NSD groups. An excellent level of agreement, with Cohen's $\kappa = 0.86$, was found suggesting not only concordance between operators, but also the adequacy of the CBCT images for the proposed task. Regarding volumetric and angular measurement, the proposed method appears repeatable, since the measurement error is less than 1% of the variance of the sample for both measures. Volume analysis was made after images segmentation, which can be done manually or automatically; the first technique is the most accurate but it is also time consuming [167, 183, 184]. In this study we began with automatic segmentation and subsequently we refined its outcome manually.

As expected, our results revealed the presence of a significant difference in septal deviation angle between healthy and NSD subjects; this is reasonable, since the deformation of the bony structures of the nasal septum is the primary but not the only, nasal structural change in NSD subjects. A significant difference was also found between groups in the percentage of volume difference between the left and right side of nasal airways. This value is independent of subject size and consequently of his/her airway dimension. Therefore it can be a useful three-dimensional index to assess the balance of volume in the two different sides of the airways. In our study we found higher values of VPD in NSD subjects, suggesting a paradoxical hypertrophy, which is an acquired phenomenon or a congenital dimensional difference of turbinates in the nasal cavity, opposite side to the septal deviation [156, 157].

Our results showed that SDA and VDP can characterize NSD subjects. For this reason, we decided to merge them into a single parameter, the SDI, which is directly proportional to them and indirectly proportional to the total volume of nasal airways. This index has significantly higher values in NSD than in healthy subjects and appears to be a useful parameter to evaluate the deviation of the septum, since it takes various factors contributing to subject respiration into account. SDI is robust to the variation of only one parameter between SDA and VDP, which may separately contribute to patient's breathing, and takes into account that septal deviations may create more or less discomfort to the subject depending on the size of his/her nasal airway. Moreover, this index showed the highest correlation with the first PC, which expresses 57.0% of the sample variability.

In multivariate analysis, only PC1 and PC2 were retained. PC1 highly correlates with all the morphological parameters that have significantly higher values in NSD than in healthy subjects. This component is therefore more related to factors that identify nasal septal deviation, rather than with the size of the airway. On the contrary, PC2 (29.6% of explained variance) is highly related to the nasal airway size of the subject, so it is less suited for representing the analysed sample. This is also evidenced by the non-significant difference in terms of VT in the analysed groups.

Conclusion

In the current study four three-dimensional morphological parameters were analysed to evaluate their usefulness in assessing the deviation of the nasal septum. Retrospectively selected CBCT images, which allowed to accurately assess the morphology of the airways of the patient reducing the dose of radiation and therefore its invasiveness, were used to

the scope.

Among the analysed parameters, the proposed SDI index seems to be the most suitable for the quantitative assessment of nasal septal deviation, since it summarizes different morphometric factors. Further investigation shall expand the study to patient with clinically assessed alterations in respiratory function and nasal airways patency.

Chapter 6

Conclusions

Image analysis is widely applied in medicine, since it allows clinicians to quantitatively assess patient morphology, thus providing a useful diagnostic tool that can be used in daily diagnosis. In maxillofacial imaging, different kinds of biological tissues need to be imaged at the same time for a successful diagnosis, requiring, sometimes, the use of different acquisition modalities.
In this PhD thesis, various approaches were used to face different maxillofacial tasks, pointing out the possible improvement that can be reached in daily diagnosis. Moreover, it showed the possibility to improve computer-aided maxillofacial imaging for quantitative, accurate and reliable assessment of patient condition.

Hard tissue imaging

Among the possible imaging modalities, CBCT represents a useful tool for hard tissue imaging in the craniofacial complex. Due to its high resolution, isotropic voxels and the good contrast of hard tissue structures, it is suitable for maxillofacial applications.
In the third chapter, we proposed different studies that focused on image segmentation, registration and artifact reduction applied to the automatic extraction of cephalometric landmarks in CBCT data.
In particular, to obtain a three-dimensional model of the bony structures contained in the FOV, a fully automatic segmentation algorithm was developed. Our findings show high level of accuracy, comparable with manual thresholding, which represents the most used segmentation approach in maxillofacial imaging.
Moreover, a specific algorithm was developed for mandibular condyle segmentation. Also in this case, high level of accuracy were reached. In particular, the proposed method allows to improve the segmentation of the outer condylar surface as well as the segmentation of

the inner trabecular bone structures.

These segmentation methods, combined with automatic image registration techniques, were used to automatically estimate the most used cephalometric landmarks. The proposed method allows to estimate 21 cephalometric landmarks using an atlas based approach with limited a priori information. Obtained validation results show an annotation error comparable to the ones reached from other research groups, reducing the amount prior knowledge about the geometry and location specific each landmark.

Landmark estimation process may be affected by the presence of metal artifacts. For this reason, in this thesis we evaluated the expression of metal artifact varying image parameters. The quantification of these artifacts was performed using a fully automatic process developed by our research group. This evaluation allowed us to identify those parameters that affect metal object segmentation and background noise.

The results obtained from the quantification of metal artifacts helped us in the development of an efficient metal artifact reduction algorithm, which proved to be an valuable tool that improves both image quality and hard tissue segmentation.

In conclusion, in this section all the main issues related to hard tissue image processing in CBCT data were studied. Our results show that the automatic extraction of craniofacial feature is possible and can lead to the development of clinically useful tools. Nevertheless further studies should be conducted in order to improve image quality, segmentation accuracy and landmark estimation.

Soft tissue imaging

In the fourth chapter we studied the application of stereophotogrammetric systems and laser scanners for the development of computer aided approaches for facial morphology evaluation.

Stereophotogrammetric systems were proved to be suitable for the proposed task. In this doctoral thesis the obtained 3D images were used to evaluate facial asymmetry. In particular, a quantitative and facial third-based method for the evaluation the asymmetry of patient face was developed. Our findings show a high level of accuracy and reproducibility in asymmetry assessment both on healthy and pathological subjects.

Moreover, stereophotogrammetric images were fused with the digital models of patient dental arches obtained using a dental laser scanner. The proposed approach was based on automatic surface registration techniques and allows to obtain a virtual model of patient face that takes into account at the same time the relationship between patient face and

dentition in a non-invasive way.
The presented studies pointed out the possible applications of optical systems for the assessment of facial morphology. Moreover it shows how the application of registration techniques may allows the integration of different image modalities, providing a three-dimensional model of the patient face that may be used for virtual treatment planning and follow up evaluations.

Upper airway imaging

Finally, in the fifth chapter a method for nasal septal deviation in CBCT data is presented. The results of this study show that CBCT images allow the segmentation of upper airway in a reproducible way. Moreover, the obtained virtual models of upper airway were used to perform volumetric assessment improving the quantification of nasal septum deviation. Furthermore, the proposed method allow to define a new index for quantification of septal deviation, which may help clinician during deviation diagnosis.
From this study, it is possible to conclude that 3D airway modelling can be a valuable diagnostic tool. The use of such virtual models will make the clinician able to navigate and deeply understand the complex anatomy of the patient, learning important information that can enrich the diagnostic process.

General conclusions

In conclusion, we proved that the application of image processing techniques may help in the development of new diagnostic tools for maxillofacial applications. This PhD thesis has helped creating a good basis for future studies on the application of imaging techniques in oral and maxillofacial applications.
Although the clinical influence of the proposed techniques could not be fully evaluated in this thesis, it represents a starting point for further improvement and evaluation of the proposed applications. New studies should focus on algorithm optimization, validation on larger clinical datasets and evaluation of the benefits that computer aided approach provides to the patient. Furthermore, it was pointed out that the integration of different image modalities can lead to the creation of a complete three-dimensional virtual model of patient craniofacial anatomy. With this doctoral thesis, we provide a solid basis for future studies on image data fusion that will led to the creation of the virtual patient model.

Bibliography

[1] S Thaller, JP Bradley, and Joe I Garri. *Craniofacial surgery*. CRC Press, 2007.

[2] C Sforza, M de Menezes, and V Ferrario. Soft-and hard-tissue facial anthropometry in three dimensions: what's new. *Journal of anthropological sciences*, 91:159–184, 2013.

[3] KA Eaton, PA Reynolds, SK Grayden, and NHF Wilson. A vision of dental education in the third millennium. *British dental journal*, 205(5):261–271, 2008.

[4] DA Tyndall, JB Price, S Tetradis, SD Ganz, C Hildebolt, and WC Scarfe. Position statement of the american academy of oral and maxillofacial radiology on selection criteria for the use of radiology in dental implantology with emphasis on cone beam computed tomography. *Oral surgery, oral medicine, oral pathology and oral radiology*, 113(6):817–826, 2012.

[5] CHF Hämmerle, L Cordaro, N Assche, GI Benic, M Bornstein, F Gamper, K Gotfredsen, D Harris, M Hürzeler, R Jacobs, et al. Digital technologies to support planning, treatment, and fabrication processes and outcome assessments in implant dentistry. summary and consensus statements. the 4th eao consensus conference 2015. *Clinical oral implants research*, 26(S11):97–101, 2015.

[6] SA Centenero and F Hernández-Alfaro. 3d planning in orthognathic surgery: Cad/cam surgical splints and prediction of the soft and hard tissues results–our experience in 16 cases. *Journal of Cranio-Maxillofacial Surgery*, 40(2):162–168, 2012.

[7] Y Gan, Z Xia, J Xiong, Q Zhao, Y Hu, and J Zhang. Toward accurate tooth segmentation from computed tomography images using a hybrid level set model. *Medical physics*, 42(1):14–27, 2015.

[8] DX Ji, SH Ong, and KWC Foong. A level-set based approach for anterior teeth segmentation in cone beam computed tomography images. *Computers in biology and medicine*, 50:116–128, 2014.

[9] L Wang, Y Gao, F Shi, G Li, K Chen, Z Tang, JJ Xia, and D Shen. Automated segmentation of dental cbct image with prior-guided sequential random forests. *Medical physics*, 43(1):336–346, 2016.

[10] ST Gollmer and TM Buzug. Fully automatic shape constrained mandible segmentation from cone-beam ct data. In *2012 9th IEEE International Symposium on Biomedical Imaging (ISBI)*, pages 1272–1275. IEEE, 2012.

[11] MEH Wagner, N Gellrich, K Friese, M Becker, F Wolter, JT Lichtenstein, M Stoetzer, M Rana, and H Essig. Model-based segmentation in orbital volume measurement with cone beam computed tomography and evaluation against current concepts. *International journal of computer assisted radiology and surgery*, 11(1):1–9, 2016.

[12] T Xi, R Schreurs, WJ Heerink, SJ Bergé, and TJJ Maal. A novel region-growing based semi-automatic segmentation protocol for three-dimensional condylar reconstruction using cone beam computed tomography (cbct). *PloS one*, 9(11):e111126, 2014.

[13] A Sinha, S Leonard, A Reiter, M Ishii, RH Taylor, and GD Hager. Automatic segmentation and statistical shape modeling of the paranasal sinuses to estimate natural variations. In *SPIE Medical Imaging*, pages 97840D–97840D. International Society for Optics and Photonics, 2016.

[14] NA Alsufyani, A Hess, M Noga, N Ray, MAQ Al-Saleh, MO Lagravère, and PW Major. New algorithm for semiautomatic segmentation of nasal cavity and pharyngeal airway in comparison with manual segmentation using cone-beam computed tomography. *American Journal of Orthodontics and Dentofacial Orthopedics*, 150(4):703–712, 2016.

[15] H Luebbers, P Messmer, JA Obwegeser, RA Zwahlen, R Kikinis, KW Graetz, and F Matthews. Comparison of different registration methods for surgical navigation in cranio-maxillofacial surgery. *Journal of Cranio-Maxillofacial Surgery*, 36(2):109–116, 2008.

[16] H Yu, SG Shen, X Wang, L Zhang, and S Zhang. The indication and application of computer-assisted navigation in oral and maxillofacial surgeryâ€"shanghai's expe-

rience based on 104 cases. *Journal of Cranio-Maxillofacial Surgery*, 41(8):770–774, 2013.

[17] MAQ Al-Saleh, JL Jaremko, N Alsufyani, Z Jibri, H Lai, and PW Major. Assessing the reliability of mri-cbct image registration to visualize temporomandibular joints. *Dentomaxillofacial Radiology*, 44(6):20140244, 2015.

[18] DJ Loeffelbein, M Souvatzoglou, V Wankerl, A Martinez-Möller, J Dinges, M Schwaiger, and AJ Beer. Pet-mri fusion in head-and-neck oncology: current status and implications for hybrid pet/mri. *Journal of Oral and Maxillofacial Surgery*, 70(2):473–483, 2012.

[19] T Flügge, W Derksen, J Poel, B Hassan, K Nelson, and D Wismeijer. Registration of cone beam computed tomography data and intraoral surface scans–a prerequisite for guided implant surgery with cad/cam drilling guides. *Clinical Oral Implants Research*, 2016.

[20] E Nkenke, S Zachow, M Benz, T Maier, K Veit, M Kramer, S Benz, G Häusler, FW Neukam, and M Lell. Fusion of computed tomography data and optical 3d images of the dentition for streak artefact correction in the simulation of orthognathic surgery. *Dentomaxillofacial Radiology*, 2014.

[21] K Stokbro, E Aagaard, P Torkov, RB Bell, and T Thygesen. Virtual planning in orthognathic surgery. *International journal of oral and maxillofacial surgery*, 43(8):957–965, 2014.

[22] RM Haralick and LG Shapiro. Image segmentation techniques. *Computer vision, graphics, and image processing*, 29(1):100–132, 1985.

[23] DL Pham, C Xu, and JL Prince. Current methods in medical image segmentation 1. *Annual review of biomedical engineering*, 2(1):315–337, 2000.

[24] J Modersitzki. *Numerical Methods for Image Registration (Numerical Mathematics and Scientific Computation)*. Oxford university press USA, 2004.

[25] LG Brown. A survey of image registration techniques. *ACM computing surveys (CSUR)*, 24(4):325–376, 1992.

[26] W Rui and L Minglu. An overview of medical image registration. In *Computational Intelligence and Multimedia Applications, 2003. ICCIMA 2003. Proceedings. Fifth International Conference on*, pages 385–390. IEEE, 2003.

[27] JBA Maintz and Max A Viergever. An overview of medical image registration methods. *UU-CS*, (1998-22), 1998.

[28] WA Kalender. *Computed tomography: fundamentals, system technology, image quality, applications*. John Wiley & Sons, 2011.

[29] R Jacobs and M Quirynen. Dental cone beam computed tomography: justification for use in planning oral implant placement. *Periodontology 2000*, 66(1):203–213, 2014.

[30] K Lee, J Song, J Cho, and H Hwang. Influence of head motion on the accuracy of 3d reconstruction with cone-beam ct: Landmark identification errors in maxillofacial surface model. *PloS one*, 11(4):e0153210, 2016.

[31] T Rodet, F Noo, and M Defrise. The cone-beam algorithm of feldkamp, davis, and kress preserves oblique line integrals. *Medical physics*, 31(7):1972–1975, 2004.

[32] R Schulze, U Heil, D Gross, DD Bruellmann, E Dranischnikow, U Schwanecke, and E Schoemer. Artefacts in cbct: a review. *Dentomaxillofacial Radiology*, 2014.

[33] J Al Abduwani, L ZilinSkiene, S Colley, and S Ahmed. Cone beam ct paranasal sinuses versus standard multidetector and low dose multidetector ct studies. *American journal of otolaryngology*, 37(1):59–64, 2016.

[34] AC Miracle and SK Mukherji. Conebeam ct of the head and neck, part 2: clinical applications. *American Journal of Neuroradiology*, 30(7):1285–1292, 2009.

[35] R Pauwels, H Stamatakis, H Bosmans, R Bogaerts, R Jacobs, K Horner, and K Tsiklakis. Quantification of metal artifacts on cone beam computed tomography images. *Clinical oral implants research*, 24(A100):94–99, 2013.

[36] KF Vasconcelos, LFP Nicolielo, MC Nascimento, F Haiter-Neto, FN Bóscolo, J Van Dessel, M Ezeldeen, I Lambrichts, and R Jacobs. Artefact expression associated with several cone-beam computed tomographic machines when imaging root filled teeth. *International endodontic journal*, 48(10):994–1000, 2015.

[37] GI Benic, M Sancho-Puchades, RE Jung, H Deyhle, and CHF Hämmerle. In vitro assessment of artifacts induced by titanium dental implants in cone beam computed tomography. *Clinical oral implants research*, 24(4):378–383, 2013.

[38] D Prell, Y Kyriakou, M Beister, and WA Kalender. A novel forward projection-based metal artifact reduction method for flat-detector computed tomography. *Physics in medicine and biology*, 54(21):6575, 2009.

[39] Q Wang, L Li, L Zhang, Z Chen, and K Kang. A novel metal artifact reducing method for cone-beam ct based on three approximately orthogonal projections. *Physics in medicine and biology*, 58(1):1, 2012.

[40] M Meilinger, C Schmidgunst, O Schütz, and EW Lang. Metal artifact reduction in cone beam computed tomography using forward projected reconstruction information. *Zeitschrift für Medizinische Physik*, 21(3):174–182, 2011.

[41] J Kim, H Nam, and R Lee. Development of a new metal artifact reduction algorithm by using an edge preserving method for cbct imaging. *Journal of the Korean Physical Society*, 67(1):180–188, 2015.

[42] S Tohnak, AJH Mehnert, M Mahoney, and S Crozier. Dental ct metal artefact reduction based on sequential substitution. *Dentomaxillofacial Radiology*, 2014.

[43] R Pauwels, O Nackaerts, N Bellaiche, H Stamatakis, K Tsiklakis, An Walker, H Bosmans, R Bogaerts, R Jacobs, and K Horner. Variability of dental cone beam ct grey values for density estimations. *The British journal of radiology*, 86(1021):20120135–20120135, 2013.

[44] M Codari, M Caffini, GM Tartaglia, C Sforza, and G Baselli. Computer-aided cephalometric landmark annotation for cbct data. *International Journal of Computer Assisted Radiology and Surgery*, pages 1–9, 2016.

[45] L Wang, KC Chen, Y Gao, F Shi, S Liao, G Li, SGF Shen, J Yan, PKM Lee, B Chow, et al. Automated bone segmentation from dental cbct images using patch-based sparse representation and convex optimization. *Medical physics*, 41(4):043503, 2014.

[46] R Pauwels, R Jacobs, H Bosmans, P Pittayapat, P Kosalagood, O Silkosessak, and S Panmekiate. Automated implant segmentation in cone-beam ct using edge detection and particle counting. *International journal of computer assisted radiology and surgery*, 9(4):733–743, 2014.

[47] JH Choi, S Baek, Y Kim, T Son, S Park, and K Lee. Automatic detection of inferior alveolar nerve canal from cone-beam computed tomography images for dental

surgery planning. *Medicine Meets Virtual Reality 21: NextMed/MMVR21*, 196:61, 2014.

[48] A Gupta, OP Kharbanda, V Sardana, R Balachandran, and HK Sardana. A knowledge-based algorithm for automatic detection of cephalometric landmarks on cbct images. *International journal of computer assisted radiology and surgery*, 10(11):1737–1752, 2015.

[49] T Xi, B Van Loon, P Fudalej, S Berge, G Swennen, and T Maal. Validation of a novel semi-automated method for three-dimensional surface rendering of condyles using cone beam computed tomography data. *International journal of oral and maxillofacial surgery*, 42(8):1023–1029, 2013.

[50] J Gateno, JJ Xia, and JF Teichgraeber. New 3-dimensional cephalometric analysis for orthognathic surgery. *Journal of Oral and Maxillofacial Surgery*, 69(3):606–622, 2011.

[51] G Bettega, Y Payan, B Mollard, A Boyer, B Raphaël, and S Lavallee. A simulator for maxillofacial surgery integrating 3d cephalometry and orthodontia. *Computer Aided Surgery*, 5(3):156–165, 2000.

[52] C A Hurst, B L Eppley, R J Havlik, and AM Sadove. Surgical cephalometrics: applications and developments. *Plastic and reconstructive surgery*, 120(6):92e–104e, 2007.

[53] P Pittayapat, N Limchaichana-Bolstad, G Willems, and R Jacobs. Three-dimensional cephalometric analysis in orthodontics: a systematic review. *Orthodontics & craniofacial research*, 17(2):69–91, 2014.

[54] GRJ Swennen, FAC Schutyser, and J Hausamen. *Three-dimensional cephalometry: a color atlas and manual*. Springer Science & Business Media, 2005.

[55] A Al-Okshi, C Lindh, H Salé, M Gunnarsson, and M Rohlin. Effective dose of cone beam ct (cbct) of the facial skeleton: a systematic review. *The British journal of radiology*, 88(1045):20140658, 2014.

[56] A Weissheimer, LM de Menezes, GT Sameshima, R Enciso, J Pham, and D Grauer. Imaging software accuracy for 3-dimensional analysis of the upper airway. *American Journal of Orthodontics and Dentofacial Orthopedics*, 142(6):801–813, 2012.

[57] Y Sun, H Luebbers, JO Agbaje, S Schepers, L Vrielinck, I Lambrichts, and C Politis. Validation of anatomical landmarks-based registration for image-guided surgery: an in-vitro study. *Journal of Cranio-Maxillofacial Surgery*, 41(6):522–526, 2013.

[58] GRJ Swennen, F Schutyser, EL Barth, P De Groeve, and A De Mey. A new method of 3-d cephalometry part i: the anatomic cartesian 3-d reference system. *Journal of craniofacial surgery*, 17(2):314–325, 2006.

[59] I Titiz, M Laubinger, T Keller, K Hertrich, and U Hirschfelder. Repeatability and reproducibility of landmarksâ€"a three-dimensional computed tomography study. *The European Journal of Orthodontics*, page cjq190, 2011.

[60] RA Katkar, C Kummet, D Dawson, L Moreno U, V Allareddy, M Finkelstein, and A Ruprecht. Comparison of observer reliability of three-dimensional cephalometric landmark identification on subject images from galileos and i-cat cone beam ct. *Dentomaxillofacial Radiology*, 42(9):20130059, 2013.

[61] Y Cheng, WK Leow, and TC Lim. Automatic identification of frankfurt plane and mid-sagittal plane of skull. *Applications of Computer Vision (WACV), 2012 IEEE Workshop on*, pages 233–238, 2012.

[62] J Keustermans, W Mollemans, D Vandermeulen, and P Suetens. Automated cephalometric landmark identification using shape and local appearance models. *Pattern Recognition (ICPR), 2010 20th International Conference on*, pages 2464–2467, 2010.

[63] J Keustermans, D Smeets, D Vandermeulen, and P Suetens. Automated cephalometric landmark localization using sparse shape and appearance models. *Machine Learning in Medical Imaging*, pages 249–256, 2011.

[64] S Shahidi, E Bahrampour, E Soltanimehr, A Zamani, M Oshagh, M Moattari, and A Mehdizadeh. The accuracy of a designed software for automated localization of craniofacial landmarks on cbct images. *BMC medical imaging*, 14(1):1, 2014.

[65] M Makram and H Kamel. Reeb graph for automatic 3d cephalometry. *IJIP*, 8:17–29, 2014.

[66] W De Vos, J Casselman, and GRJ Swennen. Cone-beam computerized tomography (cbct) imaging of the oral and maxillofacial region: a systematic review of the

literature. *International journal of oral and maxillofacial surgery*, 38(6):609–625, 2009.

[67] M Sagawa, Y Miyoseta, Y Hayakawa, and A Honda. Comparison of two-and three-dimensional filtering methods to improve image quality in multiplanar reconstruction of cone-beam computed tomography. *Oral radiology*, 25(2):154–158, 2009.

[68] B Hassan, PC Souza, R Jacobs, S de Azambuja Berti, and P van der Stelt. Influence of scanning and reconstruction parameters on quality of three-dimensional surface models of the dental arches from cone beam computed tomography. *Clinical oral investigations*, 14(3):303–310, 2010.

[69] DJC MacKay. *Information theory, inference and learning algorithms*. Cambridge university press, 2003.

[70] DL Pham, C Xu, and JL Prince. Current methods in medical image segmentation 1. *Annual review of biomedical engineering*, 2(1):315–337, 2000.

[71] HP Ng, SH Ong, KWC Foong, PS Goh, and WL Nowinski. Medical image segmentation using k-means clustering and improved watershed algorithm. In *2006 IEEE Southwest Symposium on Image Analysis and Interpretation*, pages 61–65. IEEE, 2006.

[72] DJC MacKay. *Information theory, inference and learning algorithms*. Cambridge university press, 2003.

[73] Y Gao, Y Zhan, and D Shen. Incremental learning with selective memory (ilsm): Towards fast prostate localization for image guided radiotherapy. *IEEE transactions on medical imaging*, 33(2):518–534, 2014.

[74] J Liu, W Gao, S Huang, and WL Nowinski. A model-based, semi-global segmentation approach for automatic 3-d point landmark localization in neuroimages. *IEEE Transactions on Medical Imaging*, 27(8):1034–1044, 2008.

[75] S Frantz, K Rohr, and HS Stiehl. Localization of 3d anatomical point landmarks in 3d tomographic images using deformable models. In *International Conference on Medical Image Computing and Computer-Assisted Intervention*, pages 492–501. Springer, 2000.

[76] JM Fitzpatrick, DLG Hill, and CR Maurer Jr. Image registration. *Handbook of medical imaging*, 2:447–513, 2000.

[77] A Myronenko and X Song. Intensity-based image registration by minimizing residual complexity. *IEEE Transactions on Medical Imaging*, 29(11):1882–1891, 2010.

[78] D Rueckert, LI Sonoda, C Hayes, DLG Hill, MO Leach, and DJ Hawkes. Nonrigid registration using free-form deformations: application to breast mr images. *IEEE transactions on medical imaging*, 18(8):712–721, 1999.

[79] F Baan, J Liebregts, T Xi, R Schreurs, M de Koning, S Bergé, and T Maal. A new 3d tool for assessing the accuracy of bimaxillary surgery: The orthognathicanalyser. *PloS one*, 11(2):e0149625, 2016.

[80] M Puisoru, N Forna, AM Fatu, R Fuatu, and C Fuatu. Analysis of mandibular variability in humans of different geographic areas. *Annals of Anatomy-Anatomischer Anzeiger*, 188(6):547–554, 2006.

[81] W Schlicher, I Nielsen, JC Huang, K Maki, DC Hatcher, and AJ Miller. Consistency and precision of landmark identification in three-dimensional cone beam computed tomography scans. *The European Journal of Orthodontics*, page cjq144, 2011.

[82] M Sancho-Puchades, CHF Hämmerle, and GI Benic. In vitro assessment of artifacts induced by titanium, titanium–zirconium and zirconium dioxide implants in cone-beam computed tomography. *Clinical oral implants research*, 26(10):1222–1228, 2015.

[83] N Kuusisto, PK Vallittu, LVJ Lassila, and S Huumonen. Evaluation of intensity of artefacts in cbct by radio-opacity of composite simulation models of implants in vitro. *Dentomaxillofacial Radiology*, 44(2):20140157, 2014.

[84] B De Man, J Nuyts, P Dupont, G Marchal, and P Suetens. Metal streak artifacts in x-ray computed tomography: a simulation study. *IEEE Transactions on Nuclear Science*, 46(3):691–696, 1999.

[85] B Hassan, ME Metska, AR Ozok, P van der Stelt, and PR Wesselink. Comparison of five cone beam computed tomography systems for the detection of vertical root fractures. *Journal of endodontics*, 36(1):126–129, 2010.

[86] SLS Melo, EA Bortoluzzi, M Abreu, LR Corrêa, and M Corrêa. Diagnostic ability of a cone-beam computed tomography scan to assess longitudinal root fractures in prosthetically treated teeth. *Journal of endodontics*, 36(11):1879–1882, 2010.

[87] FF Costa, BF Gaia, OS Umetsubo, and MGP Cavalcanti. Detection of horizontal root fracture with small-volume cone-beam computed tomography in the presence and absence of intracanal metallic post. *Journal of endodontics*, 37(10):1456–1459, 2011.

[88] FF Costa, BF Gaia, OS Umetsubo, LR Pinheiro, IP Tortamano, and MGP Cavalcanti. Use of large-volume cone-beam computed tomography in identification and localization of horizontal root fracture in the presence and absence of intracanal metallic post. *Journal of endodontics*, 38(6):856–859, 2012.

[89] PF da Silveira, MB Vizzotto, GS Liedke, HLD da Silveira, F Montagner, and HED da Silveira. Detection of vertical root fractures by conventional radiographic examination and cone beam computed tomography–an in vitro analysis. *Dental Traumatology*, 29(1):41–46, 2013.

[90] ME Guerrero, R Jacobs, M Loubele, F Schutyser, P Suetens, and D van Steenberghe. State-of-the-art on cone beam ct imaging for preoperative planning of implant placement. *Clinical oral investigations*, 10(1):1–7, 2006.

[91] K Kamburoğlu, E Kolsuz, S Murat, H Eren, S Yüksel, and CS Paksoy. Assessment of buccal marginal alveolar peri-implant and periodontal defects using a cone beam ct system with and without the application of metal artefact reduction mode. *Dentomaxillofacial Radiology*, 42(8):20130176, 2013.

[92] LW Goldman. Principles of ct: radiation dose and image quality. *Journal of nuclear medicine technology*, 35(4):213–225, 2007.

[93] JA Hartigan and MA Wong. Algorithm as 136: A k-means clustering algorithm. *Journal of the Royal Statistical Society. Series C (Applied Statistics)*, 28(1):100–108, 1979.

[94] DLG Hill, PG Batchelor, M Holden, and DJ Hawkes. Medical image registration. *Physics in medicine and biology*, 46(3):R1, 2001.

[95] R Molteni. Prospects and challenges of rendering tissue density in hounsfield units for cone beam computed tomography. *Oral surgery, oral medicine, oral pathology and oral radiology*, 116(1):105–119, 2013.

[96] FG Draenert, E Coppenrath, P Herzog, S Müller, and UG Mueller-Lisse. Beam hardening artefacts occur in dental implant scans with the newtom® cone beam ct but not with the dental 4-row multidetector ct. *Dentomaxillofacial Radiology*, 2014.

[97] J Chindasombatjaroen, N Kakimoto, S Murakami, Y Maeda, and S Furukawa. Quantitative analysis of metallic artifacts caused by dental metals: comparison of cone-beam and multi-detector row ct scanners. *Oral Radiology*, 27(2):114–120, 2011.

[98] F Esmaeili, M Johari, P Haddadi, and M Vatankhah. Beam hardening artifacts: comparison between two cone beam computed tomography scanners. *Journal of dental research, dental clinics, dental prospects*, 6(2):49–53, 2012.

[99] D Helvacioglu-Yigit, HD Kocasarac, B Bechara, and M Noujeim. Evaluation and reduction of artifacts generated by 4 different root-end filling materials by using multiple cone-beam computed tomography imaging settings. *Journal of endodontics*, 42(2):307–314, 2016.

[100] R Pauwels, L Seynaeve, JCG Henriques, C de Oliveira-Santos, PC Souza, FH Westphalen, IRF Rubira-Bullen, RF Ribeiro-Rotta, MIB Rockenbach, F Haiter-Neto, et al. Optimization of dental cbct exposures through mas reduction. *Dentomaxillofacial Radiology*, 44(9):20150108, 2015.

[101] R Pauwels, R Jacobs, R Bogaerts, H Bosmans, and S Panmekiate. Reduction of scatter-induced image noise in cone beam computed tomography: effect of field of view size and position. *Oral surgery, oral medicine, oral pathology and oral radiology*, 121(2):188–195, 2016.

[102] R Spin-Neto, E Gotfredsen, and A Wenzel. Impact of voxel size variation on cbct-based diagnostic outcome in dentistry: a systematic review. *Journal of digital imaging*, 26(4):813–820, 2013.

[103] D Schneider, P Marquardt, M Zwahlen, and RE Jung. A systematic review on the accuracy and the clinical outcome of computer-guided template-based implant dentistry. *Clinical oral implants research*, 20(s4):73–86, 2009.

[104] B AL-RAWI, B Hassan, B Vandenberge, and R Jacobs. Accuracy assessment of three-dimensional surface reconstructions of teeth from cone beam computed tomography scans. *Journal of oral rehabilitation*, 37(5):352–358, 2010.

[105] M Bal and L Spies. Metal artifact reduction in ct using tissue-class modeling and adaptive prefiltering. *Medical physics*, 33(8):2852–2859, 2006.

[106] D Garcia. Robust smoothing of gridded data in one and higher dimensions with missing values. *Computational statistics & data analysis*, 54(4):1167–1178, 2010.

[107] R Ning and Y Zhang. Method and apparatus for 3d metal and high-density artifact correction for cone-beam and fan-beam ct imaging, July 24 2012. US Patent 8,229,246.

[108] S Dong, J Dong, S Li, and J Hsieh. Method and apparatus for metal artifact elimination in a medical image, October 24 2014. US Patent App. 14/522,783.

[109] D Yang and RA Senn. Metal artifacts reduction for cone beam ct, December 1 2015. US Patent 9,202,296.

[110] O Nackaerts, F Maes, H Yan, P Couto Souza, R Pauwels, and R Jacobs. Analysis of intensity variability in multislice and cone beam computed tomography. *Clinical oral implants research*, 22(8):873–879, 2011.

[111] WJH Veldkamp, RMS Joemai, AJ van der Molen, and J Geleijns. Development and validation of segmentation and interpolation techniques in sinograms for metal artifact suppression in ct. *Medical physics*, 37(2):620–628, 2010.

[112] TJM Hoppenreijs, T Maal, and T Xi. Evaluation of condylar resorption before and after orthognathic surgery. In *Seminars in Orthodontics*, volume 19, pages 106–115. Elsevier, 2013.

[113] KH Zou, SK Warfield, A Bharatha, CMC Tempany, MR Kaus, SJ Haker, WM Wells, FA Jolesz, and R Kikinis. Statistical validation of image segmentation quality based on a spatial overlap index 1: Scientific reports. *Academic radiology*, 11(2):178–189, 2004.

[114] M de Menezes, R Rosati, VF Ferrario, and C Sforza. Accuracy and reproducibility of a 3-dimensional stereophotogrammetric imaging system. *Journal of Oral and Maxillofacial Surgery*, 68(9):2129–2135, 2010.

[115] JM Plooij, GRJ Swennen, FA Rangel, TJJ Maal, FAC Schutyser, EM Bronkhorst, AM Kuijpers-Jagtman, and SJ Bergé. Evaluation of reproducibility and reliability of 3d soft tissue analysis using 3d stereophotogrammetry. *International journal of oral and maxillofacial surgery*, 38(3):267–273, 2009.

[116] KP Lincoln, AYT Sun, TJ Prihoda, and AJ Sutton. Comparative accuracy of facial models fabricated using traditional and 3d imaging techniques. *Journal of Prosthodontics*, 2015.

[117] J Meulstee, L Verhamme, W Borstlap, H Delye, S Bergé, and T Maal. The use of 3d stereophotogrammetry in the post-operative treatment and evaluation of endoscopic assisted repair of craniosynostosis. *International Journal of Oral and Maxillofacial Surgery*, 42(10):1215, 2013.

[118] TJ Verhoeven, C Coppen, R Barkhuysen, EM Bronkhorst, MAW Merkx, SJ Bergé, and TJJ Maal. Three dimensional evaluation of facial asymmetry after mandibular reconstruction: validation of a new method using stereophotogrammetry. *International journal of oral and maxillofacial surgery*, 42(1):19–25, 2013.

[119] Y Kim, S Moon, P Yun, Y Lee, BE Larson, and N Lee. Evaluation of soft tissue changes around the lips after mandibular setback surgery with minimal orthodontics using three-dimensional stereophotogrammetry. *Journal of Oral and Maxillofacial Surgery*, 74(5):1044–1054, 2016.

[120] LM Galantucci. New challenges for reverse engineering in facial treatments: how can the new 3-d non invasive surface measurements support diagnosis and treatment? *Virtual and Physical Prototyping*, 5(1):3–12, 2010.

[121] TN Melvin and CJ Limb. Overview of facial paralysis: current concepts. *Facial Plastic Surgery*, 24(02):155–163, 2008.

[122] SE Bishara, PS Burkey, and JG Kharouf. Dental and facial asymmetries: a review. *The Angle orthodontist*, 64(2):89–98, 1994.

[123] RL Avelar, JG Göelzer, FG Azambuja, RB de Oliveira, MP de Oliveira, and PF Pase. Use of autologous fat graft for correction of facial asymmetry stemming from parry-romberg syndrome. *Oral Surgery, Oral Medicine, Oral Pathology, Oral Radiology, and Endodontology*, 109(2):e20–e25, 2010.

[124] J Kim, M Kang, J You, H Jee, JW Yi, and B Kim. Natural head postures of patients with facial asymmetry in frontal view are corrected after orthognathic surgeries. *Journal of Oral and Maxillofacial Surgery*, 74(2):392–398, 2016.

[125] G Thiesen, BF Gribel, and MPM Freitas. Facial asymmetry: a current review. *Dental press journal of orthodontics*, 20(6):110–125, 2015.

[126] P Claes, M Walters, and J Clement. Improved facial outcome assessment using a 3d anthropometric mask. *International journal of oral and maxillofacial surgery*, 41(3):324–330, 2012.

[127] P Chatrath, J De Cordova, SAR Nouraei, J Ahmed, and HA Saleh. Objective assessment of facial asymmetry in rhinoplasty patients. *Archives of Facial Plastic Surgery*, 9(3):184–187, 2007.

[128] T Verhoeven, T Xi, R Schreurs, S Bergé, and T Maal. Quantification of facial asymmetry: A comparative study of landmark-based and surface-based registrations. *Journal of Cranio-Maxillofacial Surgery*, 2016.

[129] D Smeets, P Claes, D Vandermeulen, and JG Clement. Objective 3d face recognition: Evolution, approaches and challenges. *Forensic science international*, 201(1):125–132, 2010.

[130] JT Richtsmeier, V Burke Deleon, and SR Lele. The promise of geometric morphometrics. *American journal of physical anthropology*, 119(S35):63–91, 2002.

[131] J Ostwald, P Berssenbrügge, D Dirksen, C Runte, K Wermker, J Kleinheinz, and S Jung. Measured symmetry of facial 3d shape and perceived facial symmetry and attractiveness before and after orthognathic surgery. *Journal of Cranio-Maxillofacial Surgery*, 43(4):521–527, 2015.

[132] J Djordjevic, AM Toma, AI Zhurov, and S Richmond. Three-dimensional quantification of facial symmetry in adolescents using laser surface scanning. *The European Journal of Orthodontics*, 36(2):125–132, 2014.

[133] VF Ferrario, C Sforza, CE Poggio, M Cova, and GM Tartaglia. Preliminary evaluation of an electromagnetic three-dimensional digitizer in facial anthropometry. *The Cleft palate-craniofacial journal*, 35(1):9–15, 1998.

[134] HO Taylor, CS Morrison, O Linden, B Phillips, J Chang, ME Byrne, SR Sullivan, and CR Forrest. Quantitative facial asymmetry: using three-dimensional photogrammetry to measure baseline facial surface symmetry. *Journal of Craniofacial Surgery*, 25(1):124–128, 2014.

[135] JM Bland and DG Altman. Statistical methods for assessing agreement between two methods of clinical measurement. *The lancet*, 327(8476):307–310, 1986.

[136] NF Berlin, P Berssenbrügge, C Runte, K Wermker, S Jung, J Kleinheinz, and D Dirksen. Quantification of facial asymmetry by 2d analysis–a comparison of recent approaches. *Journal of Cranio-Maxillofacial Surgery*, 42(3):265–271, 2014.

[137] P Berssenbrügge, N Berlin, G Kebeck, C Runte, S Jung, J Kleinheinz, and D Dirksen. 2d and 3d analysis methods of facial asymmetry in comparison. *Journal of Cranio-Maxillofacial Surgery*, 42(6):e327–e334, 2014.

[138] M Alqattan, J Djordjevic, AI Zhurov, and S Richmond. Comparison between landmark and surface-based three-dimensional analyses of facial asymmetry in adults. *The European Journal of Orthodontics*, 37(1):1–12, 2015.

[139] D Kornreich, AA Mitchell, BD Webb, I Cristian, and E Jabs. Quantitative assessment of facial asymmetry using three-dimensional surface imaging in adults: Validating the precision and repeatability of a global approach. *The Cleft Palate-Craniofacial Journal*, 53(1):126–131, 2016.

[140] U Ozsoy. Comparison of different calculation methods used to analyze facial soft tissue asymmetry: Global and partial 3d quantitative evaluation of healthy subjects. *Journal of Oral and Maxillofacial Surgery*, 2016.

[141] FA Rangel, TJJ Maal, SJ Bergé, OJC van Vlijmen, JM Plooij, F Schutyser, and AM Kuijpers-Jagtman. Integration of digital dental casts in 3-dimensional facial photographs. *American Journal of Orthodontics and Dentofacial Orthopedics*, 134(6):820–826, 2008.

[142] T Joda and GO Gallucci. The virtual patient in dental medicine. *Clinical oral implants research*, 26(6):725–726, 2015.

[143] LM Galantucci. New challenges for reverse engineering in facial treatments: How can the new 3d non-invasive surface measures support diagnoses and cures? *Virtual and Physical Prototyping*, 5(1):3–12, 2010.

[144] R Rosati, M De Menezes, A Rossetti, C Sforza, and VF Ferrario. Digital dental cast placement in 3-dimensional, full-face reconstruction: a technical evaluation. *American Journal of Orthodontics and Dentofacial Orthopedics*, 138(1):84–88, 2010.

[145] PJ Besl and ND McKay. Method for registration of 3-d shapes. In *Robotics-DL tentative*, pages 586–606. International Society for Optics and Photonics, 1992.

[146] MA Audette, FP Ferrie, and TM Peters. An algorithmic overview of surface registration techniques for medical imaging. *Medical image analysis*, 4(3):201–217, 2000.

[147] LM Galantucci, G Percoco, F Lavecchia, and E Di Gioia. Noninvasive computerized scanning method for the correlation between the facial soft and hard tissues for an integrated three-dimensional anthropometry and cephalometry. *Journal of Craniofacial Surgery*, 24(3):797–804, 2013.

[148] R Guijarro-Martinez and GRJ Swennen. Cone-beam computerized tomography imaging and analysis of the upper airway: a systematic review of the literature. *International journal of oral and maxillofacial surgery*, 40(11):1227–1237, 2011.

[149] MG Lenza, MM de O Lenza, Michel Dalstra, Birte Melsen, and PM Cattaneo. An analysis of different approaches to the assessment of upper airway morphology: a cbct study. *Orthodontics & craniofacial research*, 13(2):96–105, 2010.

[150] H Shi, WC Scarfe, and AG Farman. Upper airway segmentation and dimensions estimation from cone-beam ct image datasets. *International Journal of Computer Assisted Radiology and Surgery*, 1(3):177–186, 2006.

[151] A Yamashina, K Tanimoto, P Sutthiprapaporn, and Y Hayakawa. The reliability of computed tomography (ct) values and dimensional measurements of the oropharyngeal region using cone beam ct: comparison with multidetector ct. *Dentomaxillofacial Radiology*, 2014.

[152] X Feng, G Li, Z Qu, L Liu, K Näsström, and X Shi. Comparative analysis of upper airway volume with lateral cephalograms and cone-beam computed tomography. *American Journal of Orthodontics and Dentofacial Orthopedics*, 147(2):197–204, 2015.

[153] NL Bui, SH Ong, and KWC Foong. Automatic segmentation of the nasal cavity and paranasal sinuses from cone-beam ct images. *International journal of computer assisted radiology and surgery*, 10(8):1269–1277, 2015.

[154] R Huang, A Li, L Bi, C Li, P Young, G King, DD Feng, and Jinman Kim. A locally constrained statistical shape model for robust nasal cavity segmentation in computed tomography. In *Biomedical Imaging (ISBI), 2016 IEEE 13th International Symposium on*, pages 1334–1337. IEEE, 2016.

[155] A Sahin-Yilmaz and RM Naclerio. Anatomy and physiology of the upper airway. *Proceedings of the American Thoracic Society*, 8(1):31–39, 2011.

[156] E Egeli, L Demirci, B Yazỳcỳ, and U Harputluoglu. Evaluation of the inferior turbinate in patients with deviated nasal septum by using computed tomography. *The Laryngoscope*, 114(1):113–117, 2004.

[157] I Orhan, S Aydın, T Ormeci, and F Yılmaz. A radiological analysis of inferior turbinate in patients with deviated nasal septum by using computed tomography. *American journal of rhinology & allergy*, 28(1):e68–e72, 2014.

[158] GL Murrell. Components of the nasal examination. *Aesthetic Surgery Journal*, 33(1):38–42, 2013.

[159] AMH Wuister, NA Goto, EJ Oostveen, WU de Jong, ES van der Valk, NM Kaper, MCJ Aarts, W Grolman, and GJMG van der Heijden. Nasal endoscopy is recommended for diagnosing adults with chronic rhinosinusitis. *Otolaryngology–Head and Neck Surgery*, 150(3):359–364, 2014.

[160] D Karatas, F Yüksel, Me Sentürk, and M Dogan. The contribution of computed tomography to nasal septoplasty. *Journal of Craniofacial Surgery*, 24(5):1549–1551, 2013.

[161] B Mamikoglu, S Houser, I Akbar, B Ng, and JP Corey. Acoustic rhinometry and computed tomography scans for the diagnosis of nasal septal deviation, with clinical correlation. *Otolaryngology–Head and Neck Surgery*, 123(1):61–68, 2000.

[162] SB Eren, S Tugrul, R Dogan, B Ozucer, and O Ozturan. Objective and subjective evaluation of operation success in patients with nasal septal deviation based on septum type. *American journal of rhinology & allergy*, 28(4):e158–e162, 2014.

[163] E Akoğlu, S Karazincir, A Balcı, S Okuyucu, H Sumbas, and AŞ Dağlı. Evaluation of the turbinate hypertrophy by computed tomography in patients with deviated nasal septum. *Otolaryngology-Head and Neck Surgery*, 136(3):380–384, 2007.

[164] E Günbey, HP Günbey, S Uygun, H Karabulut, and C Cingi. Is preoperative paranasal sinus computed tomography necessary for every patient undergoing septoplasty? In *International forum of allergy & rhinology*, volume 5, pages 839–845. Wiley Online Library, 2015.

[165] HH Tso, JS Lee, JC Huang, K Maki, D Hatcher, and AJ Miller. Evaluation of the human airway using cone-beam computerized tomography. *Oral Surgery, Oral Medicine, Oral Pathology, Oral Radiology, and Endodontology*, 108(5):768–776, 2009.

[166] NL Bui, SH Ong, and KWC Foong. Automatic segmentation of the nasal cavity and paranasal sinuses from cone-beam ct images. *International journal of computer assisted radiology and surgery*, pages 1–9, 2014.

[167] RJ Robinson, J Russo, and RL Doolittle. 3d airway reconstruction using visible human data set and human casts with comparison to morphometric data. *The Anatomical Record*, 292(7):1028–1044, 2009.

[168] KRS de Souza, PVP Oltramari-Navarro, R Navarro, AC Conti, and MR de Almeida. Reliability of a method to conduct upper airway analysis in cone-beam computed tomography. *Brazilian oral research*, 27(1):48–54, 2013.

[169] J Setlur and P Goyal. Relationship between septal body size and septal deviation. *American journal of rhinology & allergy*, 25(6):397–400, 2011.

[170] A Furuhashi, S Yamada, T Shiomi, R Sasanabe, Y Aoki, Y Yamada, and Y Kazaoka. Effective three-dimensional evaluation analysis of upper airway form during oral appliance therapy in patients with obstructive sleep apnoea. *Journal of oral rehabilitation*, 40(8):582–589, 2013.

[171] L Li, H Liu, H Cheng, Y Han, C Wang, Y Chen, J Song, and D Liu. Cbct evaluation of the upper airway morphological changes in growing patients of class ii division 1 malocclusion with mandibular retrusion using twin block appliance: A comparative research. *PloS one*, 9(4):e94378, 2014.

[172] S Salerno, C Gagliardo, S Vitabile, C Militello, G Latona, M Giuffrè, AL Casto, and M Midiri. Semi-automatic volumetric segmentation of the upper airways in patients with pierre robin sequence. *The neuroradiology journal*, 27(4):487–494, 2014.

[173] I Orhan, T Ormeci, S Aydin, G Altin, E Urger, E Soylu, and F Yilmaz. Morphometric analysis of the maxillary sinus in patients with nasal septum deviation. *European Archives of Oto-Rhino-Laryngology*, 271(4):727–732, 2014.

[174] PA Yushkevich, J Piven, HC Hazlett, RG Smith, S Ho, JC Gee, and G Gerig. User-guided 3d active contour segmentation of anatomical structures: significantly improved efficiency and reliability. *Neuroimage*, 31(3):1116–1128, 2006.

[175] A Kamoen, L Dermaut, and R Verbeeck. The clinical significance of error measurement in the interpretation of treatment results. *The European Journal of Orthodontics*, 23(5):569–578, 2001.

[176] PR Burgel, JL Paillasseur, D Caillaud, I Tillie-Leblond, P Chanez, R Escamilla, T Perez, P Carré, N Roche, et al. Clinical copd phenotypes: a novel approach using principal component and cluster analyses. *European Respiratory Journal*, 36(3):531–539, 2010.

[177] I Jolliffe. *Principal component analysis*. Wiley Online Library, 2002.

[178] A Gouelle, F Mégrot, A Presedo, I Husson, A Yelnik, and G Penneçot. The gait variability index: A new way to quantify fluctuation magnitude of spatiotemporal parameters during gait. *Gait & posture*, 38(3):461–465, 2013.

[179] E Szücs and PAR Clement. Acoustic rhinometry and rhinomanometry in the evaluation of nasal patency of patients with nasal septal deviation. *American journal of rhinology*, 12(5):345–352, 1998.

[180] OK Kahveci, MC Miman, A Yucel, F Yucedag, E Okur, and A Altuntas. The efficiency of nose obstruction symptom evaluation (nose) scale on patients with nasal septal deviation. *Auris Nasus Larynx*, 39(3):275–279, 2012.

[181] P Dastidar, T Heinonen, J Numminen, M Rautiainen, and E Laasonen. Semiautomatic segmentation of computed tomographic images in volumetric estimation of nasal airway. *European archives of oto-rhino-laryngology*, 256(4):192–198, 1999.

[182] LA Pimenta, GL de Rezende Barbosa, H Pretti, O Emodi, J van Aalst, P E Rossouw, D A Tyndall, and AF Drake. Three-dimensional evaluation of nasopharyngeal airways of unilateral cleft lip and palate patients. *The Laryngoscope*, 125(3):736–739, 2015.

[183] K Tingelhoff, AI Moral, ME Kunkel, M Rilk, I Wagner, KWG Eichhorn, FM Wahl, and F Bootz. Comparison between manual and semi-automatic segmentation of nasal cavity and paranasal sinuses from ct images. In *Engineering in Medicine and Biology Society, 2007. EMBS 2007. 29th Annual International Conference of the IEEE*, pages 5505–5508. IEEE, 2007.

[184] G Di Carlo, A Polimeni, B Melsen, and PM Cattaneo. The relationship between upper airways and craniofacial morphology studied in 3d. a cbct study. *Orthodontics & craniofacial research*, 18(1):1–11, 2015.

Published works

Full Paper

Published

1. M. Codari, M. Caffini, G.M. Tartaglia, C. Sforza, G. Baselli. Computer-aided 3D cephalometric landmark annotation for CBCT data. International Journal of Computer Assisted Radiology and Surgery, 1-9, 2016;

2. M. Codari; M. Zago, G.A. Guidugli, V.Pucciarelli, G.M. Tartaglia, F. Ottaviani, S. Righini, C. Sforza. The nasal septum deviation index (NSDI) based on CBCT data. Dentomaxillofacial Radiology, 45(2):20150327, 2015;

3. C. Sforza, C. Dolci, D.M. Gibelli, M. Codari, V.Pucciarelli, V.F. Ferrario, F. Elamin. Age- and sex-related changes in the normal soft tissue profile of Northern Sudanese persons: a cross-sectional study. The British Journal of Oral & Maxillofacial Surgery, 54(2):192-197, 2015;

4. G.M. Tartaglia, C. Maiorana, M. Gallo, M. Codari, C. Sforza. Implant Dentistry Implant-supported immediately loaded full-arch rehabilitations: Comparison of resin and zirconia clinical outcomes in a 5 year retrospective follow-up study, 25(1):74-82, 2015;

5. M. Codari, V. Pucciarelli, D.G. Tommasi, C. Sforza. Validation of a technique for integration of a digital dental model into stereophotogrammetric images of the face using cone-beam computed tomographic data. The British Journal of Oral & Maxillofacial Surgery,4(5):584-586,2015;

6. M. Codari, V. Pucciarelli, L. Pisoni, C. Sforza. Laser Scanner versus Stereophotogrammetry: comparison of area measurements on nasal plaster casts. The British Journal of Oral & Maxillofacial Surgery, 53(8):769-770, 2015

7. D.M. Gibelli, M. Codari, R. Rosati, C. Dolci, G.M. Tartaglia, C. Cattaneo, C. Sforza. Sexual dimorphism of lips: aestetics and sex. Aesthetic Plastic Surgery, 39(5):771-776, 2015;

8. C. Sforza, L. Pisoni, M. Codari, M. Gandolfini, A. Di Blasio, V.F. Ferrario. Soft tissue facial asymmetry in subjects with Moebius syndrome: bilateral vs. unilateral palsy. Italian Journal of Maxillo-Facial Surgery 25(1):1-7, 2014;

9. R. Rosati, M. Codari, F. Maffessanti, C. Dolci, V.F. Ferrario, C. Sforza. The Labial Aging Process: A Surface Analysis-Based Three-Dimensional Evaluationt, Aesthetic Plastic Surgery, 38(1):236-241, 2014;

10. M. Zago, M. Codari, M. Grilli, B. Giuseppe, N. Lovecchio, C. Sforza. Determinants of the 180-turn with the ball in sub-elite youth soccer players. Sports Biomechanics, 15(2):234-244, 2016.

11. M. Zago, M. Codari, F.M. Iaia, C. Sforza. Multi-segmental movements as a function of experience in karate. Journal of Sports Sciences, 1-8, 2016;

In Press

12. V. Pucciarelli, F. Tarabbia, M. Codari, G.A. Guidugli, G. Colletti, G. Dell'Aversana Orabona, B. Bianchi, C. Sforza, F. Biglioli. Stereophotogrammetric evaluation of labial symmetry after surgical treatment of a lymphatic malformation. Journal of Craniofacial Surgery, *in Press*

13. M. Codari, V. Pucciarelli; F. Stangoni, M. Zago, F. Tarabbia, F. Biglioli, C. Sforza. Facial thirds-based evaluation of facial asymmetry using stereophotogrammetric devices: application on facial palsy subjects. Journal of Cranio-Maxillofacial Surgery, *in Press.*

14. M. EzEldeen, A. Stratis, W. Coucke; M. Codari, C. Politis, R Jacobs. As low dose as sufficient quality: optimization of CBCT scanning protocol for tooth autotransplantation planning and follow-up in children. . Journal of Endodontics, *in Press*

15. V. Pucciarelli, S. Bertoli, M. Codari, P. Veggiotti, A. Battezzati , C. Sforza. Facial evaluation in holoprosencephaly: A three-dimensional study. Journal of Craniofacial Surgery, *in Press*

Conference Paper

Published

1. M. Codari, V. Pucciarelli, F. Stangoni, GA. Guidugli, GM. Tartaglia, C Sforza. "Assessment of facial asymmetry using stereophotogrammetry". Italian Journal of Anatomy and Embryology, , 2016;

2. L. Pisoni, M. Codari, S. Galli, V. Pucciarelli, FME. Rusconi, GM. Tartaglia, C. Dolci. Comparison of direct linear measurements on dental plaster cast and digital measurements obtained from laser scanner and Cone-Beam CT dental models. Italian Journal of Anatomy and Embryology,, 2016;

3. C. Dolci, V. Pucciarelli, M. Codari, F.M.E. Rusconi, S. Marelli, G. Trifiro', A. Pini. The face in Marfan Syndrome: a 3D Morphometric Analysis. Italian Journal of Anatomy and Embryology,, 2016;

4. M. Codari, L. Ferreira Pinheiro Nicolielo, K. de Faria Vasconcelos, R. Jacobs, F. Haiter Neto, In-vitro objective evaluation of the impact of metal artifact in metal segmentation and background image quality with different CBCT devices, materials and field of views, Proceedings of ECDMFR, 2016;

5. K. de Faria Vasconcelos, L. Ferreira Pinheiro Nicolielo, M. Codari, R. Jacobs, F. Haiter Neto, The performance of artifact reduction algorithm in CBCT images: a quantitative study, Proceedings of ECDMFR, 2016;

6. L. Ferreira Pinheiro Nicolielo, J. Van Dessel, M. Codari, A. Kakar, A. De Mol, E. Shaheen, C. Politis, R. Jacobs. A novel imaging approach to follow-up of condylar remodeling following bimaxillary surgery, Proceedings of ECDMFR, 2016;

7. K. Khouri, I. Ioan, D. Casolino, M. Codari, M. Trimboli, F. Sardanelli. "Relazione tra parametri di perfusione del carcinoma mammario invasivo (CMI) alla RM mammaria dinamica e biomarker di aggressivitÃ ". Proceedings of the SIRM Congress, 2016;

8. M. Codari, L. Ferreira Pinheiro Nicolielo, J. Van Dessel, M. Caffini, G. Baselli, C. Politis, C. Sforza, R. Jacobs. Automatic segmentation for condylar morphometric analysis in CT and CBCT data: an in-vitro validation. International Journal of Computer Assisted Radiology and Surgery, 11(S1):S146-S147, 2016;

9. V. Pucciarelli, L. Pisoni, M. De Menezes, A.M. Ceron-Zapata, A.M. Lopez-Palacio, M. Codari, C. Sforza. Palatal Volume Changes in Unilateral Cleft Lip and Palate Paediatric Patients. Proceedings of the 6th International Conference on 3D Body Scanning Technologies, 139-146, 2015;

10. V. Pucciarelli, M. Codari, C. Invernizzi, S. Bertoli, A. Battezzati, R. De Amicis, V. De Giorgis, P. Veggiotti, C. Sforza. Three-Dimensional Craniofacial Features of Glut1 Deficiency Syndrome Patients. Proceedings of the 6th International Conference on 3D Body Scanning Technologies, 61-67, 2015.

11. C. Dolci, V. Pucciarelli, M. Codari, D.M. Gibelli, S. Marelli, G. Trifiro', A. Pini, C. Sforza. 3D Craniofacial Morphometric Analysis of Young Subjects with Marfan Syndrome: A Preliminary Report. Proceedings of the 6th International Conference on 3D Body Scanning Technologies 54-60, 2015;

12. L. Pisoni, M. Codari, M. De Menezes, A.M. Cerib-Zapata, A.M Lopez-Palacio, C. Dolci. Longitudinal analysis of palatal volume in unilateral cleft and palate children. Italian journal of anatomy and embryology, 120(Suppl.1):79-79, 2015;

13. V. Pucciarelli, M. Codari, A. Girardi, C. Gustinetti, G.M. Tartaglia, M. Caffini, G. Baselli, C. Sforza. Evaluation of accuracy and reproducibility in manual point picking during 3D cephalometry on CBCT data. Italian journal of anatomy and embryology, 120(Suppl.1):84-84, 2015.

14. M. Codari, M. Caffini, L. Rizzo, G. Rocco, G. Baselli, C. Sforza. Validation of an automatic hard tissue segmentation algorithm for cone beam CT data. Proceedings of the International 37th annual conference of IEEE Engineering in Medicine and Biology Society, 2015;

15. M.Codari, M.Caffini,G.M. Tartaglia, C.Sforza, G.Baselli. Automatic Hard Tissue Segmentation And Metal Artifacts Reduction In Dental CBCT DataInternational Journal of Computer Aided Radiology and Surgery 10(S1):300-301, 2015;

16. M. Codari, M.Caffini, G. Baselli, G.M. Tartaglia, V. Pucciarelli, M. Zago, C. Sforza. Evaluation of different registration approaches in 3D cephalometric landmark estimation. Italian journal of anatomy and embryology, 119(S1):49-49, 2014;

17. M. Codari, G.A. Guidugli, G.M. Tartaglia, V. Pucciarelli, L. Pisoni, V.F. Ferrario. Morphometric parameters for nasal septum deviation identification in CBCT data. Italian journal of anatomy and embryology, 119:(S1):48-48, 2014;

18. D.G. Tommasi, D. Dervishi, F. Argenta, M. Codari, G.M. Tartaglia, C. Dolci. Registration of dental arch models in 3D facial volumes: an alternative to CBCT acquisitions. Italian journal of anatomy and embryology, 118:(S2):187-187, 2013;

In Press

19. C. Dolci, V. Pucciarelli, M. Codari, S. Marelli, G.Trifiro', A.Pini, C.Sforza. 3D Morphometric Evaluation of Craniofacial Features in Adult Subjects With Marfan Syndrome. Proceedings of the 7th International Conference and Exhibition on 3D body scanning technologies, 2016, *In Press*;

20. V. Pucciarelli, DM. Gibelli, M.Codari, F.M.E. Rusconi, A. Cappella, C. Cattaneo, C.Sforza. Laser scanner versus stereophotogrammetry: a three-dimensional quantitative approach for morphological analysis of pubic symphysis. Proceedings of the 7th International Conference and Exhibition on 3D body scanning technologies, 2016, *In Press*;

CURRICULUM VITAE

Marina Codari

Curriculum Vitae

Via Don Bosco 31
Milano, Italia 20139
+39 327 4724263
marina.codari@gmail.com
DoB: 27 December 1987

EDUCATION

January 2017 – January 2014 **PhD Candidate in Integrated Biomedical Research**, *Department of Biomedical Sciences for Health - University of Milan - Via Mangiagalli 31, 20133 Milano (MI),Italy*,
Main Topic: Image processing for automatic feature extraction: application to the oro-maxillo-facial region, Main research topics: image segmentation, registration and arifact reduction in CBCT data for maxillofacial applications. During the PhD I worked on several project that required cooperation with Companies, Medical Doctors, Engineers and Dentists.

April 2016 – October 2015 **Visiting PhD Student**, *KU Leuven*, Omfs Impath Research Group, Department of Imaging and Pathology, Faculty of Medicine, University of Leuven and Department of Oral and Maxillofacial Surgery, University Hospitals Leuven, Leuven, Belgium.

January 2014 – September 2013 **Visiting graduate student**, ***University of Milan*** , *Department of Biomedical Sciences for Health, Laboratory of Functional Anatomy of the Stomatognathic Apparatus*, Milano, Italy, Implementation of a semi-automatic algorithm for 3D cephalometric analysis. 3D labial morphology analysis. Suppor for teaching activities for a group Medicine and Dentistry students.

July 2013 – February 2010 **Master's degree, Bioengineering and Biomedical Engineering**, ***Politecnico di Milano***, **Italy**,
Specialization in Biomedical Electronics field, with particular attention to: Biomedical imaging, Electronic devices for medical instruments, Computer aided surgery systems, Motion analysis and virtualization techniques, Biological signal analysis. Master Thesis: Semi-automatic estimate of cephalometric landmarks in three-dimensional Cone Beam CT. 105/110

February 2010 – October 2006 **Bachelor's degree, Bioengineering and Biomedical Engineering**, ***Politecnico di Milano***, **Italy**, Thesis: Definition of a quantitative method for lip curvature analisys.

TRAINING AND COURSES

February 2016 **EADMFR Junior Meeting**, *Lublin, Poland*, Selected Partecipant.
Lessons on: EBR tasks, CBCT, US and MRI imaging for maxillofacial applications

January 2016 **Amira training Course**, *KU Leuven, Leuven, Belgium*.

February 2015 **Sistematic, topographic and functional head and neck anatomy**, *Professor Chiarella Sforza*, Università degli studi di Milano.

October 2014 **Data Analysis**, *Professor Andrea Caumo*, Università degli studi di Milano.

May 2014 **Applied statistic**, *Professor Alberto Porta*, Università degli studi di Milano, 30/30 cum Laude.

PUBLICATIONS

Full Articles — I'm author of 13 full articles published on peer-reviewed international Journals, ORCID ID: http://orcid.org/0000-0001-8475-2071

Conference Paper — I'm author of 20 conference paper presented in both national (8) and intrnational (12) conferences as oral presentation or posters.

EXPERIENCE

January 2014 September 2013 — **R&D Engineer**, *Sidoti e Tartaglia s.r.l.* , Via Martiri della Libertà 58, 20090 , Segrate (MI),Italy.
Elaboration of CBCT images for dental application and CAD/CAM applications for guided implant surgery

May 2009 January 2009 — **Internship - Morphological analysis of the human face**, *Laboratory of Functional Anatomy of the Stomatognathic Apparatus, Università degli Studi di Milano, Department of Human Morphology - Città Studi, Milano, Italy.*,
3D study of facial morphology using data obtained with stereophotogrammetric and laser-scanning imaging systems.

October 2009 January 2009 — **Management Control**, *Nuovoprogramma s.a.s., via Conciliazione 16, 20077 Melegnano (MI), Italy*,
Control and monitoring of the project progresses in relation to established budgets and timetables for an IT company.

AWARDS

June 2016 — **Research Award**, *Oral Presentation - 2nd Prize*, 15th European Congress of DentoMaxillo-FacialRadiology , Cardiff, Wales (UK).
In-vitro quantification of the impact of artifacts on metal segmentation and image quality with varying CBCTs, materials and fbbield of views

September 2010 — **Rotary Youth Leadership Awards**, *Scholarship winner*, Selected participant of the Personal Leadership course.

SKILLS

Certifications

Italian Engineering profession Certification

Association

IEEE Engineering in Medicine and Biology Society, European Academy of DentomaxillofacialRadiology

Reviewer for

Journals: Clinical Oral Investigation,European Journal of Oral Implantology, Journal of Anatomy, International Journal of Computer Assisted radiology and surgery and Medical & Biological Engineering & Computing

Technical

Languages — MATLAB, C, C ++,VHDL, LABVIEW, MEVISLAB

Softwares — OSIRIX, ITK-SNAP, MIMICS, MEVISLAB, ECDL, RHINOCEROS, LATEX, KYPLOT, OFFICE, AMIRA

Systems — Windows XP, Vista, 7, 8, Mac OSX

Linguistic

Italian — mother tongue

English level C1, TOEFL iBT Test (2015)

VOLUNTEER EXPERIENCES AND CAUSES

Italian Red Cross

Present – May 2008 Member as Voluntary of First Aid. AED, First Aid, DAE and ECG certified.

Rotaract International

December 2014 – May 2009 Member of Rotaract association.
Vice President (2010-2011), then President (2011-2012) and Past President and Sergeant-at-arms (2012 ? 2013) of the RTC San Giuliano Milanese. Winner of the RYLA (Rotary Youth Leadership Awards) scholarship in 2010. Winner of the Eubosia ANT prize ? IV Edition.

I authorise the processing of my personal data.

APPENDIX

Published works included in this Doctoral Thesis

The final publications presented in this section are available at:

- British Institute of Radiology via *http://dx.doi.org/10.1259/dmfr.20150327*
- Elsevier via *http://dx.doi.org/10.1016/j.bjoms.2016.01.019*
- Elsevier via *http://dx.doi.org/10.1016/j.jcms.2016.11.003*
- Springer via *http://dx.doi.org/10.1007/s11548-016-1453-9*

Dentomaxillofacial Radiology (2016) 45, 20150327
© 2015 The Authors. Published by the British Institute of Radiology
birpublications.org/dmfr

RESEARCH ARTICLE

The nasal septum deviation index (NSDI) based on CBCT data

[1]Marina Codari, [1]Matteo Zago, [1,2]Giulia A Guidugli, [1]Valentina Pucciarelli, [1]Gianluca M Tartaglia, [2,3]Francesco Ottaviani, [3]Stefano Righini and [1]Chiarella Sforza

[1]*Functional Anatomy Research Center (FARC), Laboratorio di Anatomia Funzionale, dell'Apparato Stomatognatico, Dipartimento di Scienze Biomediche per la Salute, Facoltà di Medicina e Chirurgia, Università degli Studi di Milano, Milano, Italy;* [2]*Dipartimento di Scienze Cliniche e di Comunità, Facoltà di Medicina e Chirurgia, Università degli Studi di Milano, Milano, Italy;* [3]*Ospedale San Giuseppe, Milano, Italy*

Objective: To assess whether three-dimensional morphometric parameters could be useful in nasal septal deviation (NSD) diagnosis and, secondarily, whether CBCT could be considered an adequate imaging technique for the proposed task.
Methods: We analysed images of 46 subjects who underwent CBCT for reasons not related to this study. Two experienced operators divided all the images into healthy and NSD subjects. Subsequently, the images were segmented using ITK Snap in order to obtain the three-dimensional model of the nasal airways and compute four morphological parameters: septal deviation angle (SDA), percentage of volume difference between right and left side of the nasal airways, nasal airway total volume and a new synthetic septal deviation index (SDI). Principal component analysis (PCA) was used to unveil relationships between each variable and the global nasal airway variability.
Results: Differences between the groups were found in SDA ($p < 0.001$), in volume percentage difference ($p < 0.05$) and in SDI ($p < 0.001$). PCA showed high correlation between the SDI and the first principal component (0.97, $p < 0.001$).
Conclusions: Among the analysed parameters, SDI seemed to be the most suitable for the quantitative assessment of NSD, and CBCT allowed accurate assessment of airway morphology.
Dentomaxillofacial Radiology (2016) **45**, 20150327. doi: 10.1259/dmfr.20150327

Cite this article as: Codari M, Zago M, Guidugli GA, Pucciarelli V, Tartaglia GM, Ottaviani F, et al. The nasal septum deviation index (NSDI) based on CBCT data. *Dentomaxillofac Radiol* 2016; **45**: 20150327.

Keywords: nasal septum; CBCT; image interpretation; Computer-assisted

Introduction

Nasal septal deviation (NSD) consists in a misalignment of nasal septum from the midline, which leads to respiratory disease caused by volume reduction in the nasal cavity. Together with NSD, a hypertrophy of the turbinates, opposed to septal convexity, is often noticed.[1,2]

Diagnostic investigations currently used for this pathology are anterior rhinoscopy, endoscopy, multislice CT and MR, which allow a good evaluation of the entity and position of NSD.[3–8] In particular, pre-operative CT scan of the paranasal sinuses is often performed before septoplasty, in order to evaluate nasal anatomy, to find concomitant sinonasal pathologies and to reduce surgical failure.[8–10] Despite the fact that pre-operative CT scan of the paranasal sinuses can be recommended in case of obstructive middle turbinate hypertrophy, impossibility to evaluate the middle meatus and the posterior nasal cavity or in patients with chronic sinusitis, the high radiation dose and costs do not allow its usage routinely in patients undergoing septoplasty.[10]

In the last decades, CBCT has been emerging, and now, it is widely used in dentistry, thanks to its high image resolution, low radiation dose and low costs.[11–13] Currently, its clinical use in other medical fields is limited and not widespread because of minor soft-tissue contrast;

Correspondence to: Professor Chiarella Sforza. E-mail: chiarella.sforza@unimi.it
Received 8 October 2015; revised 12 December 2015; accepted 16 December 2015

however, many studies confirm that CBCT could be a valid support in otolaryngology also.[14–16]

Given that the evaluation of NSD in CT images is currently mainly based on subjective clinic and radiologic analyses, many studies are trying to find homogeneous and standard evaluation criteria based on the morphometric analysis of the nasal airways.[1,17–19]

Among them, three-dimensional segmentation is currently used for morphological evaluation of the upper airways, mainly to assess obstructive sleep apnoea, traumas and congenital malformations.[20–22]

In the present study, we segmented several CBCT images to create three-dimensional models of the nasal airways, which were used to calculate three-dimensional parameters that describe their morphology. The aim of the proposed study was to understand if CBCT could be considered an adequate imaging technique for the proposed task and if such parameters could be useful in NSD quantification before surgery.

Methods and materials

For this study, 46 CBCT images were selected from the archives of SST Dentofacial Clinic (Segrate, MI, Italy) and analysed retrospectively. Subjects who had a history of previous nasal surgery or other abnormality besides NSD were excluded.

Since the images were selected from a dental database, no information about subject otolaryngological diagnosis was available. Therefore, two experienced operators divided the selected images into deviated (NSD group) or non-deviated nasal septum (control group). Both operators were otolaryngologists with more than 3 years' experience in NSD treatments. The classification of the images into NSD or control subjects was randomized and double blinded; it was performed by each operator according to the severity of septum deviation in relation to the median line and to the eventual reduction of the air volume in the nasal cavity.

An excellent level of agreement was found between operators, with an unweighted Cohen κ equal to 0.86. Only in three cases, the operators classified the same subject into different categories; so, these data were excluded from the data set. The final data set was composed of 15 control subjects and 28 NSD subjects.

All CBCT scans were acquired by the same scanner (WhiteFox; ACTEON, Mérignac, France). The device was operated at 6–10 mA (pulse mode) and 105 kV using an X-ray generator with fixed anode and 0.5-mm nominal focal spot size. The selected volume images are composed of isotropic 0.3-mm voxels.

To evaluate the severity of septal deviation, we assessed the difference between groups in septal deviation angle (SDA), calculated as proposed by Orhan et al.[23] The measurements of the angle between the maxillary spine, the crista galli and the apex of the septal deviation were taken using the freeware OsiriX (Pixmeo, Geneva, Switzerland).

Subsequently, we evaluated the percentage difference between the volume of the upper airways in the right and left side of the nose in the same samples. Volume segmentation from the CBCT files was performed using the freeware ITK Snap, which allows the user to accurately segment and calculate volumes of upper airways.[16,24] For all images, a first automatic segmentation was subsequently refined manually.

At first, in order to obtain an accurate and reproducible segmentation of the nasal portion of the upper airway, a volume of interest (VOI) was delimited for each side of the upper airways. Each VOI was defined as a box bounded anterosuperiorly by the rhinion, the most inferior and anterior point between the nasal bones, inferiorly from the lower limit of the hard palate, posteriorly from the Posterior Nasal Spine Landmark and laterally by the lateral margins of the nasal cavity, as shown in Figure 1.

Once VOIs were selected, we proceeded with the segmentation of the nasal upper airway using the active contour segmentation option. Moreover, to avoid the inclusion of different portions of the maxillary sinuses in different subjects, they were segmented separately and their volume was subtracted from the nasal airway volume. In Figure 2, an example of the outcome of the segmentation process is shown.

The repeatability in the selection and segmentation of the VOI and in deviation angle measurements was verified on a subsample of 10 CBCT. Statistical analyses on measurement repeatability were performed by calculating Student's *t*-test and Dahlberg's formula.[25]

After the segmentation, the volumes of each side of the upper airway were measured, and then their relative volume percentage difference (VPD) was calculated as:

$$\mathrm{VPD}=\frac{|V_r - V_l|}{V_r + V_l}\cdot 100$$

where V_r and V_l, both expressed in cm^3, represent the volumes of the right and left VOIs defined previously.

Finally, a new index, named septal deviation index (SDI), was introduced. The SDI was designed to summarize information about the angle of septal deviation, volume difference between right and left side of the nose and total volume of the nasal airway and was calculated as:

$$\mathrm{SDI}=\frac{(\mathrm{SDA}+1)\cdot(\mathrm{VPD}+1)}{V_T}$$

where SDA is expressed in degrees, VPD is the adimensional volumetric percentage of difference and V_T represents the total volume of nasal airways ($V_T = V_r + V_l$). Both SDA and VPD were increased by a unitary factor to prevent SDI from tending to zero if only one of these factors is null.

The statistical analysis was performed using the MATLAB® statistic toolbox (MathWorks®, Natick, MA). Student's *t*-tests and $\chi 2$ tests were performed to compare different morphometric parameters in healthy and NSD subjects. Statistical significance was set at

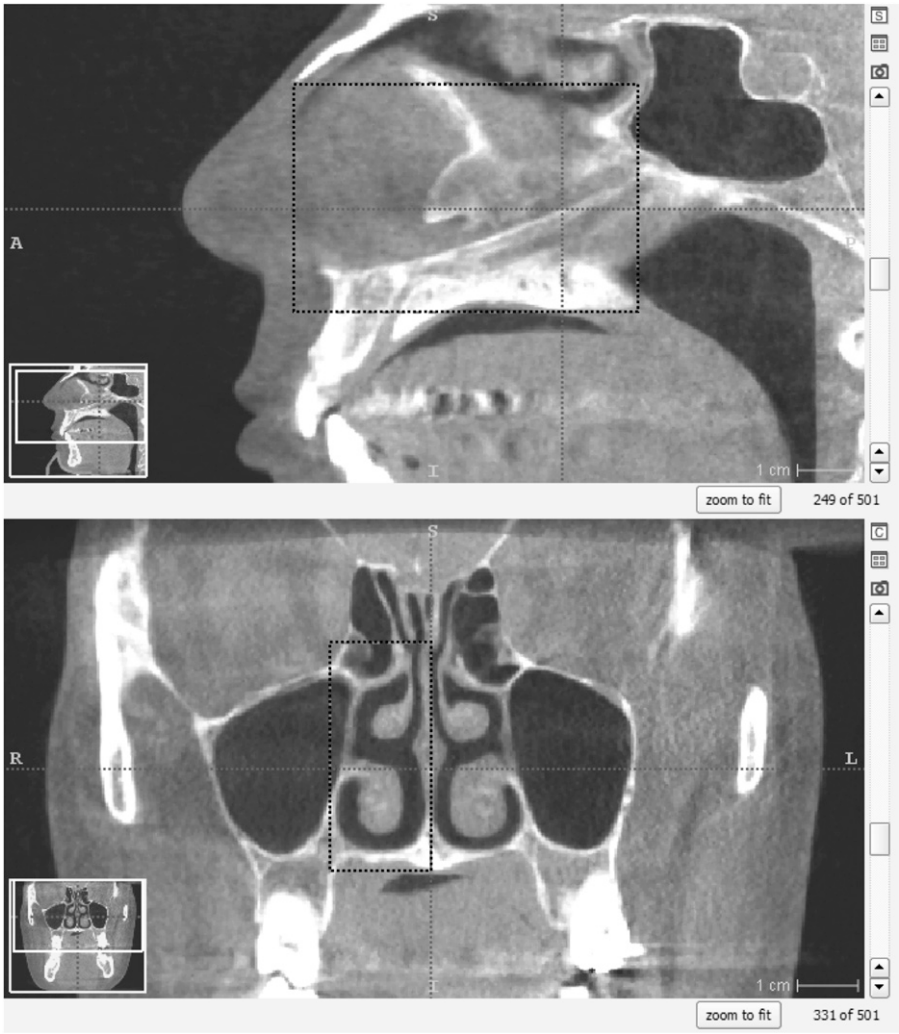

Figure 1 Example of a selected volume of interest for the right side of the nasal airways using ITK Snap. The bounding box is highlighted using dashed rectangles in sagittal (top) and frontal (bottom) views.

$p < 0.05$. Furthermore, since the evaluated morphometric variables are related to each other, we used principal component analysis (PCA) to transform all the morphological data into a set of uncorrelated variables called principal components.[26] According to Kaiser's rule, we retained the components whose eigenvalues were larger than 1.[27] PCA was performed on the correlation matrix of the normalized data set.

Pearson's correlation coefficients retained principal components, and all calculated parameters were also computed. In this way, PCA is used to unveil the relationship between each variable and the global nasal airway variability.[28]

Results

The analysed groups were composed of 15 control subjects (7 males, 9 females; average age 46 ± 15 years) and 28 NSD subjects (15 males, 13 females; average age 48 ± 15 years). No significant difference was found in age (Student's t) and sex composition (χ^2) between groups ($p > 0.05$).

Repeatability analysis showed no significant differences for both SDA and volume measurements ($p > 0.05$). In particular, random errors explained 0.77% of sample variance for angle measurements and 0.99% for volume measurements.

Values of SDA, VPD and SDI were significantly higher in NSD subjects compared with healthy subjects. Descriptive statistics of these parameters are summarized in Table 1.

In particular, intergroup analysis showed statistically significant differences in SDA ($p < 0.001$), in VPD ($p < 0.05$) and in SDI ($p < 0.001$) between healthy and NSD subjects. No significant difference was found in V_T between groups ($p > 0.05$).

Only the first component (PC1) and the second component (PC2) resulting from the PCA were retained. These

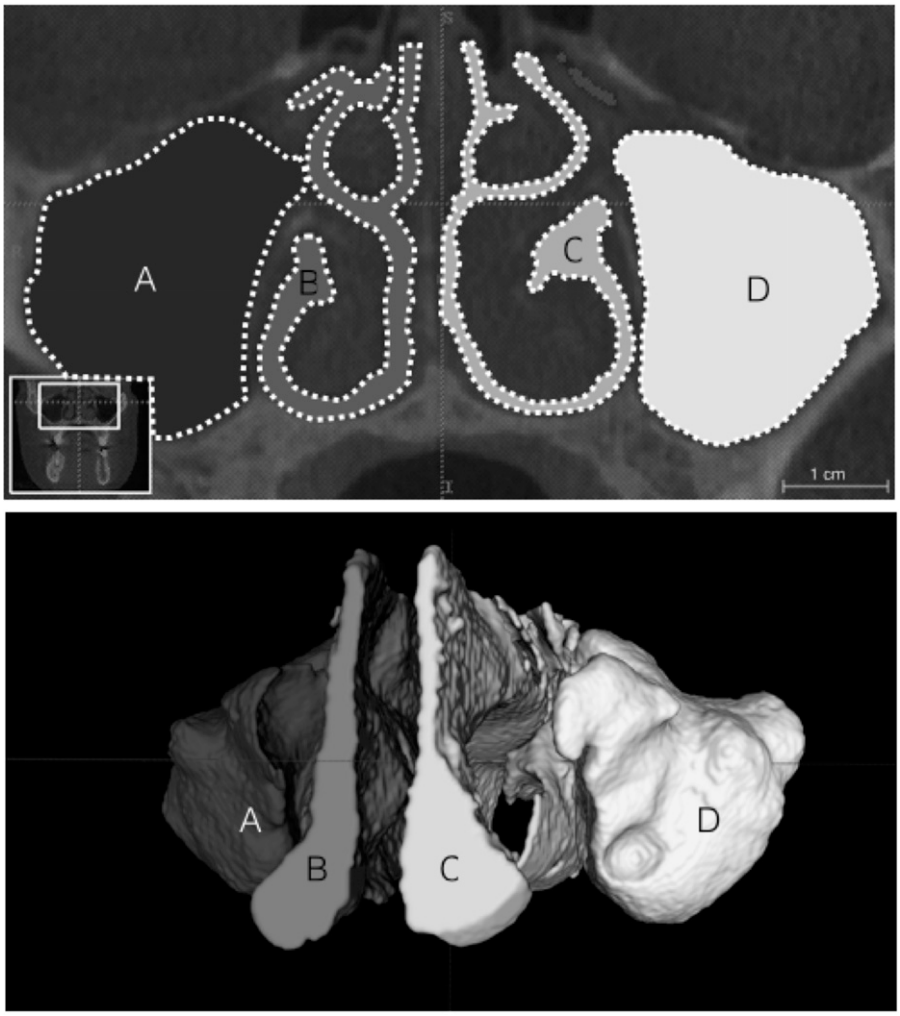

Figure 2 Example of segmentation of the right (B) and left (C) side of the nasal airway and of the left and right maxillary sinuses (A and D, respectively). In the top image, the segmentation outcomes are represented in a posterior coronal CBCT slice. In the bottom image, an example of the three-dimensional volumes segmented in the proposed study is depicted.

two components explained 86.6% of the sample variance. For PC1, higher values of correlation coefficient were found for SDI (0.97, $p < 0.001$) and for standard deviation (0.89, $p < 0.001$); on the other hand, PC2 seemed to be more correlated with V_T (0.94, $p < 0.001$) than the other morphological variables. In Table 2, all the calculated correlation coefficients are detailed.

Discussion

In otorhinolaryngology, NSD is one of the most frequent diagnoses, and it is generally based on the evaluation of patient symptoms and on anterior rhinoscopic outcomes.[6] This clinical analysis is accompanied by quantitative diagnostic methods used to demonstrate the septal deviation.[7,8,29] In particular, cross-sectional images allow the correlation of patient symptoms to the airway anatomy of both the anterior and posterior nasal cavity before surgery.[10,30]

In this study, we analysed 46 CBCT images belonging to dental patients whose otolaryngological diagnosis is

Table 1 Septal deviation angle (SDA), volume percentage difference (VPD), total volume (V_T) and septal deviation index (SDI) between healthy and nasal septal deviation (NSD) group

Morphological parameters	*Groups*	*Mean*	*SD*	*Min*	*Max*
SDA (°)	Control	9.5	2.5	5.9	14.3
	NSD	17.3	5.5	10.0	36.0
VPD (%)	Control	5.5	4.9	0.1	16.4
	NSD	13.6	11.6	0.39	54.7
V_T (cm^3)	Control	18.1	4.7	12.2	30.5
	NSD	16.5	3.1	12.1	23.1
SDI (°/cm^3)	Control	3.8	3.2	0.6	12.0
	NSD	16.5	14.3	1.3	62.9

SD, standard deviation.

Table 2 Eigenvalues and explained variance of the retained principal components and their corresponding Pearson's correlation coefficients for the analysed morphological variables

		Pearson's correlation coefficient			
Principal component	*Explained variance (%)*	*SDA*	*VPD*	V_T	*SDI*
PC1	57.0	0.75	0.89	0.12	0.96
PC2	29.6	−0.40	0.19	0.94	0.12

The analysed parameters are: septal deviation angle (SDA), septal deviation index (SDI), volume percentage difference (VPD) and total volume (V_T). PC1, first component; PC2, second component.

unknown, to assess whether there was a significant difference in four morphological parameters (SDA, VPD, VT and SNI) between NSD and healthy subjects. This analysis was performed in order to assess whether quantitative and evidence-based morphometric parameters may be useful in NSD diagnosis or septoplasty pre-operative planning and to test the validity of a proposed synthetic index summarizing these parameters.

In the present investigation, two experienced operators divided all the images into control and NSD groups. An excellent level of agreement, with Cohen's $\kappa = 0.86$, was found, suggesting not only concordance between operators, but also adequacy of the CBCT images for the proposed task.

Regarding volumetric and angular measurement, the proposed method appears repeatable, since the measurement error was $<1\%$ of the sample variance for both measures.

At first, we evaluated the SDA, which is frequently used to assess the severity of NSD.[23,31,32] As expected, the results showed a significant difference between healthy and NSD subjects. Moreover, the high repeatability of SDA measurements demonstrated that CBCT scans could be used to evaluate the severity of NSD.

A significant difference between the groups was also found in the percentage of volume difference between the left and right side of the nasal airways. This value is independent of subject size and consequently of his/her airway dimension. Therefore, it can be a useful three-dimensional index to assess the balance of volume in the two different sides of the airways. In our study, we found higher values of VPD in NSD subjects, suggesting a paradoxical hypertrophy. Our results showed that SDA and VPD could characterize NSD subjects. For this reason, we decided to merge them into a single global parameter, SDI, which is directly proportional to them and indirectly proportional to the total volume of the nasal airways. This index has significantly higher values in NSD than in control subjects and appears to be a useful parameter for septal deviation quantification, since it takes into account various factors contributing to subject respiration. SDI is robust to the variation of only one parameter between SDA and VPD, which may separately contribute to the patient's breathing, and takes into account that septal deviations may create more or less discomfort to the subject depending on the size of his/her nasal airway. In particular, SDI can be a useful parameter because it is not a local descriptor of the nasal cavity, like SDA, but takes into account the three-dimensional morphology of the nasal cavity. Moreover, this index showed the highest correlation with PC1, which expresses 57.0% of the sample variability.

In multivariate analysis, only PC1 and PC2 were retained. PC1 highly correlates with all the morphological parameters that have significantly higher values in NSD subjects than in healthy subjects. This component is therefore more related to factors that identify NSD, rather than to the size of the airway.

On the contrary, PC2 (29.6% of explained variance) is highly related to the nasal airway size of the subject; so, it is less suited for representing the analysed sample. This is also evidenced by the non-significant difference in terms of V_T in the analysed groups.

From our findings it can be stated that SDA, VPD and SDI are morphological parameters that may help surgeons to better understand the patient's upper airway morphology, estimating the amount of the septal deviation and the air volume in each side of the nose. In particular, they may be a useful tool during the pre-operative assessment of the nasal airway, in order to enable the surgeon to find the optimal surgical intervention that will produce the best outcome.[33]

Although results are promising, a further validation of the proposed method is advised. In particular, the validation on a sample of CBCT images of patients with known otolaryngological diagnosis would allow correlating these quantitative parameters with the patient medical history, thus overcoming the limitations caused by the need to group the subjects only in accordance with radiologic examination and without clinical diagnosis.

Conclusions

In the present study, four three-dimensional morphological parameters were analysed to evaluate their usefulness in assessing the deviation of the nasal septum. Retrospectively selected CBCT images, which allowed accurate assessment of the morphology of the airways of the patient, reducing the dose of radiation and therefore its invasiveness, were used.

Among the analysed parameters, the proposed SDI seems to be the most suitable for the quantitative assessment of NSD, since it summarizes different morphometric factors. Further investigation shall expand the study to patients with clinically assessed alterations in respiratory function and nasal airway patency.

References

1. Orhan I, Aydın S, Ormeci T, Yılmaz F. A radiological analysis of inferior turbinate in patients with deviated nasal septum by using computed tomography. *Am J Rhinol Allergy* 2014; **28**: 68–72.doi: 10.2500/ajra.2014.28.4007
2. Egeli E, Demirci L, Yazýcý B, Harputluoglu U. Evaluation of the inferior turbinate in patients with deviated nasal septum by using computed tomography. *Laryngoscope* 2004; **114**: 113–17. doi: 10.1097/00005537-200401000-00020
3. Murrell GL. Components of the nasal examination. *Aesthet Surg J* 2013; **33**: 38–42. doi: 10.1177/1090820X12469626
4. Wuister AMH, Goto NA, Oostveen EJ, de Jong WU, van der Valk ES, Kaper NM, et al. Nasal endoscopy is recommended for diagnosing adults with c rhinosinusitis. *Otolaryngol Head Neck Surg* 2014; **150**: 359–64.
5. Karataş D, Yüksel F, Şentürk M, Doğan M. The contribution of computed tomography to nasal septoplasty. *J Craniofac Surg* 2013; **24**: 1549–51.
6. Mamikoglu B, Houser S, Akbar I, Ng B, Corey JP. Acoustic rhinometry and computed tomography scans for the diagnosis of nasal septal deviation, with clinical correlation. *Otolaryngol Head Neck Surg* 2000; **123**(1 Pt 1): 61–8. doi: 10.1067/mhn.2000.105255
7. Eren SB, Tugrul S, Dogan R, Ozucer B, Ozturan O. Objective and subjective evaluation of operation success in patients with nasal septal deviation based on septum type. *Am J Rhinol Allergy* 2014; **28**: 158–62. doi: 10.2500/ajra.2014.28.4080
8. Kahveci OK, Miman MC, Yucel A, Yucedag F, Okur E, Altuntas A. The efficiency of Nose Obstruction Symptom Evaluation (NOSE) scale on patients with nasal septal deviation. *Auris Nasus Larynx* 2012; **39**: 275–9. doi: 10.1016/j.anl.2011.08.006
9. Akoğlu E, Karazincir S, Balci A, Okuyucu Sş, Sumbas H, Dağli AŞ. Evaluation of the turbinate hypertrophy by computed tomography in patients with deviated nasal septum. *Otolaryngol Head Neck Surg* 2007; **136**: 380–4.
10. Günbey E, Günbey HP, Uygun S, Karabulut H, Cingi C. Is preoperative paranasal sinus computed tomography necessary for every patient undergoing septoplasty? *Int Forum Allergy Rhinol* 2015; **5**: 839–45. doi: 10.1002/alr.21545
11. De Vos W, Casselman J, Swennen GRJ. Cone-beam computerized tomography (CBCT) imaging of the oral and maxillofacial region: a systematic review of the literature. *Int J Oral Maxillofac Surg* 2009; **38**: 609–25. doi: 10.1016/j.ijom.2009.02.028
12. Miracle AC, Mukherji SK. Conebeam CT of the head and neck, part 2: clinical applications. *AJNR Am J Neuroradiol* 2009; **30**: 1285–92. doi: 10.3174/ajnr.A1654
13. Mischkowski RA, Scherer P, Ritter L, Neugebauer J, Keeve E, Zöller JE. Diagnostic quality of multiplanar reformations obtained with a newly developed cone beam device for maxillofacial imaging. *Dentomaxillofacial Radiol* 2008; **37**: 1–9.
14. Bui NL, Ong SH, Foong KWC. Automatic segmentation of the nasal cavity and paranasal sinuses from cone-beam CT images. *Int J Comput Assist Radiol Surg* 2015; **10**: 1269–77. doi: 10.1007/s11548-014-1134-5
15. Tso HH, Lee JS, Huang JC, Maki K, Hatcher D, Miller AJ. Evaluation of the human airway using cone-beam computerized tomography. *Oral Surg Oral Med Oral Pathol Oral Radiol Endod* 2009; **108**: 768–76. doi: 10.1016/j.tripleo.2009.05.026
16. Weissheimer A, Macedo de Menezes L, Sameshima GT, Enciso R, Pham J, Grauer D. Imaging software accuracy for 3-dimensional analysis of the upper airway. *Am J Orthod Dentofacial Orthop* 2012; **142**: 801–13. doi: 10.1016/j.ajodo.2012.07.015
17. Robinson RJ, Russo J, Doolittle RL. 3D airway reconstruction using visible human data set and human casts with comparison to morphometric data. *Anat Rec (Hoboken)* 2009; **292**: 1028–44. doi: 10.1002/ar.20898
18. Souza KR, Oltramari-Navarro PV, Navarro RDL, Conti AC, Almeida MR. Reliability of a method to conduct upper airway analysis in cone-beam computed tomography. *Braz Oral Res* 2013; **27**: 48–54.
19. Setlur J, Goyal P. Relationship between septal body size and septal deviation. *Am J Rhinol Allergy* 2011; **25**: 397–400. doi: 10.2500/ajra.2011.25.3671
20. Li L, Liu H, Cheng H, Han Y, Wang C, Chen Y, et al. CBCT Evaluation of the upper airway morphological changes in growing patients of class II division 1 malocclusion with mandibular retrusion using twin block appliance: a comparative research. *PLoS One* 2014; **9**: 1–7. doi: 10.1371/journal.pone.0094378
21. Furuhashi A, Yamada S, Shiomi T, Sasanabe R, Aoki Y, Yamada Y, et al. Effective three-dimensional evaluation analysis of upper airway form during oral appliance therapy in patients with obstructive sleep apnoea. *J Oral Rehabil* 2013; **40**: 582–9. doi: 10.1111/joor.12059
22. Salerno S, Gagliardo C, Vitabile S, Militello C, Tona GLA, Giuffrè M, et al. Semi-automatic volumetric segmentation of the upper airways in patients with pierre robin sequence. *Neuroradiol J* 2014; **27**: 487–94.
23. Orhan I, Ormeci T, Aydin S, Altin G, Urger E, Soylu E, et al. Morphometric analysis of the maxillary sinus in patients with nasal septum deviation. *Eur Arch Otorhinolaryngol* 2014; **271**: 3035–40. doi: 10.1007/s00405-013-2617-7
24. Yushkevich P, Piven J, Hazlett HC, Smith RG, Ho S, Gee JC, et al. User-guided 3D active contour segmentation of anatomical structures: significantly improved efficiency and reliability. *Neuroimage* 2006; **31**: 1116–28. doi: 10.1016/j.neuroimage.2006.01.015
25. Kamoen A, Dermaut L, Verbeeck R. The clinical significance of error measurement in the interpretation of treatment results. *Eur J Orthod* 2001; **23**: 569–78. doi: 10.1093/ejo/23.5.569
26. Burgel PR, Paillasseur JL, Caillaud D, Tillie-Leblond I, Chanez P, Escamilla R, et al. Clinical COPD phenotypes: a novel approach using principal component and cluster analyses. *Eur Respir J* 2010; **36**: 531–9. doi: 10.1183/09031936.00175109
27. Jolliffe I. *Principal component analysis*. 2nd ed. New York, NY: Springer; 2002.
28. Gouelle A, Mégrot F, Presedo A, Husson I, Yelnik A, Penneçot GF. The gait variability index: a new way to quantify fluctuation magnitude of spatiotemporal parameters during gait. *Gait Posture* 2013; **38**: 461–5. doi: 10.1016/j.gaitpost.2013.01.013
29. Szücs E, Clement PAR. Acoustic rhinometry and rhinomanometry in the evaluation of nasal patency of patients with nasal septal deviation. *Am J Rhinol* 1998; **12**: 345–52. doi: 10.2500/105065898780182507
30. Dastidar P, Heinonen T, Numminen J, Rautiainen M, Laasonen E. Semi-automatic segmentation of computed tomographic images in volumetric estimation of nasal airway. *Eur Arch Otorhinolaryngol* 1999; **256**: 192–8. doi: 10.1007/s004050050138
31. Orlandi RR. A systematic analysis of septal deviation associated with rhinosinusitis. *Laryngoscope* 2010; **120**: 1687–95. doi: 10.1002/lary.20992
32. Lee DC, Shin JH, Kim SW, Kim SW, Kim BG, Kang JM, et al. Anatomical analysis of nasal obstruction: nasal cavity of patients complaining of stuffy nose. *Laryngoscope* 2013; **123**: 1381–4. doi: 10.1002/lary.23841
33. Rhee JS, Cannon DE, Frank DO, Kimbell JS. Role of virtual surgery in preoperative planning. *Arch Facial Plast Surg* 2012; **14**: 354–9. doi: 10.1001/archfacial.2012.182

Available online at www.sciencedirect.com

SciVerse ScienceDirect

British Journal of Oral and Maxillofacial Surgery 54 (2016) 584–586

BRITISH Journal of Oral and Maxillofacial Surgery

www.bjoms.com

Short communication

Validation of a technique for integration of a digital dental model into stereophotogrammetric images of the face using cone-beam computed tomographic data

Marina Codari, Valentina Pucciarelli, Davide G. Tommasi [1], Chiarella Sforza *

Functional Anatomy Research Center (FARC), Laboratorio di Anatomia Funzionale dell'Apparato Stomatognatico (LAFAS), Dipartimento di Scienze Biomediche per la Salute, Facoltà di Medicina e Chirurgia, Università degli Studi di Milano, Italy

Accepted 14 January 2016
Available online 3 February 2016

Abstract

We wanted to find and validate a new way to visualise patients' faces and their dental arches non-invasively. The stereophotogrammetric images of the faces and the digitised dental casts of seven healthy subjects were analysed. Point-based and surface-based recording techniques matched the facial image with those of the mandibular and maxillary dental arches in their relative positions. The cone-beam computed tomographic (CT) images of the same subjects were analysed retrospectively. Twenty-eight dentofacial distances were obtained on cone-beam CT images and on the recorded facial and dental surfaces. The median (IQR) distances of more than 96% of the measurements did not differ significantly.
© 2016 The British Association of Oral and Maxillofacial Surgeons. Published by Elsevier Ltd. All rights reserved.

Keywords: Stereophotogrammetry; Laser scanner; Dental arches; Face

Introduction

Digital technology and three-dimensional images are widely used in dentistry, making dental practices and research contexts into virtual-based processes.[1,2] Three-dimensional images of the face, skull, and dentition can be acquired using different imaging techniques. In particular, stereophotogrammetry and laser scanners allow us to acquire images of the face and the dental arches separately non-invasively, making them suitable for use in children and for longitudinal evaluation of outcomes of treatment.[3] In this context, we wanted to define and validate a technique that allows us to integrate information about facial soft tissues and the teeth non-invasively.

Patients and methods

The digitised dental plaster casts and the facial stereophotogrammetric images of seven subjects who had just had cone-beam computed tomography (CT) for clinical reasons were recorded and analysed. Cone-beam CT images of the same subjects were analysed retrospectively to validate the method. All study procedures were non-invasive, and done according to the Declaration of Helsinki. All subjects gave their written consent.

For each subject both maxillary and mandibular dental casts were obtained and digitised using a laser scanner (Dental Wings Series 3, Dental Wings Inc., Montreal, Canada). Both dental arches were digitised separately to preserve the

* Corresponding author. Dipartimento di Scienze Biomediche per la Salute, via Mangiagalli 31 - I-20133 MILANO - Italy.
Tel.: +39 – 02 503 15407; fax: +39 – 02 503 15387.
E-mail address: chiarella.sforza@unimi.it (C. Sforza).
[1] Current affiliation: Anatomage Inc., San Jose, CA, USA

http://dx.doi.org/10.1016/j.bjoms.2016.01.019
0266-4356/© 2016 The British Association of Oral and Maxillofacial Surgeons. Published by Elsevier Ltd. All rights reserved.

original alignment of teeth and occlusion using the DWOS software (Dental Wings Inc., Montreal, Canada).[4]

Data for facial soft tissues were acquired twice using a stereophotogrammetric system (Vectra 3D, Canfield Scientific, Fairfield, NJ), the first time with lips open and cheek retractors (so that the front teeth were visible) and the second time at rest.[4]

The two surfaces of the subject's face were recorded as previously described.[4] To record the digitised dental casts, we developed a new approach that used a point-based, and subsequently a surface-based, recording.

First, a region of interest (ROI) that contained the same upper frontal teeth was selected on the "open-lips" stereophotogrammetric and laser-scanned surfaces of the upper dental arches. Then at least three points were selected in each ROI to record them using the Procrustes method.[5] Either anatomical landmarks or points of interest that were easily detectable on both surfaces were used. To evaluate recording of ROI, the median (IQR) distances between the point clouds of the ROI were calculated. The percentages of corresponding points less than 1 mm distance between the two ROI, were also evaluated.[6]

This recording was refined using the iterative closest point algorithm.[5] Once the geometric transformation that indicates this process had been calculated, it was applied to the original dental casts to provide their correct position (Fig. 1).

To validate the proposed algorithm, 11 landmarks were placed both on the cone-beam CT image and on the recorded facial and dental surfaces of each subject. The chosen landmarks were: right and left Orbitale (lOr, rOr), Pronasale (Prn), Subnasale (Sn), Sublabiale (Sl), upper and lower interincisal (uIn, lIn), and the distal vestibular cups of the first molars (16, 46, 26, 36). To evaluate the accuracy of the digital dentofacial reconstruction, 28 distances were calculated, and the significance of the differences between the relevant ones were compared with the Wilcoxon signed rank test.

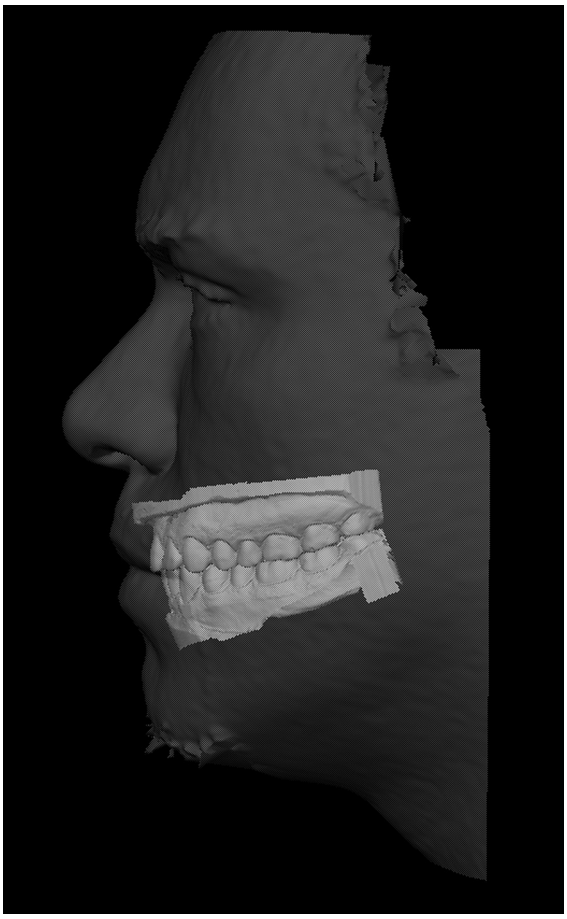

Fig. 1. Example of recorded outcome between facial and dental surfaces. The dark surface indicates the stereophotogrammetric acquisition of the face and the light surface the digitised dental casts (published with the permission of the patient).

Results

The median distance between ROI point clouds was 0.59 (0.43–0.73) mm, and the median percentage of corresponding points was 86.1% (81.6% - 92.1%). There were no significant differences among the evaluated distances except for the distance 36 – rOr (p-0.03; Tables 1 and 2).

Discussion

Compared with the previous method, this technique allows us to record both dental arches separately providing a complete picture of the patient's teeth,[4] and the recording algorithm was validated on a sample of subjects.[3,7] The high percentages of corresponding points, the reduced median distance, and the almost complete lack of significant differences between paired distances (cone-beam CT compared with facial and dental surfaces), prove the accuracy of the recording progress.

Table 1
Median (IQR) distances (mm) between facial landmarks and landmarks on the upper dental arch.

Distance	Cone-beam computed tomography	Matched surfaces	p value
uIn – lOr	66.3 (7.0)	64.8 (3.2)	0.43
uIn – rOr	67.4 (3.2)	64.3 (4.9)	0.06
uIn – Prn	46.3 (3.6)	45.9 (3.2)	0.84
uIn – Sn	27.3 (1.6)	27.1 (1.6)	1.00
16 – lOr	83.8 (7.2)	83.8 (3.0)	1.00
16 – rOr	53.2 (3.4)	54.2 (3.0)	0.56
16 – Prn	73.9 (5.6)	75.7 (2.5)	0.16
16 – Sn	55.7 (5.8)	57.4 (1.6)	0.31
16 – Sl	49.0 (3.0)	50.4 (2.5)	0.06
26 – lOr	52.4 (3.6)	54.2 (2.5)	0.16
26 – rOr	83.6 (6.2)	83.8 (1.8)	0.84
26 – Prn	73.7 (1.7)	74.9 (1.3)	0.09
26 – Sn	55.7 (2.6)	57.1 (4.6)	0.22
26 – Sl	48.8 (7.0)	49.3 (4.1)	0.69

Table 2
Median (IQR) distances (mm) between facial landmarks and landmarks on the lower dental arch.

Distance	Cone-beam computed tomography	Matched surfaces	p value
lIn – lOr	64.3 (6.4)	63.1 (5.8)	0.56
lIn – rOr	65.5 (4.4)	62.3 (7.1)	0.07
lIn – Prn	46.8 (4.7)	46.9 (3.2)	0.84
lIn – Sn	27.2 (2.2)	27.4 (0.9)	1.00
46 – lOr	84.2 (5.4)	80.7 (1.7)	0.09
46 – rOr	55.7 (2.5)	53.4 (2.3)	0.09
46 – Prn	74.7 (4.6)	73.2 (3.3)	0.31
46 – Sn	56.1 (4.4)	54.7 (2.0)	0.31
46 – Sl	47.5 (1.2)	48.3 (3.8)	0.44
36 – lOr	54.9 (0.4)	50.6 (2.7)	0.16
36 – rOr	84.3 (4.5)	79.4 (3.0)	0.03
36 – Prn	74.1 (2.0)	70.5 (1.2)	0.09
36 – Sn	55.8 (3.2)	52.8 (4.2)	0.16
36 – Sl	46.8 (3.2)	47.8 (4.9)	0.44

Results are encouraging. This technique may be useful to assess the position of the patient's face with respect to the teeth. Nevertheless, further validations on a larger sample are advisable.

Conflict of Interest

We have no conflict of interest.

Ethics statement/confirmation of patient's permission

All study procedures were non-invasive and carried out according to the Declaration of Helsinki. All subjects gave their written consent. The figure was published with the permission of the patient.

References

1. Eaton KA, Reynolds PA, Grayden SK, et al. A vision of dental education in the third millennium. *Br Dent J* 2008;**205**:261–71.
2. Sforza C, de Menezes M, Ferrario VF. Soft- and hard-tissue facial anthropometry in three dimensions: what's new. *J Anthropol Sci* 2013;**91**:159–84.
3. Rangel FA, Maal TJ, Bergé SJ, et al. Integration of digital dental casts in 3-dimensional facial photographs. *Am J Orthod Dentofac Orthop* 2008;**134**:820–6.
4. Rosati R, De Menezes M, Rossetti A, et al. Digital dental cast placement in 3-dimensional, full-face reconstruction: A technical evaluation. *Am J Orthod Dentofac Orthop* 2010;**138**:84–8.
5. Hill DL, Batchelor PG, Holden M, et al. Medical image registration. *Phys Med Biol* 2001;**46**:R1–45.
6. Nkenke E, Zachow S, Benz M, et al. Fusion of computed tomography data and optical 3D images of the dentition for streak artefact correction in the simulation of orthognathic surgery. *Dentomaxillofacial Radiol* 2004;**33**:226–32.
7. Galantucci LM, Percoco G, Lavecchia F, et al. Noninvasive computerized scanning method for the correlation between the facial soft and hard tissues for an integrated three-dimensional anthropometry and cephalometry. *J Craniofac Surg* 2013;**24**:797–804.

Journal of Cranio-Maxillo-Facial Surgery xxx (2016) 1–6

Contents lists available at ScienceDirect

Journal of Cranio-Maxillo-Facial Surgery

journal homepage: www.jcmfs.com

Facial thirds–based evaluation of facial asymmetry using stereophotogrammetric devices: Application to facial palsy subjects☆

Marina Codari [a], Valentina Pucciarelli [a], Fabiano Stangoni [a], Matteo Zago [a], Filippo Tarabbia [b], Federico Biglioli [b], Chiarella Sforza [a, *]

[a] Department of Biomedical Sciences for Health (Director: Prof. Francesco Auxilia), Facoltà di Medicina e Chirurgia, Università degli Studi di Milano, Milano, Italy
[b] Maxillo-Facial Surgery Unit, San Paolo University Hospital, San Paolo Hospital, Department of Health Sciences (Director: Prof. Silvio Scarone), Facoltà di Medicina e Chirurgia, Università degli Studi di Milano, Milano, Italy

ARTICLE INFO

Article history:
Paper received 7 June 2016
Accepted 8 November 2016
Available online xxx

Keywords:
Facial asymmetry
Photogrammetry
Facial paralysis

ABSTRACT

Many conditions can compromise facial symmetry, resulting in an impairment of the affected person from both esthetic and functional points of view. For these reasons, a detailed, focused, and objective evaluation of facial asymmetry is needed, both for surgical planning and for treatment evaluation.

In this study, we present a new quantitative method to assess symmetry in different facial thirds, objectively defined on the territories of distribution of trigeminal branches.

A total of 70 subjects (40 healthy controls and 30 patients with unilateral facial palsy) participated. A stereophotogrammetric system and the level of asymmetry of the subjects' hemi-facial thirds was evaluated, comparing the root mean square of the distances (RMSD) between their original and mirrored facial surfaces.

Results show a high average reproducibility of area selection (98.8%) and significant differences in RMSD values between controls and patients ($p = 0.000$) for all of the facial thirds. No significant differences were found on different thirds among controls ($p > 0.05$), whereas significant differences were found for the upper, middle, and lower thirds of patients ($p = 0.000$).

The presented method provides an accurate, reproducible, and local facial symmetry analysis that can be used for different conditions, especially when only part of the face is asymmetric.

© 2016 European Association for Cranio-Maxillo-Facial Surgery. Published by Elsevier Ltd. All rights reserved.

1. Introduction

Many pathologies can result in facial asymmetry. Among these, hemifacial microsomia, cleft lip/palate, mandibular osteochondroma, trauma and infections, untreated mandibular fractures, and damage to facial nerves are mentionable. In particular, facial nerve palsy, which can be due to different etiologies, from neoplasm to infective, traumatic, congenital, and metabolic causes, can strongly alter facial harmony (Melvin and Limb, 2008). Furthermore, environmental factors, such as chewing and sucking habits, or craniofacial syndromes, can compromise facial symmetry (Bishara et al., 1994; Avelar et al., 2010). The amount of asymmetry of the face can vary among subjects, ranging from unperceived or subclinical cases to evident and clear ones. In those cases, aesthetics, appearance and functionality of the orofacial district can be severely affected, leading to discomfort and dissatisfaction of the patients regarding their own facial appearance (Kim et al., 2015; Thiesen et al., 2015).

To both improve aesthetics and correct functional defects, an objective, quantitative assessment of facial asymmetry is advised. The quantification of asymmetry can be especially useful during surgical treatment planning, but it can also be performed during follow-up examinations, allowing surgeons and dentists to evaluate the progressive reduction of asymmetry, therapy progression, and achieved results (Claes et al., 2012; Chatrath et al., 2016; Verhoeven et al., 2016).

The evaluation of facial morphology evolved during the last decades, passing from the direct measurement to an indirect

☆ No grants were obtained for this investigation.

* Corresponding author. Department of Biomedical Sciences for Health, Università degli Studi di Milano, via Mangiagalli 31, 20133 Milan, Italy. Fax: +39 0250315387.
E-mail address: chiarella.sforza@unimi.it (C. Sforza).

http://dx.doi.org/10.1016/j.jcms.2016.11.003
1010-5182/© 2016 European Association for Cranio-Maxillo-Facial Surgery. Published by Elsevier Ltd. All rights reserved.

Please cite this article in press as: Codari M, et al., Facial thirds–based evaluation of facial asymmetry using stereophotogrammetric devices: Application to facial palsy subjects, Journal of Cranio-Maxillo-Facial Surgery (2016), http://dx.doi.org/10.1016/j.jcms.2016.11.003

assessment of the face, through two- and three-dimensional imaging systems (Smeets et al., 2010). These technologies can allow not only a facial analysis based on landmarks, but also the investigation of the whole surface (Richtsmeier et al., 2002). Surface assessments have already been found to be more sensitive than landmark measurements (Verhoeven et al., 2016). Currently, facial asymmetry is evaluated mainly by using the entire facial surface, thus providing measurements that give only general information about facial morphology (Ostwald et al., 2015; Verhoeven et al., 2016). In contrast, several pathologies affecting facial appearance are localized in selected parts of the face (Avelar et al., 2010; Djordjevic et al., 2014a), and a local assessment can provide helpful information for clinical decisions.

In this study, we introduce a new method that combines surface and landmarks based approaches to assess facial asymmetry, taking different facial thirds into account, in order to provide local information. The intra-operator repeatability of the method was assessed, and a practical application in patients with unilateral facial palsy was made.

2. Material and methods

2.1. Sample

A total of 70 adult Caucasian subjects were voluntarily recruited for this study. This sample was composed of 40 healthy subjects (21 females; 19 males; average age 39 ± 12 years) and 30 patients with diagnosed unilateral facial palsy (15 females; 15 males; average age 44 ± 15 years). All healthy subjects had no history of facial trauma, maxillofacial surgery, and craniofacial syndromes or deformities. Among the patients, the etiologies of the facial nerve palsy were oncological surgery (71%), Bell's palsy (18%), trauma (7%), and brainstem embolus due to arterio-venous malformations (4%).

2.2. Image acquisition

Images for all of the involved subjects were acquired using the VECTRA M3 stereophotogrammetric system (Canfield Scientific Inc., Fairfield, NJ), which allows scanning of faces in a fast and non-invasive way (Sforza et al., 2013). Before the acquisition, 50 soft tissue facial landmarks were marked using black liquid eyeliner, following a protocol that was previously developed, tested and validated by our research group (Ferrario et al., 1998; De Menezes et al., 2010). During the acquisition, subjects were asked to have a neutral facial expression of the face, with teeth in loose contact and closed mouth. The institutional review board of the University of Milan (approval n. 92/2014) approved all the described procedures and all patients gave their written informed consent.

After the acquisition process, the facial landmarks were digitally marked on each surface, to delimit the portions of the face used for asymmetry evaluation, using the manufacturer's software (Mirror Vectra; Canfield Scientific Inc., Fairfield, NJ).

2.3. Asymmetry quantification

To define the portion of face used to evaluate the asymmetry of the subject, 10 facial landmarks were selected. A detailed list of these landmarks is provided in Table 1. Landmark selection allows one to delimit the facial surface in a standard and repeatable way, thus reducing operator dependency. An example of the selected surface is depicted in Fig. 1.

Intra-operator repeatability of facial area (FA) selection was evaluated on a training sample of 20 facial surfaces. One experienced operator selected the different facial thirds and the FA twice with a 2-week interval. The repeatability was assessed on facial surface selection since it is the main cause of variability in surface mirroring approaches, as further image processing steps are automated. After landmark identification, the Mirror Vectra software (Canfield Scientific Inc., Fairfield, NJ) automatically computed the surface area.

The selected surface was then used to calculate the plane of maximum symmetry, this process allowed us to automatically find the midline plane of symmetry using only a previously selected area on the acquired facial surface. In this study, the selected area was defined in order to minimize the regions that can affect asymmetry quantification, such as hairs and neck region, and to take all the craniofacial structures of interest for maxillofacial morphometric analysis into account. This processing step was carried out using the Mirror imaging software (Canfield Scientific Inc., Fairfield, NJ).

Once the plane of maximum symmetry was obtained, it was used as a mirroring plane to obtain the reflected face of each subject.

The original facial surface was then divided in two hemi-face surfaces, which were subsequently subdivided into three different facial thirds: upper (UT), middle (MT), and lower third (LT). In the proposed method, facial thirds division was based on the territories of distribution of trigeminal branches, which correspond to different embryological origins (Holmes, 2016). Each third was defined using anatomical landmarks, thus providing a standard and repeatable selection criterion. The list of landmarks used to define each facial third is provided in Table 1, and an example of facial third selection is depicted in Fig. 2.

Finally, to quantify the asymmetry of each facial third in each subject, the root mean square deviation (RMSD) between the original and reflected surfaces was calculated. A color-coded surface map displayed the local values of the distances between the two surfaces, as can be seen in Fig. 3. The RMSD has already proved to be a reproducible and accurate way to measure facial asymmetry, using three-dimensional photogrammetric systems (Taylor et al., 2014).

2.4. Statistical analysis

The Chi-square test was used to check differences in sex distribution between control and patient groups, while an unpaired Student's t test was used to check age difference.

Table 1
Landmarks used to define facial areas and the facial thirds.

Landmarks	
Facial area (FA)	trichion (tr); frontotemporale (ft); zygion (zy); tragion (t); gonion (go); gnathion (gn)
Upper third (UT)	trichion (tr); glabella (g); nasion (n); pronasale (prn); columella (c); alare (al); endocanthion (en); exocanthion (ex); frontotemporale (ft)
Middle third (MT)	endocanthion (en); alare (al); upper terminal of the nostril (stn); columella (c); subnasale (sn); labiale superius (ls); stomion (sto); chelion (ch); zygion (zy); frontotemporale (ft); exocanthion (ex)
Lower third (LT)	stomion (sto), labiale inferius (li); sublabiale (sl); pogonion (pg); gnathion (gn); gonion (go); tragion (t); zygion (zy); cheilion (ch)

Please cite this article in press as: Codari M, et al., Facial thirds–based evaluation of facial asymmetry using stereophotogrammetric devices: Application to facial palsy subjects, Journal of Cranio-Maxillo-Facial Surgery (2016), http://dx.doi.org/10.1016/j.jcms.2016.11.003

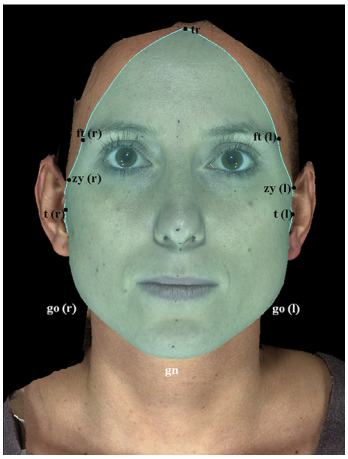

Fig. 1. Facial area (FA) selected to evaluate asymmetry, based on the more external anthropometric landmarks of the face. Landmarks that are not visible from the frontal view are shown in white; r and l indicate right and left side of the face, respectively.

The repeatability in surface area selection was tested using Bland–Altman analysis for both the total facial area and each facial third. For repeated area measurements, the bias value, which corresponds to the systematic error, and the repeatability coefficient (RC), which represents the least detectable difference among measurements and is twice the standard deviation of measurement differences (Bland and Altman, 1986), were calculated.

Box plots were used for representing RMSD values of different facial thirds in different subject groups. Normality distribution of the data was tested using the Kolmogorov–Smirnov test. RMSD of different facial thirds in both control and pathological subjects were positively skewed, so logarithmic transformation of the data was performed in order to obtain normal distributions. After this transformation, a two-way analysis of variance (ANOVA) was performed in order to determine whether there were statistically significant differences among the groups and facial thirds. Post hoc analyses were performed using Fisher's LSD test. The statistical level of significance was set to $p < 0.05$ for all tests.

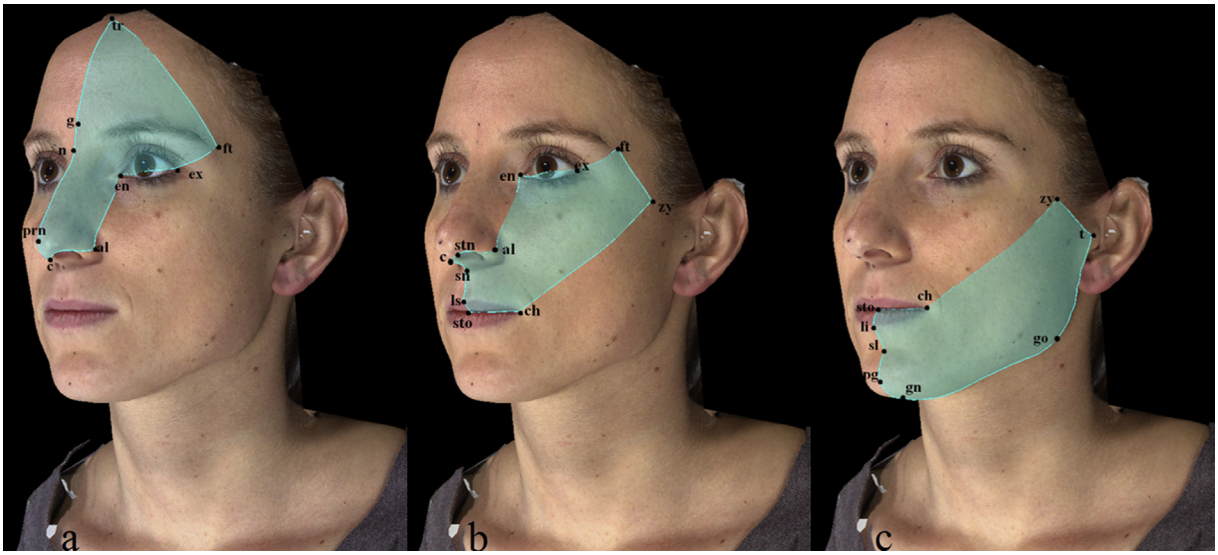

Fig. 2. (a) Upper facial third (UT); (b) middle facial third (MT); (c) lower facial third (LT). Each facial third is defined by the respective anatomical landmarks, chosen to follow the territories of distribution of trigeminal branches.

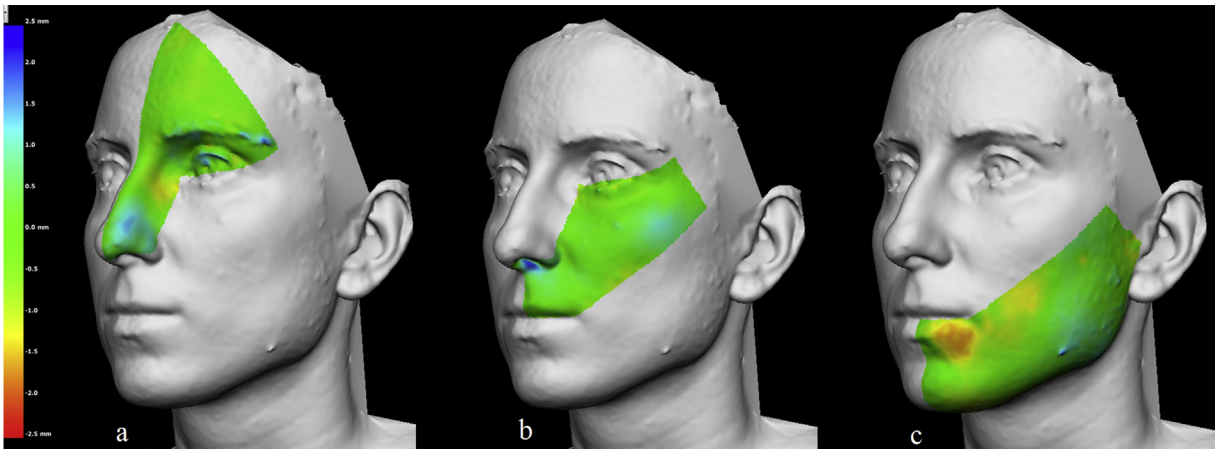

Fig. 3. Color-coded maps for the local distances between the original and mirrored facial areas. (a) Upper third; (b) middle third; (c) lower third.

Please cite this article in press as: Codari M, et al., Facial thirds–based evaluation of facial asymmetry using stereophotogrammetric devices: Application to facial palsy subjects, Journal of Cranio-Maxillo-Facial Surgery (2016), http://dx.doi.org/10.1016/j.jcms.2016.11.003

3. Results

In this study, 40 control subjects and 30 patients with diagnosed unilateral facial palsy were analyzed. No statistically significant differences were found in age ($p = 0.1$, Student's t test) and sex distribution ($p = 0.84$, Chi-square test).

The statistical analysis of the repeated area measurements showed high level of reproducibility. Bland–Altman plots and the values of bias, standard deviation (SD), repeatability coefficient, and reproducibility are respectively reported in Fig. 4 and Table 2.

Values of RMSD in control subjects and patients, divided for each facial third, are presented in Fig. 5. Overall, patients had a larger asymmetry in all facial thirds than control subjects; the difference appears particularly evident for the middle and lower thirds.

Two-way ANOVA showed a statistically significant difference in RMSD values between control subjects and patients ($p = 0.000$). A significant effect of facial third was also found ($p = 0.0014$), together with a significant group × third interaction ($p = 0.0012$). Among different thirds, the RMSD values of the upper third (UT) resulted significantly different from those of the middle third (MT)

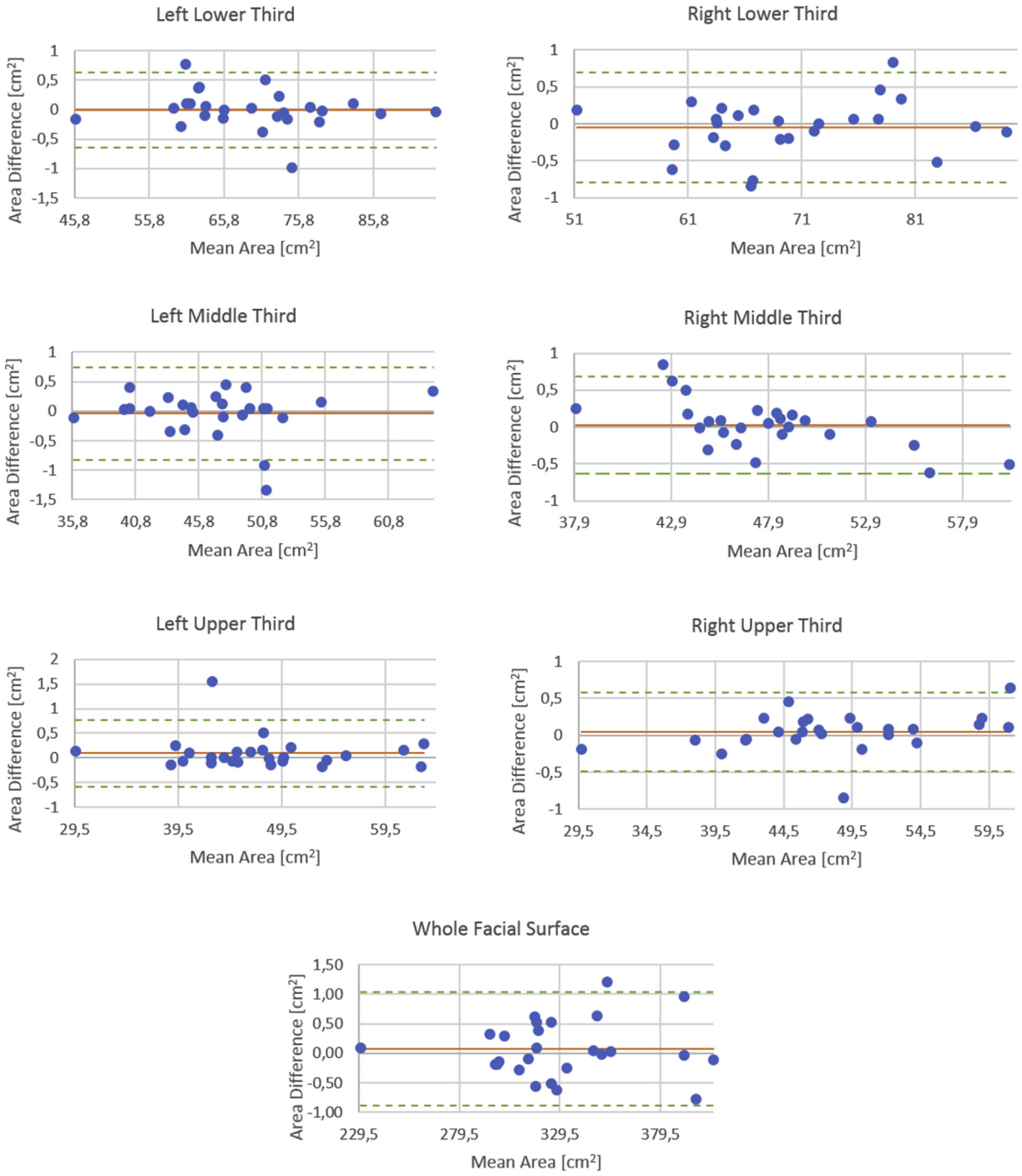

Fig. 4. Bland–Altman plots for the area repeated measurements. Continuous line indicates the average; dashed lines indicate the interval of agreement.

Please cite this article in press as: Codari M, et al., Facial thirds–based evaluation of facial asymmetry using stereophotogrammetric devices: Application to facial palsy subjects, Journal of Cranio-Maxillo-Facial Surgery (2016), http://dx.doi.org/10.1016/j.jcms.2016.11.003

Table 2
Results of Bland–Altman analysis.

	UT		MT		LT		FA
	Left	Right	Left	Right	Left	Right	
Bias (cm^2)	−0.003	−0.051	−0.039	−0.028	0.097	0.043	0.075
SD (cm^2)	0.319	0.372	0.393	0.329	0.340	0.267	0.479
RC (%)	0.9	1.1	1.7	1.4	1.4	1.1	0.6

Bias, standard deviation (SD), and repeatability coefficient (RC) of area measurements are reported for upper third (UT), middle third (MT), and lower third (LT) and the whole facial area (FA).

($p = 0.005$) and lower third (LT) ($p = 0.003$). Post hoc analysis showed that among control subject there was no significant difference between thirds ($p > 0.05$). On the other hand, in patients there was a significant difference between the UT and MT ($p = 0.001$) and between the UT and LT ($p = 0.000$). Comparing the same third between control and patient groups, statistically significant differences were found in all cases ($p = 0.000$).

4. Discussion

The evaluation and quantification of facial asymmetry is a key task in maxillofacial surgery and orthodontics, since a lot of conditions can alter it, thus compromising the patient quality of life from functional, esthetic, and social points of view (Berlin et al., 2014).

The introduction of noninvasive and inexpensive imaging procedures, e.g., laser scan and stereophotogrammetry, has speeded up the research in this field. In the past few years, a lot of work has been published on this topic, suggesting different approaches to assess facial asymmetry (Berssenbrügge et al., 2014; Alqattan et al., 2015; Kornreich et al., 2016; Verhoeven et al., 2016). Unfortunately, none of these is universally accepted from the scientific community, thus demonstrating that is still necessary to improve these procedures (Djordjevic et al., 2014a).

In the proposed method, we analyzed symmetry comparing original and mirrored facial surfaces and calculating the RMSD of the distances between their corresponding points. This approach is well known in the literature and has proved to be a potentially powerful method to analyze facial symmetry (Djordjevic et al., 2014b; Taylor et al., 2014; Ostwald et al., 2015).

Traditionally, the whole face is used to measure the asymmetry level of the subject, thus providing only a global evaluation of facial morphology (Kornreich et al., 2016; Verhoeven et al., 2016). In this study, we divided each hemi-face into thirds, based on trigeminal branches distribution territories for somatic sensitivity. Other researchers have tried to provide a local subdivision of the face using horizontal planes, thus obtaining irregular edges of selected thirds due to subjective selection of the facial area (Djordjevic et al., 2014a; Taylor et al., 2014; Ozsoy, 2016).

In the proposed method, facial area selection is the only manual image processing step needed to quantify the asymmetry of the face using surface mirroring approaches. To obtain a standardized imaging method, it is essential to reduce the variability among different measurements to as low as possible. For this reason, the selection of the FA plays a key role in asymmetry assessment on 3D facial surfaces. In the proposed method, the standardized definition of thirds allowed one to reach a very high level of reproducibility during area selection, which is the main source of variability in asymmetry quantification. Repeatability analysis shows an average RC value (±SD) equal to 1.2% ± 0.005%, proving a high level of agreement between repeated measurements. As shown by the Bland–Altman plot in Fig. 4, the bias is always near 0% (average bias value 0.03% ± 0.001%), thus demonstrating the absence of systematic errors during repeated measurements. Moreover, the division of the face into thirds allows one to focus treatment planning and to follow up evaluations of the most asymmetric region.

To validate the proposed method, both patients with diagnosed unilateral facial palsy and control subjects, matched for sex and age, were enrolled. Unilateral facial palsy causes an evident asymmetry of the facial soft tissues, so it can be considered a perfect condition for testing this method within a clinical context. Other investigations have used artificial, mathematically originated facial asymmetries that can be difficult to translate into daily practice (Verhoeven et al., 2016).

In all subjects, the asymmetry was quantified calculating the RMSD of corresponding points belonging to mirrored hemi-facial thirds. The results show that patients had a significantly less asymmetric UT compared to the MT and LT. Indeed, the UT is composed mainly by the frontal region, which is the area less affected by facial palsy. On the other hand, despite the fact that this third is less asymmetric than the other two, it is still more asymmetrical in patients than in control subjects. That can also be explained by the fact that the upper eyelid/superior orbital region, which is strongly altered in facial nerve palsy, is part of our UT. Among control subjects, there was no significant difference in

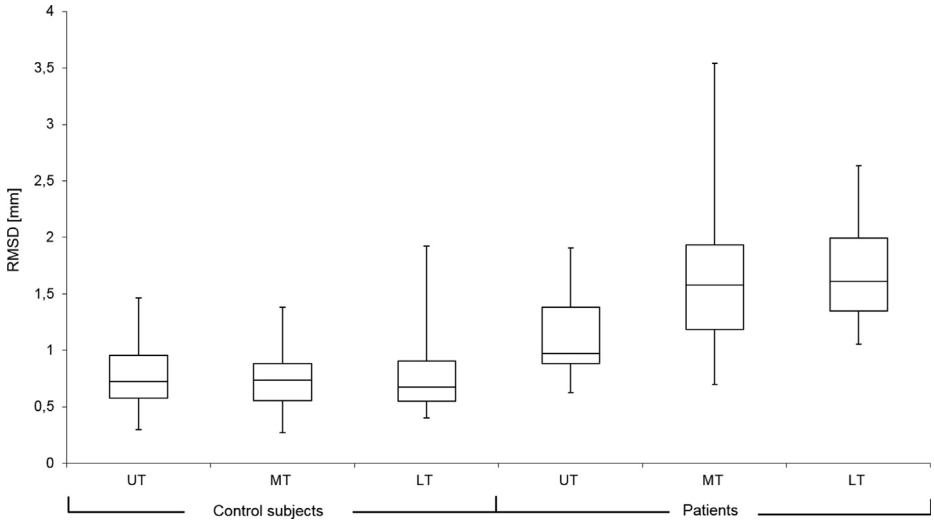

Fig. 5. Box plots, representing root mean square (RMS) values of controls subjects and patients for upper, middle, and lower facial thirds.

Please cite this article in press as: Codari M, et al., Facial thirds–based evaluation of facial asymmetry using stereophotogrammetric devices: Application to facial palsy subjects, Journal of Cranio-Maxillo-Facial Surgery (2016), http://dx.doi.org/10.1016/j.jcms.2016.11.003

RMSD values of different thirds, thus confirming the recent observations of Djordjevic et al. (2014b).

These results proved the accuracy of the proposed method in asymmetry quantification, both in physiological and pathological conditions, allowing clinicians to use it with different kinds of pathologies. Moreover, the strong reproducibility of this method makes it suitable for follow-up evaluations in different craniofacial conditions.

5. Conclusion

With this study a facial third–based method for the analysis of facial asymmetry is provided. The method showed high reproducibility and accuracy in evaluating differences between control subjects and patients. Moreover, it is applicable for diagnosis, treatment planning, and evaluation in patients with altered craniofacial morphology. In particular, the method appears suitable for pathologies that alter only part of the face, providing quantitative local information about facial symmetry.

References

Alqattan M, Djordjevic J, Zhurov AI, Richmond S: Comparison between landmark and surface-based three-dimensional analyses of facial asymmetry in adults. Eur J Orthod 37: 1–12, 2015

Avelar RL, Goelzer JG, Azambuja FG, de Oliveira RB, de Oliveira MP, Pase PF: Use of autologous fat graft for correction of facial asymmetry stemming from Parry-Romberg syndrome. Oral Surg Oral Med Oral Pathol Oral Radiol Endodontol 109: e20–e25, 2010

Berlin NF, Berssenbrügge P, Runte C, Wermker K, Jung S, Kleinheinz J, et al: Quantification of facial asymmetry by 2D analysis. A comparison of recent approaches. J Cranio-Maxillofacial Surg 42: 265–271, 2014

Berssenbrügge P, Franka N, Kebeck G, Runte C, Jung S, Kleinheinzc J, et al: 2D and 3D analysis methods of facial asymmetry in comparison. J Cranio-Maxillofac Surg 42: e327–e334, 2014

Bishara SE, Burkey PS, Kharouf JG: Dental and facial asymmetries: a review. Angle Orthod 64: 89–98, 1994

Bland JM, Altman DG: Statistical methods for assessing agreement between two methods of clinical measurement. Lancet 1: 307–310, 1986

Chatrath P, De Cordova J, Nouraei SAR, Ahmed J, Saleh HA: Objective assessment of facial asymmetry in rhinoplasty patients. Arch Facial Plast Surg 9: 184–187, 2016

Claes P, Walters M, Clement J: Improved facial outcome assessment using a 3D anthropometric mask. Int J Oral Maxillofac Surg 41: 324–330, 2012

Djordjevic J, Lewis BM, Donaghy CE, Zhurov AI, Knox J, Hunter L, et al: Facial shape and asymmetry in 5-year-old children with repaired unilateral cleft lip and/or palate: an exploratory study using laser scanning. Eur J Orthod 36: 497–505, 2014a

Djordjevic J, Toma AM, Zhurov AI, Richmond S: Three-dimensional quantification of facial symmetry in adolescents using laser surface scanning. Eur J Orthod 36: 125–132, 2014b

Ferrario VF, Sforza C, Poggio CE, Cova M, Tartaglia G: Preliminary evaluation of an electromagnetic three-dimensional digitizer in facial anthropometry. Cleft Palate-Craniofac J 35: 9–15, 1998

Holmes S: Face and scalp. In: Standring S (ed.), Gray's anatomy, 41th ed. Amsterdam: Elsevier, 501–502, 2016

Kim J-Y, Kang M-H, You J-Y, Jee HG, Yi JW, Kim BH: Natural head postures of patients with facial asymmetry in frontal view are corrected after orthognathic surgeries. J Oral Maxillofac Surg 74: 1–7, 2015

Kornreich D, Mitchell AA, Cristian I, Jabs EW: Quantitative assessment of facial asymmetry using three-dimensional surface imaging in adults: validating the precision and repeatability of a global approach. Cleft Palate Craniofac J 53: 126–131, 2016

Melvin TA, Limb CJ: Overview of facial paralysis: current concepts. Fac Plast Surg 24: 155–163, 2008

De Menezes M, Rosati R, Ferrario VF, Sforza C: Accuracy and reproducibility of a 3-dimensional stereophotogrammetric imaging system. J Oral Maxillofac Surg 68: 2129–2135, 2010

Ostwald J, Berssenbrügge P, Dirksen D, Runte C, Wermker K, Kleinheinz J, et al: Measured symmetry of facial 3D shape and perceived facial symmetry and attractiveness before and after orthognathic surgery. J Cranio-Maxillofac Surg 43: 521–527, 2015

Ozsoy U: Comparison of different calculation methods used to analyze facial soft tissue asymmetry: global and partial 3D quantitative evaluation of healthy subjects. J Oral Maxillofac Surg 74: 1847.e1–1847.e9, 2016

Richtsmeier JT, DeLeon VB, Lele SR: The promise of geometric morphometrics. Yearb Phys Anthropol 45: 63–91, 2002

Sforza C, de Menezes M, Ferrario VF: Soft- and hard-tissue facial anthropometry in three dimensions: what's new. J Anthropol Sci 91: 159–184, 2013

Smeets D, Claes P, Vandermeulen D, Clement JG: Objective 3D face recognition: evolution, approaches and challenges. Forensic Sci Int 201: 125–132, 2010

Taylor HO, Morrison CS, Linden O, Phillips B, Chang J, Byrne ME, et al: Quantitative facial asymmetry: using three-dimensional photogrammetry to measure baseline facial surface symmetry. J Craniofac Surg 25: 124–128, 2014

Thiesen G, Gribel BF, Freitas PM: Facial asymmetry: a current review 20: 110–125, 2015

Verhoeven T, Xi T, Schreurs R, Bergé S, Maal T: Quantification of facial asymmetry: a comparative study of landmark-based and surface-based registrations. J Craniomaxillofac Surg 44: 1131–1136, 2016

Please cite this article in press as: Codari M, et al., Facial thirds–based evaluation of facial asymmetry using stereophotogrammetric devices: Application to facial palsy subjects, Journal of Cranio-Maxillo-Facial Surgery (2016), http://dx.doi.org/10.1016/j.jcms.2016.11.003

International Journal of Computer Assisted Radiology and Surgery

Computer-aided 3D cephalometric landmark annotation for CBCT data

--Manuscript Draft--

Manuscript Number:	CARS-D-16-00015R2
Full Title:	Computer-aided 3D cephalometric landmark annotation for CBCT data
Article Type:	Original Article
Keywords:	Cone-Beam CT; Cephalometry; Image segmentation; Image registration
Corresponding Author:	Chiarella Sforza, MD Università degli studi di MIlano Milano, ITALY
Corresponding Author Secondary Information:	
Corresponding Author's Institution:	Università degli studi di MIlano
Corresponding Author's Secondary Institution:	
First Author:	Marina Codari, MSc Biomedical Engineering
First Author Secondary Information:	
Order of Authors:	Marina Codari, MSc Biomedical Engineering
	Matteo Caffini, MSc Biomedical Engineering, PhD
	Gianluca Martino Tartaglia, DDS, PhD
	Chiarella Sforza, MD
	Giuseppe Baselli, MSc Electronics Engineering
Order of Authors Secondary Information:	
Funding Information:	
Abstract:	Purpose: Nowadays, with the increased diffusion of Cone Beam Computerized Tomography (CBCT) scanners in dental and maxilla-facial practice, 3D cephalometric analysis is emerging. Maxillofacial surgeons and dentists make wide use of cephalometric analysis in diagnosis, surgery and treatment planning. Accuracy and repeatability of the manual approach, the most common approach in clinical practice, are limited by intra- and inter-subject variability in landmark identification. So, we propose a computer-aided landmark annotation approach that estimates the three-dimensional (3D) positions of 21 selected landmarks. Methods: The procedure involves an adaptive cluster-based segmentation of bone tissues followed by an intensity-based registration of an annotated reference volume onto a patient Cone Beam CT (CBCT) head volume. The outcomes of the annotation process are presented to the clinician as a 3D surface of the patient skull with the estimate landmark displayed on it. Moreover, each landmark is centered into a spherical confidence region that can help the clinician in a subsequent manual refinement of the annotation. The algorithm was validated onto 18 CBCT images. Results: Automatic segmentation shows a high accuracy level with no significant difference between automatically and manually determined threshold values. The overall median value of the localization error was equal to 1.99 mm with an interquartile range (IQR) of 1.22 - 2.89 mm. Conclusion: The obtained results are promising, segmentation was proved to be very robust and the achieved accuracy level in landmark annotation was acceptable for most of landmarks and comparable with other available methods.

Powered by Editorial Manager® and ProduXion Manager® from Aries Systems Corporation

Manuscript

Click here to view linked References

Click here to download Manuscript CARS-D-16-00015_Second revision.docx

Computer aided cephalometric landmark annotation for CBCT data

Marina Codari[1], Matteo Caffini[2], Gianluca M. Tartaglia[1,3], Chiarella Sforza[1], Giuseppe Baselli[4]

1) Department of Biomedical Sciences for Health, Università degli Studi di Milano, 20133, Milano MI, Italy

2) CIMeC, Università degli Studi di Trento, 38068, Rovereto, TN, Italy

3) SST Dentofacial Clinic, 20090, Segrate, MI, Italy.

4) Department of Electronics, Information and Bioengineering, Politecnico di Milano, 20133, Milano MI, Italy

Purpose: Nowadays, with the increased diffusion of Cone Beam Computerized Tomography (CBCT) scanners in dental and maxilla-facial practice, 3D cephalometric analysis is emerging. Maxillofacial surgeons and dentists make wide use of cephalometric analysis in diagnosis, surgery and treatment planning. Accuracy and repeatability of the manual approach, the most common approach in clinical practice, are limited by intra- and inter-subject variability in landmark identification. So, we propose a computer-aided landmark annotation approach that estimates the three-dimensional (3D) positions of 21 selected landmarks.

Methods: The procedure involves an adaptive cluster-based segmentation of bone tissues followed by an intensity-based registration of an annotated reference volume onto a patient Cone Beam CT (CBCT) head volume. The outcomes of the annotation process are presented to the clinician as a 3D surface of the patient skull with the estimate landmark displayed on it. Moreover, each landmark is centered into a spherical confidence region that can help the clinician in a subsequent manual refinement of the annotation. The algorithm was validated onto 18 CBCT images.

Results: Automatic segmentation shows a high accuracy level with no significant difference between automatically and manually determined threshold values. The overall median value of the localization error was equal to 1.99 mm with an interquartile range (IQR) of 1.22 - 2.89 mm.

Conclusion: The obtained results are promising, segmentation was proved to be very robust and the achieved accuracy level in landmark annotation was acceptable for most of landmarks and comparable with other available methods.

Keywords: Cone-Beam CT, Cephalometry, Image segmentation, Image registration

1. INTRODUCTION

The measurement of the head, known as cephalometry, considers both soft and hard tissues and has many applications in today's world. The application of cephalometry to the clinical needs, commonly known as cephalometric analysis, is widely used in dental applications, such as orthodontics and implantology, and in surgical planning and treatment evaluation for maxillofacial surgery [1–3]. Traditionally, cephalometric analyses have been manually performed on a 2D cephalogram, which is a standardized tracing of craniofacial structures as depicted by a latero-lateral radiography of the head. Currently, with the diffusion of Cone Beam Computerized Tomography (CBCT) scanners, 3D cephalometric analysis is emerging [4]. CBCT is used for small segments of the body, such as the head or part of it, and generally delivers lower dose to the patient, compared to CT [5]. In particular, CBCT is a useful tool for identification and evaluation of treatment outcomes, becoming one of the most common image modality used to visualize the facial skeleton [6–8]. Both maxillofacial surgeons and dentists can foresee remarkable developments by the aid of computerized methods permitting to easily extract individual features and perform measurements.

Nowadays, manual point-picking represents the method of choice to perform 3D cephalometric analysis, however this approach is limited in accuracy and repeatability due to the differences in intra- and inter-operator landmark identification [9–11]. The need to overcome these limitations recently led to the development of aided, automated or nearly-automated methods [12–18]. Here, we propose a semi-automatic computerized method that can help the clinician to annotate three-dimensional CBCT volumes of the human head, using intensity-based image registration.

2. MATERIALS AND METHODS

The proposed algorithm, entirely developed in MATLAB (MathWorks, Natick, MA, USA), automatically segments the skull from CBCT volumes of the human head and subsequently estimates a number of cephalometric landmarks. The flowchart of the proposed algorithm is presented in Fig. 1.

2.1 Anatomical Landmarks

In this study, a set of fiducial points, which location will be estimated, must be decided and defined. To validate the proposed method, a set of 21 landmarks, commonly used in clinical practice and distributed

all over the skull surface, was chosen [19]. All chosen landmarks and their definition are listed in Tab.1. [20].

2.2 Dataset

Datasets of 18 subjects who underwent CBCT imaging examination at the SST Dentofacial Clinic, Italy, were retrospectively selected. These images were acquired for reasons independent of this study and in all acquisitions the device was operated at 6-10 mA (pulse mode) and 105 kV using a X-ray generator with fixed anode and 0.5 mm nominal focal spot size. All images were acquired with cephalometric field of view (200 mm x 170 mm). All subjects were adult healthy Caucasian women, aged from 37 to 74 years, who had teeth in both dental arches. No limitations was set to the presence of dental implants, dental fillings or even on particular dental treatments carried out before the radiological examination.

2.3 Image Preprocessing

In order to standardize the structures in the CBCT data, the proposed method requires a single initialization step consisting in pointing the most inferior point of the mandibular bone. Currently, this is the only manual operation required; however, this is easy to automatize, provided a standard patient's positioning on the scanner chin set. Next, the volume is cut off below the selected slice and the algorithm proceeds automatically in landmarks' identification. This simple step defines a common criterion for volume limitation capable of providing a coarse standardization of the structures.

Subsequently, to improve the accuracy of the segmentation procedures and to make it robust to the presence of noise, the image was filtered using a three-dimensional low pass Gaussian filter. The size of this cubic filter was set to 3 voxels in order to limit the blurring effect, increase signal to noise ratio and preserve the morphology of craniofacial bones [21].

2.4 Image Segmentation

The segmentation algorithm aims at a standard hard-tissue thresholding, though after a subject-specific adaptation with no manual interaction and no training dataset or previously developed models. A major consideration driving the algorithm design was that CBCT scanners provide less calibrated contrasts than CTs, thus reducing the confidence in preset thresholds [22].

This aim was approached by k-means clustering separately performed on a representative subset of the volume slices. In particular, the k-means clustering was chosen due to its low sensitivity to initialization parameters, relatively low computational complexity and its suitability for biomedical image segmentation since the number of clusters can be easily defined based on prior anatomical knowledge [23, 24].

The present validation considered a 1:2 reduction, by analyzing each second slice; however, further preliminary trials revealed that higher reduction factors improved efficiency with no accuracy loss. As detailed below, the statistics of clusters was used to set the optimal soft/hard tissue separation threshold; also, a good robustness against dental metal artifacts was achieved by proper elimination of low-density outliers.

Within each subset, slice tissues were classified into 4 main categories, one representing air, two representing soft tissues and one representing hard tissues. The classification was performed using a k-means clustering approach [25]. The following statistics through the subset of slices considered the minimum of the highest intensity cluster; i.e., the one intended to classify bone and tooth tissue.

These values allowed to determine the global threshold which was defined at the 10th percentile of the population of minima. This threshold value was shown to make the algorithm robust to misclassification of tissues in a limited (i.e., less than 10%) number of slices that are easily classified as outliers. The 10% rule was ~~shown~~ selected to avoid a specific search of outliers.

After the optimized threshold value was obtained, it was possible to proceed with the thresholding of the entire volume that needs to be segmented, since preliminary analyses confirmed that possible intensity calibration trends through slices were negligible. The outcome of single voxel thresholding was next improved by removing all the residual volumes of the segmentation process, caused by the presence of noise or artifacts. A 3D labelling process identified all structures and those presenting a volume lower than 0.1% of the total segmented volume were eliminated. An example of the outcome of the segmentation process is shown in Fig.2.

2.5 Image Registration

Landmark placement was based on the propagation of landmarks through the registration on an annotated reference skull. The reference skull was automatically segmented with the above presented method and annotated in a double blind process by three expert operators for three times, in order to take intra and inter-operator variability into account. Each operator had at least 4 years of experience in morphological

evaluation of the skull. To allow the user to annotate the reference skull, a dedicated guided user interface (GUI) was created using MATLAB. This GUI allowed the user to annotate the skull visualizing multi planar reconstruction (MPR) views. Once all the operators performed the annotation the center of mass of all annotations was used as final landmark positions.

In previous investigations, deformable registration approaches have been used to align corresponding structures in different images in order to estimate anatomical landmarks, as such methods take into account the global appearance information of the anatomical structures [26–28]. During this step, segmentation for both subject and reference was used for masking only, thus keeping the information of gray levels inside the segmented bone. Registration was started by affine transformation that, being global and linear, permits re-scaling according to the individual proportions and also allows a robust compensation of the different volumetric FOVs occurring in CBCT. Its transform is expressed by:

$$F : \mathbf{x}_F \in \Omega_F \rightarrow F(\mathbf{x}_F)$$

$$M : \mathbf{x}_M \in \Omega_M \rightarrow M(\mathbf{x}_M)$$

where $F(\mathbf{x}_F)$ is an intensity value of the image F at the location $\mathbf{x}_F$, Ω_F is the domain of the image F, $M(\mathbf{x}_M)$ is an intensity value of the image M at the location $\mathbf{x}_M$ and Ω_M is the domain of image M [15].

The mean squared intensity difference (MSD) was applied as registration objective function to be minimized. This cost figure is defined as follows:

$$MSD = \frac{1}{N}\sum_{\mathbf{x_F} \in \Omega^T_{F,M}} |F(\mathbf{x}_\mathrm{F}) - M^{Ta}(\mathbf{x}_\mathrm{M})|^2 \qquad (1)$$

where $\mathbf{x}_F$ represents the voxel locations in image F and $\Omega^T_{F,M}$ represents the overlap domain consisting of N voxel subset.

Trilinear interpolation was applied in computing the transformed image gray levels and an iterative gradient descent algorithm was applied to find the optimal transform:

$$R_a = M^{Ta} = T_a(M) \qquad (2)$$

The affine registration (linear) step was used as initialization of a subsequent elastic registration (nonlinear). Importantly, the algorithm was designed to avoid deformations due to the presence of different anatomical structures in the image volumes; which were caused by the limited field of view of CBCT images and inter-subject morphological variability. This problem was solved by shrinking the subjects mask to the overlap subset $T_{F,M}$ found after the first affine registration step, thus cutting out the

individual volume in excess to the reference volume. Then, the skulls were processed with a subsequent step of intensity-based global elastic registration, by MATLAB Medical Image Registration Toolbox, MIRT, Free Form Deformation (FFD) with three hierarchical levels of B-spline control points [30, 31]. A wide mesh window size between the B-spline control points of 15 voxels was set, in order to register the main skull features while avoiding deformation relevant to the largely varying bone structure details and to artifacts. As a result, the number of control points varied for each image, depending on its size. Moreover, in order to prevent the mesh to get too much deformed, a regularization term was used. In particular, the Euclidean distance between all the neighbouring displacements of B-spline control points was penalized [30]. In our algorithm, the regularization weight was set to 0.1. Both mesh window size and regularization weight were empirically determined to give the best performance in term of accuracy. Like the affine one, the elastic registration was an iterative process, which optimizes the MSD voxel similarity measure using a gradient descent optimization method with 3 hierarchical levels of optimization. This additional transformation T_e is defined as:

$$R_e = T_e(R_a) \qquad (3)$$

An example of the outcome of these registration steps is depicted in Fig. 3, which shows how the elastic registration allowed to better adapt the morphology of the reference skull to the patient's one, compared to the affine step.

2.6 Landmark Estimation

Through the registration phase the algorithm superimposes and deforms the reference skull to comply with the morphology of the patient based on the intensity values of the segmented CBCT images. The combined transformations T_a and T_e, can be readily applied to the coordinates of cephalometric landmarks annotated on the reference skull thus labelling the skull under examination.

Namely, the affine transformation T_a is described by a 4x4 matrix $\mathbf{T}_a$ (12 degrees of freedom) applied to the i–th landmark $\boldsymbol{p}_i$ (i = 1, … 21) to obtain the landmark estimate in the patient's reference system, $\widehat{\boldsymbol{p}}_i^a$ [29]:

$$\widehat{\boldsymbol{p}}_i^a = \boldsymbol{T}_a \boldsymbol{p}_i \qquad (4)$$

193 The elastic transformation T_e was implemented numerically on a zeros volume, the size of the original
194 volume, marked with a single 1 at the landmark position. The transformed image was no more binary
195 and the center of mass coordinates were taken as transformed landmark coordinates. The 21 landmark
196 coordinates were collected in a vector $\hat{\boldsymbol{p}}_e$ representing the final estimation of the chosen cephalometric
197 landmark coordinates.
198 At the end of the annotation process each annotated landmark is displayed on the 3D surface of the patient
199 skull. Moreover, each landmark is centered into a spherical confidence region that helps the clinician
200 during a subsequent eventual manual refinement of the annotation, as can be seen in Fig 4. The radius of
201 the confidence spheres was set to the 95th percentile of the annotation error population calculated during
202 the validation step.
203
204
205 **2.7 Validation**
206
207 Optimized thresholding, though preliminary to registration and automated annotation, was considered a
208 crucial step deserving a specific validation. Therefore, the algorithm outcomes were compared to the
209 manual thresholding performed by an experienced user on the whole data set. Both threshold values and
210 segmented volumes were compared testing correlation and significance of differences of automatic vs.
211 manual identification. Depending on the normality of data, either Student's t-test or Wilcoxon signed
212 rank test was used; p-value significance level was set to 0.05. The normality of data distribution was
213 checked with Jarque-Bera test; also in this case significance level was set to 0.05.
214 To evaluate the quality of the annotations performed in this study all CBCT volumes were manually
215 annotated. In particular, in order to take the inter-operator variability of the annotation process into
216 account, a team of expert users manually annotated the image dataset. This way, for each subject, the
217 expected location of the 21 cephalometric landmarks can be defined as the barycenter of the operators'
218 annotation. Fig. 4 shows an example of manually and automatically annotated landmarks.
219 Subsequently, the Euclidean distance, expressed in mm, between the position of each manually annotated
220 landmark and the position of its corresponding landmark estimated by the proposed algorithm, was
221 calculated. These distances will be subsequently used to display confidence regions around the estimate
222 landmarks in order to allow the user to easily place the landmark in the most suitable place.
223
224 **3. RESULTS**

3.1 Segmentation

To evaluate the accuracy of the segmentation process, both threshold values and segmented volumes where compared. Both manual and automatic threshold values resulted normally distributed ($p > 0.05$). They were highly correlated ($R = 0.96$, $p < 0.001$) and no significant difference was found between them ($p > 0.05$), thus indicating that the automatic optimization well reproduced the threshold setting of experts.

Segmented volume values resulted not normally distributed ($p < 0.05$), and non-parametric tests were used for their statistical comparisons. Even for these values, a high level of accuracy was found between automatically and manually segmented volume values ($\rho = 0.98$, $p < 0.001$) and no significant differences were found between the two groups ($p > 0.05$).

3.2 Landmark Estimation

The mean (standard deviation) inter-operator interclass correlation coefficient (ICC) for all the analyzed landmarks was 0.98 (0.04).

The overall median value of the computer aided localization error was equal to 1.99 mm with an interquartile range (IQR) of 1.22 – 2.89 mm. This median error expressed in the horizontal, vertical and transverse direction was equal to 0.60 mm, 0.86 mm and 0.89 mm respectively. These distances widely varied among different landmarks. In particular, among the calculated estimation errors the lowest value was reported for the PNS landmark with a median value of 1.47 mm and an IQR of 0.79 – 1.76 mm. On the other hand, the highest values were observed for Gonia, respectively right Gonion with a median value of 2.81 mm and an IQR of 1.46 - 4.83 mm and left Gonion with a median value of 4.00 mm and an IQR of 2.00 - 4.86 mm.

Considering all landmarks, annotation error was less than 5.00 mm for 90% of landmarks and less than 2.50 mm for 63% of them. The descriptive statistics for the obtained distances for each landmark are shown in Tab. 2.

4. CONCLUSION

The proposed method allows to find a good estimate of landmark positions, which may subsequently be refined by the clinician, saving operator time and reducing annotation variability.

Nowadays the annotation of cephalometric points is mainly performed manually. Recent studies reported that the error caused by identification of landmark varies between 0.02 mm to 2.47 mm [9–11, 32].

Therefore, one important aim for the evaluation of skeletal morphology in maxillofacial patients is to reduce the landmark identification error below 2.00 mm [32].

In the present study, landmarks lying in different locations present largely different average localization errors. Using our method, Gonia arise as the most difficult markers to localize. As a matter of fact, this reflects the variability of human anatomy and manual annotation. The mandibular bone, statistically, is among the most variable bones of the skull [33] and this is reflected in the estimation of right and left Gonion [34].

In this study, since annotation errors were not normally distributed among different patients ($p<0.001$), the median annotation error was used to access the process accuracy of the annotation process. In particular, the median annotation error was found as 1.99 mm with an IQR of 1.22 – 2.89 mm. In a recent study, Shahidi et al. validated an algorithm for landmark annotation based on 3D image registration for 14 landmarks on a dataset of 20 CBCT images. They obtained an overall mean error of 3.40 mm, which is significantly higher compared to the one obtained with the current method [16]. In another study, Gupta et al. proposed a knowledge-based algorithm for automatic detection of cephalometric landmarks on CBCT images that was validated on 30 CBCT images. Gupta et al. obtained a mean error of 2.01 mm with a standard deviation of 1.23 mm, which is comparable with the one obtained with the proposed methodology [18]. With our method a comparable accuracy level was obtained with reduced *a priori* information about landmark positions.

The method described in the present study attempts a general and robust approach for the propagation of landmarks from an annotated reference skull to subject-specific ones. Due to the variability in skull morphology depending on gender, age and ethnicity, in this study we applied the proposed method to a specific category of patients: adult Caucasian women. To apply the same methodology on other patient categories, different atlases matched for sex, age and ethnicity must be used. The selection of only one specific sample represents a limitation of the current study but, at the same time, the low amount of a priori information needed from the proposed algorithm allows to test it on different patient categories simply changing the used atlas.

Segmentation of hard tissues is a fully automatic process that reduces the amount of error dependent on operator experience. In the validation step, no significant difference was found between manually and automatically determined threshold values. Moreover, the correlation coefficient close to 1 proved the high accuracy of the segmentation step compared to manual thresholding, which is now considered the standard method of segmentation in maxillofacial applications.

Since the segmentation step was proved to be very robust, the registration step represents the main source of variability in automatic annotation. In order to improve the annotation accuracy, local adaptation in a region of interest around each estimated landmark should be added to overcome the limits of the global registration step.

Moreover, we believe that a computer aided cephalometric annotation of CBCT volumes, relying on intensity-based image registration, can be a good initialization that can help the clinician in performing cephalometric analysis. Indeed, for most landmarks the current results are well comparable with those provided by other methods present in the literature [13, 14]. One advantage of our method is that cephalometric landmark coordinates were obtained without any local a priori information about geometry and location of each landmark, allowing physicians to use this approach for personalized cephalometric analysis. Indeed, the method can be customized only changing the number of landmark annotated on the reference skull, without any modification of the annotation algorithm.

Results are promising, nevertheless the study should be expanded in order to validate it on a larger dataset and reduce the estimation error to provide a fully automatic annotation algorithm. Moreover, in order to improve the segmentation and, consequently, the annotation in the dental region, a dedicated high intensity object artifact reducing algorithm should be implemented.

5. CONFLICT OF INTEREST

Marina Codari, Matteo Caffini, Chiarella Sforza, Gianluca M. Tartaglia and Giuseppe Baselli declare that they have no conflict of interest.

6. STATEMENT OF HUMAN RIGHTS

For this type of study formal consent is not required.

7. INFORMED CONSENT

Informed consent was obtained from all patients for being included in the study. The study was approved by the Institutional Review Board of the SST Dental Clinic (IRB03-2015 Doc. MQ 03 AL 02-MC).

REFERENCES

1. Gateno J, Xia JJ, Teichgraeber JF (2011) New 3-dimensional cephalometric analysis for orthognathic surgery. J Oral Maxillofac Surg 69:606–622. doi: 10.1016/j.joms.2010.09.010

2. Bettega G, Payan Y, Mollard B, Boyer A, Raphael B, Lavallèe S (2000) A Simulator for Maxillofacial Surgery Integrating 3D Cephalometry and Orthodontia. Comput aided Surg 5:156–165.

3. Hurst CA, Eppley BL, Havlik RJ, Sadove AM (2007) Surgical cephalometrics: applications and developments. Plast Reconstr Surg 120:92e–104e. doi: 10.1097/01.prs.0000282728.97278.a2

4. Pittayapat P, Limchaichana-Bolstad N, Willems G, Jacobs R (2014) Three-dimensional cephalometric analysis in orthodontics: a systematic review. Orthod Craniofac Res 17:69–91. doi: 10.1111/ocr.12034

5. Swennen GRJ, Schutyser F (2006) Three-dimensional cephalometry: spiral multi-slice vs cone-beam computed tomography. Am J Orthod Dentofacial Orthop 130:410–416. doi: 10.1016/j.ajodo.2005.11.035

6. Al-Okshi A, Lindh C, Salé H, Gunnarsson M, Rohlin M (2015) Effective dose of cone beam CT (CBCT) of the facial skeleton: a systematic review. Br J Radiol 88:20140658. doi: 10.1259/bjr.20140658

7. Weissheimer A, Menezes LM, Koerich L, Pham J, Cevidanes LHS (2015) Fast three-dimensional superimposition of cone beam computed tomography for orthopaedics and orthognathic surgery evaluation. Int J Oral Maxillofac Surg 44:1188–1196. doi: 10.1016/j.ijom.2015.04.001

8. Sun Y, Luebbers H-T, Agbaje JO, Schepers S, Vrielinck L, Lambrichts I, Politis C (2013) Validation of anatomical landmarks-based registration for image-guided surgery: An in-vitro study. J Cranio-Maxillo-Facial Surg 41:522–526.

9. Swennen GRJ, Schutyser F, Barth E-L, De Groeve P, De Mey A (2006) A New Method of 3-D Cephalometry Part I: The Anatomic Cartesian 3-D Reference System. J Craniofac Surg 17:314–325.

10. Titiz I, Laubinger M, Keller T, Hertrich K, Hirschfelder U (2011) Repeatability and reproducibility of landmarks--a three-dimensional computed tomography study. Eur J Orthod 34:1–11. doi: 10.1093/ejo/cjq190

11. Katkar RA, Kummet C, Dawson D, Moreno Uribe L, Allareddy V, Finkelstein M, Ruprecht A (2013) Comparison of observer reliability of three-dimensional cephalometric landmark identification on subject images from Galileos and i-CAT cone beam CT. Dentomaxillofacial

Radiol 42:1–11. doi: 10.1259/dmfr.20130059

12. Cheng Y, Leow WK (2012) Automatic identification of Frankfurt plane and mid-sagittal plane of skull. 2012 IEEE Work Appl Comput Vis 233–238. doi: 10.1109/WACV.2012.6162994

13. Keustermans J, Mollemans W, Vandermeulen D, Suetens P (2010) Automated Cephalometric Landmark Identification Using Shape and Local Appearance Models. In: 20th Int. Conf. Pattern Recognit. Ieee, pp 2464–2467

14. Keustermans J, Smeets D, Vandermeulen D, Suetens P (2011) Automated cephalometric landmark localization using sparse shape and appearance models. In: Mach. Learn. Med. Imaging. Springer Berlin Heidelberg, pp 249–256

15. Wang L, Chen KC, Gao Y, Shi F, Liao S, Li G, Shen SGF, Yan J, Lee PKM, Chow B, Liu NX, Xia JJ, Shen D (2014) Automated bone segmentation from dental CBCT images using patch-based sparse representation and convex optimization. Med Phys 41:043503. doi: 10.1118/1.4868455

16. Shahidi S, Bahrampour E, Soltanimehr E, Zamani A, Oshagh M, Moattari M, Mehdizadeh A (2014) The accuracy of a designed software for automated localization of craniofacial landmarks on CBCT images. BMC Med Imaging 14:32. doi: 10.1186/1471-2342-14-32

17. Makram M, Kamel H (2014) Reeb Graph for Automatic 3D Cephalometry. Int J Image Process 8:17–29.

18. Gupta A, Kharbanda OP, Sardana V, Balachandran R, Sardana HK (2015) A knowledge-based algorithm for automatic detection of cephalometric landmarks on CBCT images. Int J Comput Assist Radiol Surg 10:1737–1752. doi: 10.1007/s11548-015-1173-6

19. de Oliveira AEF, Cevidanes LHS, Phillips C, Motta A, Burke B, Tyndall D (2009) Observer reliability of three-dimensional cephalometric landmark identification on cone-beam computerized tomography. Oral Surg Oral Med Oral Pathol Oral Radiol Endod 107:256–265. doi: 10.1016/j.tripleo.2008.05.039

20. Swennen GRJ, Schutyser F, Hausamen JE (2005) Three-dimensional cephalometry: a color atlas and manual. Springer Science & Business Media

21. Sagawa M, Miyoseta Y, Hayakawa Y, Honda A (2009) Comparison of two- and three-dimensional filtering methods to improve image quality in multiplanar reconstruction of cone-beam computed tomography. Oral Radiol 25:154–158. doi: 10.1007/s11282-009-0026-9

22. Hassan B, Souza PC, Jacobs R, de Azambuja Berti S, van der Stelt P (2010) Influence of scanning and reconstruction parameters on quality of three-dimensional surface models of the dental arches from cone beam computed tomography. Clin Oral Investig 14:303–310. doi: 10.1007/s00784-009-0291-3

23. Pham DL, Xu C, Prince JL (2000) Current Methods in Medical Image Segmentation 1. Annu Rev Biomed Eng 2:315–337.

24. Ng HP, Ong SH, Foong KWC, Goh PS, Nowinski WL (2006) Medical Image Segmentation Using K-Means Clustering and Improved Watershed Algorithm. In: 2006 IEEE Southwest Symp. Image Anal. Interpret. pp 61–65

25. MacKay DJ (2003) Information theory, inference and learning algorithms. Cambridge university press

26. Gao Y, Zhan Y, Shen D (2014) Incremental Learning With Selective Memory (ILSM): Towards Fast Prostate Localization for Image Guided Radiotherapy Yaozong. IEEE Trans Med Imaging 33:518–534. doi: 10.1109/TMI.2013.2291495. Incremental

27. Liu J, Gao W, Huang S, Nowinski WL (2008) A Model-Based, Semi-Global Segmentation Approach for Automatic 3-D Point Landmark Localization in Neuroimages. IEEE Trans Med Imaging 27:1034–1044. doi: 10.1109/TMI.2008.915684

28. Frantz S, Rohr K, Stiehl HS (2000) Localization of 3D anatomical point landmarks in 3D tomographic images using deformable models. In: Med. Image Comput. Comput. Interv. 2000. Springer Berlin Heidelberg, pp 492–501

29. Hill DL, Batchelor PG, Holden M, Hawkes DJ (2001) Medical image registration. Phys Med Biol 46:R1–R45.

30. Myronenko A, Song X (2010) Intensity-Based Image Registration by Minimizing Residual Complexity. Med Imaging, IEEE Trans 29:1882–1891.

31. Rueckert D, Sonoda LI, Hayes C, Hill DL, Leach MO, Hawkes DJ (1999) Nonrigid registration using free-form deformations: application to breast MR images. IEEE Trans Med Imaging 18:712–721. doi: 10.1109/42.796284

32. Baan F, Liebregts J, Xi T, Schreurs R, de Koning M, Bergé S, Maal T (2016) A New 3D Tool for Assessing the Accuracy of Bimaxillary Surgery: The OrthoGnathicAnalyser. PLoS One 11:e0149625. doi: 10.1371/journal.pone.0149625

33. Puisoru M, Forna N, Fatu A, Fuatu R, Fuatu C (2006) Analysis of mandibular variability in humans of different geographic areas. Ann Anatomy-Anatomischer Anzeiger 188:547–554.

34. Schlicher W, Nielsen I, Huang JC, Maki K, Hatcher DC, Miller a. J (2012) Consistency and precision of landmark identification in three-dimensional cone beam computed tomography scans. Eur J Orthod 34:263–275. doi: 10.1093/ejo/cjq144

Fig. 1. Flowchart of the presented algorithm, which receives a DICOM file as input, articulates in 3 phases: image pre-processing, segmentation and registration and returns the landmark coordinates as output

Fig. 2. The figure shows, in a median sagittal slice, which structures are maintained during the segmentation process

Fig. 3. Example of affine registration (above) and affine + elastic registration (below). Median sagittal view of the segmented subject skull (light) with the register

Fig. 4. Example of the proposed, computer aided, annotation process outcome; each landmark is cantered into a spherical confidence region (95^{th} percentile of the annotation error population) that can help the clinician in a subsequent manual refinement of the annotation

Figure 1

Click here to download Figure cefalo_Fig.1_new.tif

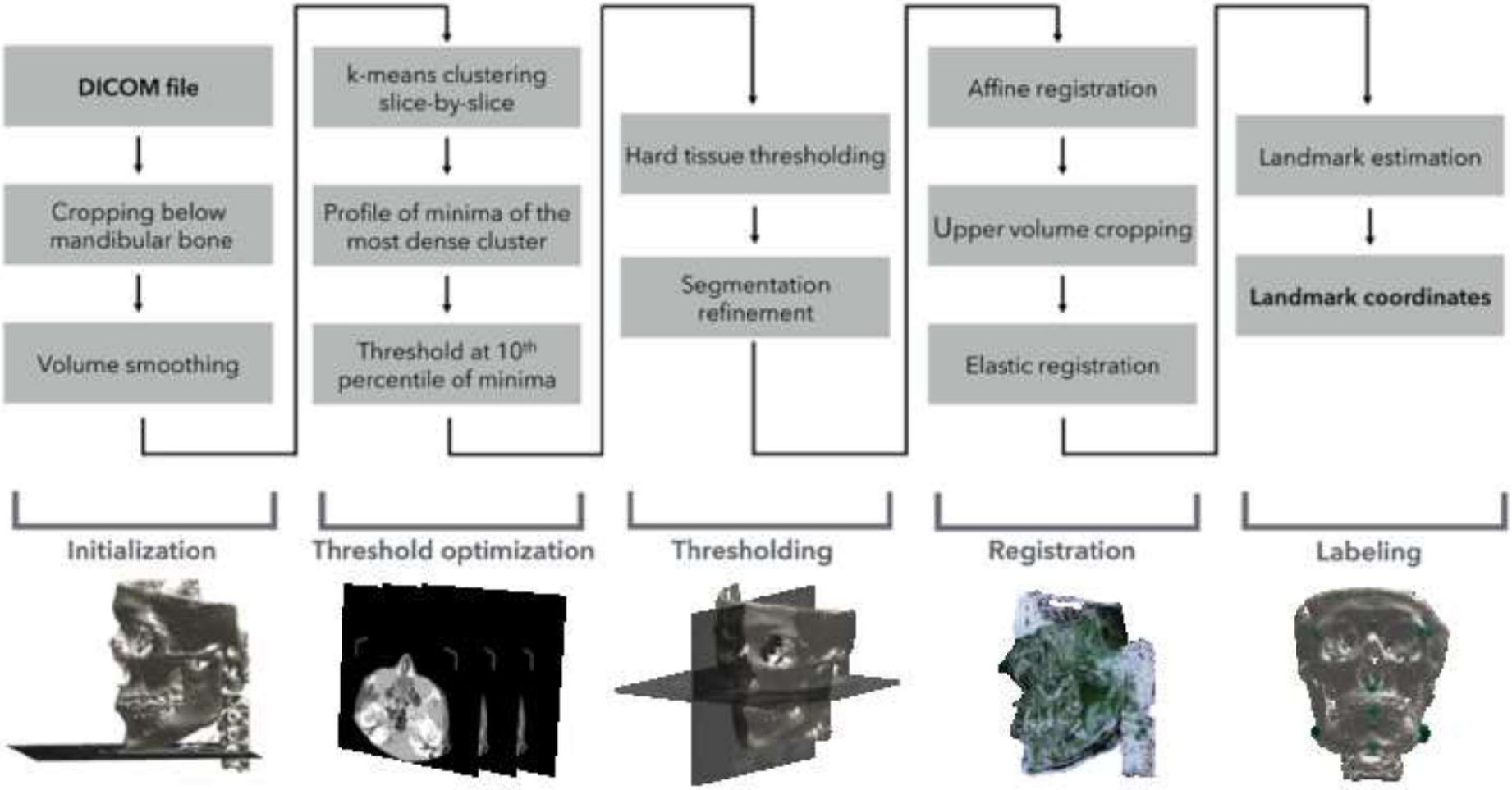

Figure 2

Click here to download Figure cefalo_Fig.2.tif

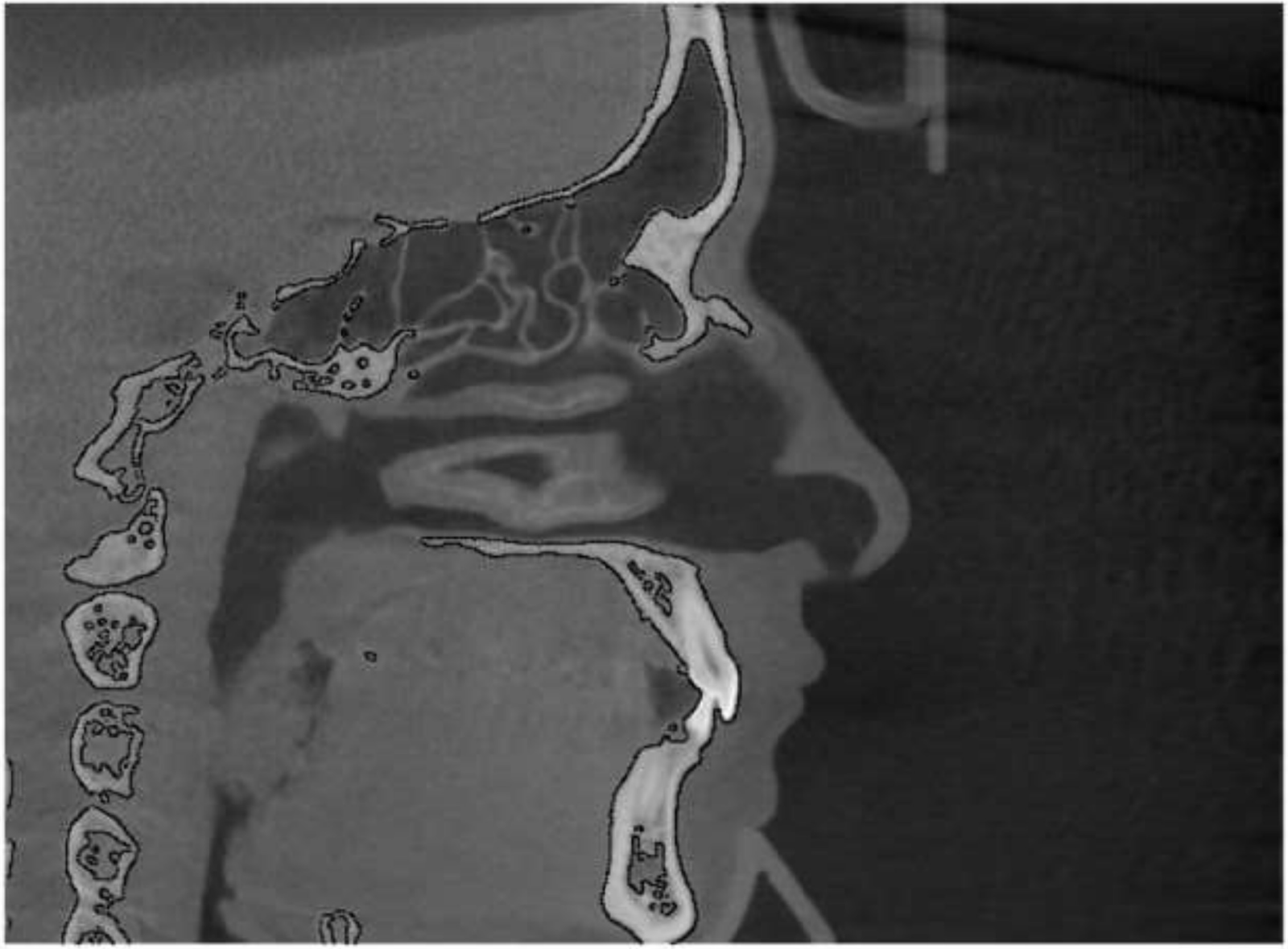

Figure 3

Click here to download Figure cefalo_Fig.3.tif

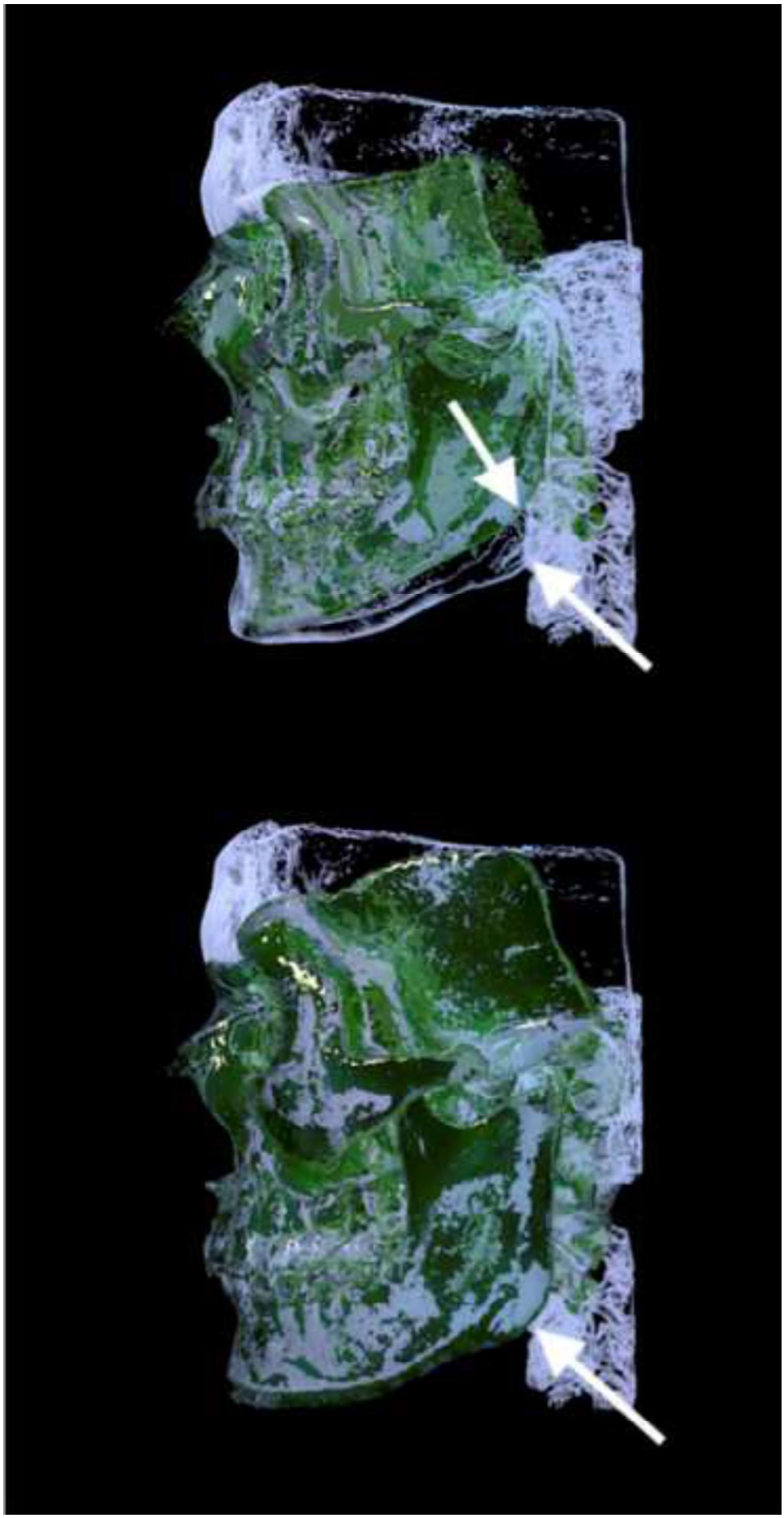

Figure 4

Click here to download Figure cefalo_Fig. 4.tif

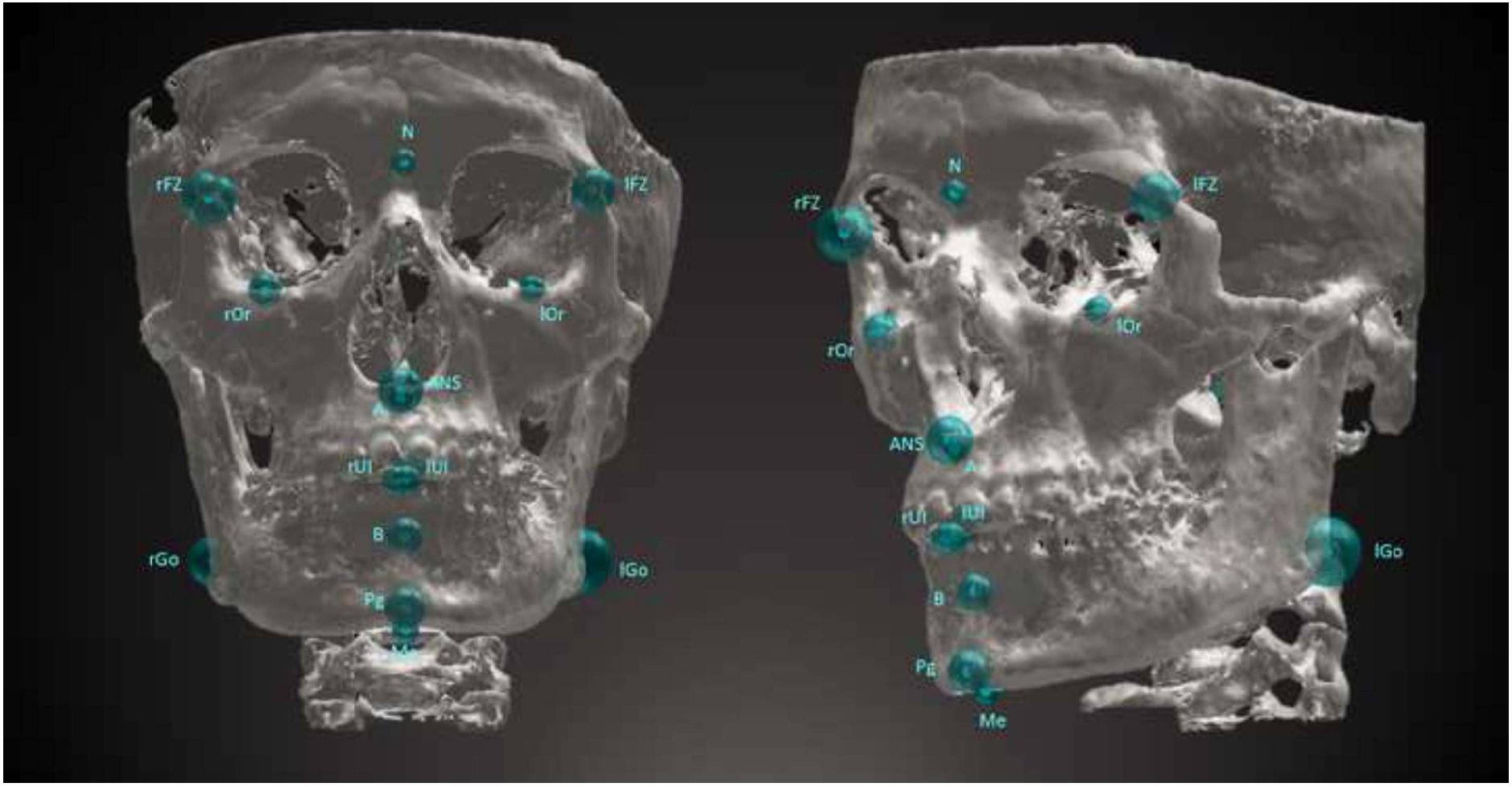

Table 1

Tab.1. List of the 21 estimated landmarks as defined by Swennen et al [16].

Landmark Name	Abbreviation	Definition
Sella Turcica	**S**	the centre of the hypophyseal fossa
Nasion	**N**	the midpoint of the frontonasal suture
Left and Right Gonion	**lGo and rGo**	the point at each mandibular angle that is defined by dropping a perpendicular from the intersection point of the tangent lines to the posterior margin of the mandibular
Anterior Nasal Spine	**ANS**	the most anterior midpoint of the anterior nasal spine of the maxilla.
Pogonion	**Pg**	the most anterior midpoint of the chin on the outline of the mandibular symphysis
Menton	**Me**	the most inferior midpoint of the chin on the outline of the mandibular symphysis
Left and Right Orbitale	**lOr**	the most inferior point of each infraorbital rim
Posterior Nasal Spine	**PNS**	the most posterior midpoint of the posterior nasal spine of the palatine bone
Left and Right posterior maxillary points	**lPM and rPM**	the most posterior midpoint of the posterior nasal spine of the palatine bone.
Left and Right Upper Incisor	**lUI and rUI**	is the most mesial point of the tip of the crown of each upper central incisor
Left and Right Lower Incisor	**lLI and rLI**	is the most mesial point of the tip of the crown of each lower central incisor
Frontozygomatic Point	**lFZ and rFZ**	the most medial and anterior point of each frontozygomatic suture at the level of the lateral orbital rim
A Point	**A**	the point of maximum concavity in the midline of the alveolar process of the maxilla
B Point	**B**	point of maximum concavity in the midline of the alveolar process of the mandible
Basion	**Ba**	the most anterior point of the great foramen

Table 2

Tab.2. Descriptive statistics of the obtained Euclidean distances for each landmark.

Landmark	Median [mm]	IQR [mm]	Max [mm]	Min [mm]
S	1.42	0.82 - 1.73	3.53	0.60
N	2.27	1.20– 2.92	4.71	0.28
lGo	4.00	2.00 – 4.86	8.33	0.45
rGo	2.81	1.46 – 4.83	6.62	0.28
ANS	2.35	1.74 – 2.97	5.70	0.60
Pg	2.87	2.11 – 4.05	5.24	0.00
Me	1.61	1.36 – 2.09	3.60	0.30
lOr	1.47	0.89 – 2.23	4.46	0.28
rOr	1.34	0.83 – 2.27	5.20	0.30
PNS	1.47	0.79 – 1.76	4.62	0.30
lPM	1.61	1.09 – 2.41	3.63	0.50
rPM	1.97	1.25 – 2.93	7.26	0.69
lUI	1.40	0.95 – 2.05	3.60	0.37
rUI	2.01	1.39 – 2.40	7.27	0.82
lLI	2.19	1.68 – 2.58	3.89	1.04
rLI	3.07	2.22 – 3.92	5.84	0.92
lFZ	1.81	1.13 – 4.30	6.60	0.50
rFZ	2.01	1.31 – 2.94	6.98	0.82
A	1.73	1.04 – 2.35	3.68	0.69
B	2.83	1.64 – 3.68	5.31	0.73
Ba	2.22	1.68 – 2.67	2.98	1.08
All	1.99	1.22 – 2.89	8.33	0.0